NASA/CR—2015-218713

# Architecture, Voltage and Components for a Turboelectric Distributed Propulsion Electric Grid (AVC-TeDP)

*Paul Gemin, Tom Kupiszewski, and Arthur Radun*
*GE Aviation, Cincinnati, Ohio*

*Yan Pan, Rixin Lai, Di Zhang, Ruxi Wang, Xinhui Wu, Yan Jiang, Steve Galioto, Kiruba Haran, William Premerlani, Jim Bray, and Antonio Caiafa*
*GE Global Research, Niskayuna, New York*

July 2015

# NASA STI Program . . . in Profile

Since its founding, NASA has been dedicated to the advancement of aeronautics and space science. The NASA Scientific and Technical Information (STI) Program plays a key part in helping NASA maintain this important role.

The NASA STI Program operates under the auspices of the Agency Chief Information Officer. It collects, organizes, provides for archiving, and disseminates NASA's STI. The NASA STI Program provides access to the NASA Technical Report Server—Registered (NTRS Reg) and NASA Technical Report Server—Public (NTRS) thus providing one of the largest collections of aeronautical and space science STI in the world. Results are published in both non-NASA channels and by NASA in the NASA STI Report Series, which includes the following report types:

- TECHNICAL PUBLICATION. Reports of completed research or a major significant phase of research that present the results of NASA programs and include extensive data or theoretical analysis. Includes compilations of significant scientific and technical data and information deemed to be of continuing reference value. NASA counter-part of peer-reviewed formal professional papers, but has less stringent limitations on manuscript length and extent of graphic presentations.

- TECHNICAL MEMORANDUM. Scientific and technical findings that are preliminary or of specialized interest, e.g., "quick-release" reports, working papers, and bibliographies that contain minimal annotation. Does not contain extensive analysis.

- CONTRACTOR REPORT. Scientific and technical findings by NASA-sponsored contractors and grantees.

- CONFERENCE PUBLICATION. Collected papers from scientific and technical conferences, symposia, seminars, or other meetings sponsored or co-sponsored by NASA.

- SPECIAL PUBLICATION. Scientific, technical, or historical information from NASA programs, projects, and missions, often concerned with subjects having substantial public interest.

- TECHNICAL TRANSLATION. English-language translations of foreign scientific and technical material pertinent to NASA's mission.

For more information about the NASA STI program, see the following:

- Access the NASA STI program home page at http://www.sti.nasa.gov

- E-mail your question to help@sti.nasa.gov

- Fax your question to the NASA STI Information Desk at 757-864-6500

- Telephone the NASA STI Information Desk at 757-864-9658

- Write to:
  NASA STI Program
  Mail Stop 148
  NASA Langley Research Center
  Hampton, VA 23681-2199

NASA/CR—2015-218713

# Architecture, Voltage and Components for a Turboelectric Distributed Propulsion Electric Grid (AVC-TeDP)

*Paul Gemin, Tom Kupiszewski, and Arthur Radun*
*GE Aviation, Cincinnati, Ohio*

*Yan Pan, Rixin Lai, Di Zhang, Ruxi Wang, Xinhui Wu, Yan Jiang, Steve Galioto, Kiruba Haran, William Premerlani, Jim Bray, and Antonio Caiafa*
*GE Global Research, Niskayuna, New York*

Prepared under Contract NNC10BA06B, Task Order NNC13TA73T

National Aeronautics and
Space Administration

Glenn Research Center
Cleveland, Ohio 44135

July 2015

*Level of Review*: This material has been technically reviewed by NASA technical management OR expert reviewer(s).

Available from

NASA STI Program
Mail Stop 148
NASA Langley Research Center
Hampton, VA 23681-2199

National Technical Information Service
5285 Port Royal Road
Springfield, VA 22161
703-605-6000

This report is available in electronic form at http://www.sti.nasa.gov/ and http://ntrs.nasa.gov/

# Architecture, Voltage and Components for a Turboelectric Distributed Propulsion Electric Grid (AVC-TeDP)

Paul Gemin, Tom Kupiszewski, and Arthur Radun
GE Aviation
Cincinnati, Ohio 45215

Yan Pan, Rixin Lai, Di Zhang, Ruxi Wang, Xinhui Wu, Yan Jiang, Steve Galioto,
Kiruba Haran, William Premerlani, Jim Bray, and Antonio Caiafa
GE Global Research
Niskayuna, New York 12309

## Summary

This report contains the deliverables for the NASA Research and Technology for Aerospace Propulsion Systems (RTAPS) study of Architecture, Voltage and Components for a Turboelectric Distributed Propulsion System (TeDP).

The purpose of this effort was to advance the selection, characterization, and modeling of a propulsion electric grid for a TeDP system for transport aircraft. NASA is evaluating turboelectric aircraft propulsion to meet N+3 / N+4 goals.

Previous NASA efforts have identified blended wing body airframes as a fuel efficiency improvement over tube and wing airframes. Combined with a blended wing body airframe, distribution of the propulsion fans allows higher propulsive efficiency through reduction of drag, a higher equivalent bypass ratio, and boundary layer ingestion. To achieve distribution of fans beyond a limited number may become cumbersome with gearing and shaft arrangements, thus NASA has studied electrical propulsion architectures. Existing electrical propulsion systems in the required power range (sea-going ships, for example) would be too heavy for aerospace, either for practical integration or fuel savings. Earlier studies determined that distribution and protection power system components accounted for approximately 30 percent of system mass. This study developed architecture options and circuit breaker technology estimating the impact on a propulsion power system.

Since the losses of turboelectric system detract from the fuel savings derived from the distributed concept, NASA is investigating cryogenic and superconducting electrical components. The need for efficient transmission of power in a cryogenic system is amplified by the additional power required to move any losses from cryogenic to ambient temperatures. The required cooling power is also the rationale behind a system where all components are cryogenic, with no interfaces to ambient temperatures, thus minimizing heat leak (and the power required to remove the heat). To meet these goals, the study proposed an architecture with hybrid circuit breakers. These breakers are estimated to provide an improved power density over mechanical breakers and improved efficiency over solid-state breakers.

Narrowing the range of potential system grid voltages for the electric propulsion system was also a major focus of the study. In selecting the voltage level, it is assumed that the high voltage system components will all exist in a pressurized cryogen which may be at 1 atmosphere or higher. The absence of electrical component exposure to low pressure gas is intended to prevent voltage breakdown. A supercritical cryogen is also presented as an option that would have the advantage of not allowing the formation of bubbles. Further, a two cryogen system (operating at two temperatures) is presented as an option. Such a system may allow reduced cooling power, depending on the location of losses and the performance and availability of cryocoolers.

Voltage selection is a balance between power conversion design, transmission cable mass, and cryocooler mass and power. Three parameters were varied over a wide range to determine if incorrect

assumptions or estimates would greatly impact the preferred DC link voltage. All cases show the greatest decrease in the component mass, with increasing voltage, occurs by approximately 6 kV. For the architecture selected and the associated assumptions, a minimum occurs at about 8 to 10 kV. Given the wide range of estimates in cable length and power densities, a voltage of over 6 kV would capture much of the weight reduction; a minimum may occur between 6 kV and 10 to 12 kV. To further refine projections of power conversion losses, semiconductor loss testing was performed with available devices.

A dynamic model was created to allow investigation of nominal operation and limited fault scenarios. The philosophy of the modeling approach was to allow rapid simulation of a simplified model with component parameters based on projected response. Example operation of the model through controlled power transients and several fault cases showed stable operation of the DC power system.

For standards development related to DC power systems for TeDP aircraft, potentially relevant existing standards were reviewed. The marine space provides perhaps the closest analog; however, Medium-Voltage DC (MVDC) power systems are still not a mature technology and will require continued research activities. Although there are some IEEE Power Electronics Standards for Ships in which MVDC power systems are discussed, those standards themselves are not finalized and cannot be applied directly to MVDC systems targeted for aerospace propulsion application and involving the use of cryogenic, high power, electrical equipment. Major sections of existing standards were used to propose content areas for MVDC systems for aircraft.

# Contents

# List of Tables



# List of Figures

## List of Acronyms and Abbreviations

| | |
|---|---|
| AMSC | American Superconductor |
| BIU | Bus Interface Unit |
| BSCCO | $Bi_2Sr_2Ca_2Cu_3O_{10}$ |
| COP | Coefficient of Performance |
| CORC | Conductor On Round Core |
| DUT | Device Under Test |
| EMI | Electromagnetic Interference |
| FCL | Fault Current Limiter |
| GaN | gallium nitride |
| HVDC | high-voltage DC |
| $LN_2$ | liquid nitrogen |
| $MgB_2$ | magnesium diboride |
| MMC | Modular Multilevel Converter |
| MSDC | Modular Stack DC |
| MTBSI | Mean-Time-Between-Service-Interruption |
| MVDC | medium-voltage DC |
| $N_2$ | nitrogen |
| Ne | neo |
| NPC | Neutral-Point-Clamped |
| SCS | Surround Copper Stabilizer |
| Si | silicon |
| SiC | silicon carbide |
| SSCB | Solid-State Circuit Breaker |
| TeDP | Turboelectric Distribution Propulsion |
| THD | Total Harmonic Distortion |
| YBCO | yttrium boron copper oxide |
| ZnO | zinc oxide |

# 1.0 Study Introduction

The purpose of this effort is to advance the selection, characterization, and modeling of a propulsion electric grid for a TeDP system for transport aircraft. NASA is evaluating turboelectric aircraft propulsion to meet N+3 / N+4 goals.

Previous NASA efforts have identified blended wing body airframes as a fuel efficiency improvement over tube and wing airframes. Combined with a blended wing body airframe, distribution of the propulsion fans allows higher propulsive efficiency through reduction of drag, a higher equivalent bypass ratio, and boundary layer ingestion. To achieve distribution of fans beyond a limited number may become cumbersome with gearing and shaft arrangements, thus NASA has considered electrical propulsion architectures. Existing electrical propulsion systems in the required power range (sea-going ships, for example) would be too heavy for aerospace, either for practical integration or fuel savings. Additionally, the losses of such systems would detract from the fuel savings derived from the distributed concept. For the improved power density and component efficiency, NASA is investigating cryogenic and superconducting electrical components.

This study had seven primary milestones:

1. Range of bus voltage and grid architecture selection for TeDP,
2. Mechanical versus solid-state circuit breakers comparison for cryogenic operation
3. Mass and efficiency model development for all grid components,
4. The development of sensitivities to bus voltage for all components,
5. The selection of a narrowed range of DC voltage,
6. Dynamic state-variable model development, and
7. Standards development recommendations

This report addresses these milestones and shows the progress of the work. For example, component mass and efficiency estimates were made early in the study to select architecture concepts, but were later refined as the architecture detail was developed. The report covers the early study estimates, as well as the estimates reached by end of the study.

NASA efforts provide several high-level assumptions to use for evaluation of the systems. Any of these assumptions were open to modification if a rationale was discovered. These assumptions are listed below.

- A turboelectric system
- 50 MW generation system
- 50 MW fan loads
- 1 to 10 kV power system
- All cryogenic system—no components at ambient temperatures
- Rotating machines were expected to be fully superconducting, synchronous machines

Narrowing of the voltage range was a major focus of this work. Several other areas were out-of-scope. Specifically, the cryogenics system that supports the cold components was presumed to be sufficiently redundant and was not part of this study; linking of the propulsive electrical grid to any other aircraft electrical systems was not part of this study; and detailed modeling of the superconducting machines was not part of this study.

The sections below describe the study approach and results to reach the defined milestones.

# 2.0 Grid Architecture and Bus Voltage Range Selection

## 2.1 System Requirements and Assumptions

Per NASA guidance, the bus voltage range to start with was 1 to 10 kV. The high power parts of the electrical system are expected to be entirely cryogenic, from the generator stator windings to the motor stator windings, without any high-current electrical leads to room temperatures. Also per scope definition, thermal modeling was not a significant part of the tasks; the cryogenic system that supports the cold components was presumed to be sufficiently redundant and was not part of this study. Detailed machine design was not part of the study. The rotating machines were expected to be fully-superconducting, wound-rotor, synchronous machines with superconducting windings on both the rotors and the stators.

The N3-X TeDP Baseline architecture includes two wingtip-mounted turboshaft engines, and each drives two cryogenically cooled superconducting electrical generators. Power electronics convert the variable frequency AC power to DC so as to improve distribution efficiency and eliminate the requirements to sync the power sources. NASA specifies 50 MW of total system power, with 25 MW in the event of a single engine failure. Therefore each power plant (one engine / two generators / converters) is sized to provide 25 MW, the minimum power required at take-off for the single engine failure scenario as recommended by NASA studies (Ref. 1). Two power plants' total power level is 50 MW. Fail-safe requirements from (Ref. 1) indicates that no single point failure should yield catastrophic consequences at the aircraft level. Redundancy design and component sizing in this study will follow this rule so that with any single point failure in the electric grid, the remaining system can provide 25 MW propulsion power.

## 2.2 Architecture Trades

A recent NASA study (Ref. 1) discussed promising architectures. However, it also demonstrated that circuit breakers could constitute 30 percent of the weight of the entire TeDP system, which was a component not previously included in earlier studies. Two new architectures will be proposed incorporating a power rating increase from 22.37 to 25 MW per NASA instruction and targeting advanced techniques to limit the usage of circuit breakers while maintaining high reliability. It needs to be noted that this stage of the study was completed with the assumption of 50 MW generation capability, but only 25 MW fan load. When the rating of elements in this section are listed as a percentage, this is the percentage of 25 MW, the required power for rolling take-off. The final estimates and architecture use 50 MW generation and 50 MW load component ratings.

### 2.2.1 Baseline Architecture

This architecture is based on Architecture 3 developed in the referenced NASA study (Ref. 1), which allows the same rating for all four generators and three buses. Redundant feeders provide power rerouting capability during a bus / generator / engine failure. The following study will take it as the Baseline Architecture for comparison. For an easy and clear comparison, the Baseline Architecture is shown in this report again in Figure 1.

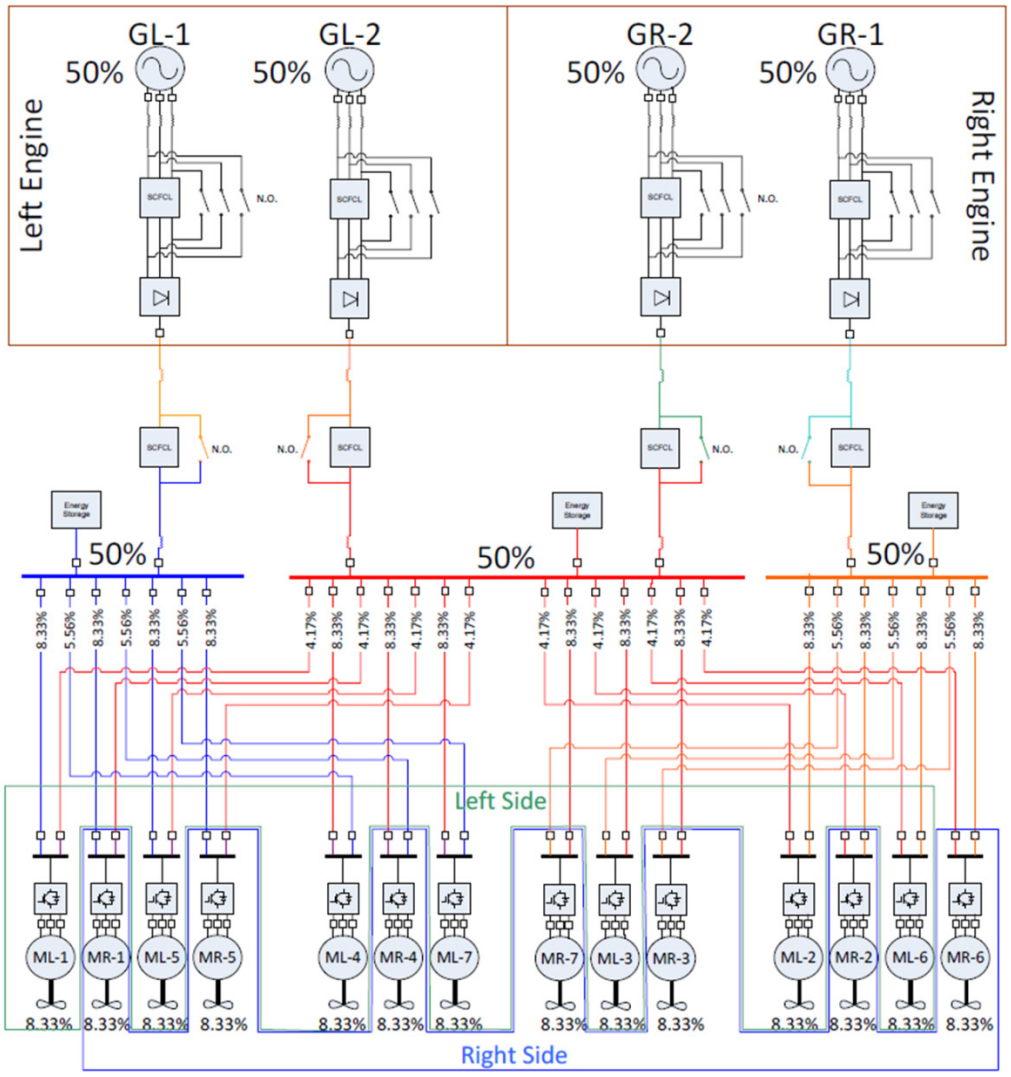


Figure 1.—Baseline Architecture (proposed in the Phase I study)

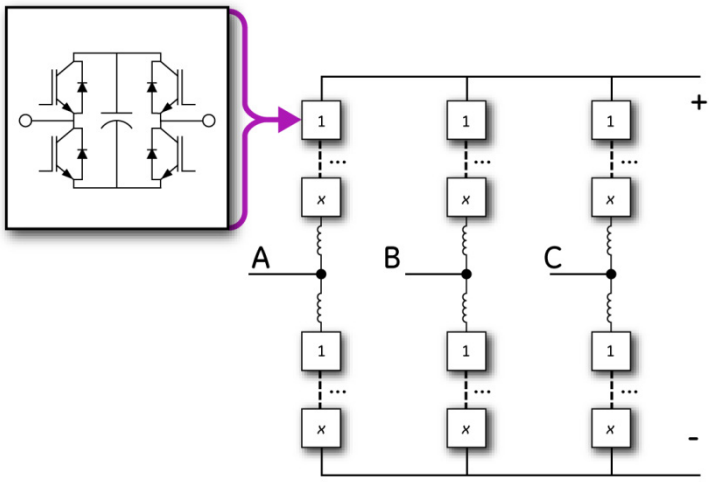


Figure 2.—Possible Topology for MMC

A newly developed Modular Multilevel Converter (MMC) technology (Refs. 2, 3, and 4) can be applied to provide integrated power conversion, fault current limitation, and fault current isolation. Figure 2 demonstrates a possible topology of MMC in a HVDC application. In our study, only one or two modules are needed due to the much lower voltage level. The adopting of MMC can bring the Baseline Architecture to a much more compact design where a single MMC can replace the fault current limiter, rectifier, and circuit breaker. However, MMC technology relies on the use of large capacitors, which greatly detracts from the weight benefits of removing circuit breakers, so much so that this technology is not taken into consideration for any of the architectures.

### 2.2.2 Voltage Source Architecture with Fast Disconnects (Architecture 1)

The reduction of circuit breakers in Architecture 1 is achieved by a new fault isolation scheme with the usage of super-fast disconnects as illustrated in Figure 3. A disconnect is a kind of mechanical contact which does not have current interrupting capability, but can open the circuit while no current flows in it. It is much lighter than a circuit breaker, about 600 kW/kg compared to 200 kW/kg, as the study in Appendix A shows. The modification made in Architecture 1 is replacing most of the circuit breakers with disconnects to reduce the system weight while maintaining high availability.

In Architecture 1, there are four DC circuit breakers at the starting end of wing transmission lines to interrupt the current from generators when a fault occurs in the downstream system. A DC circuit breaker is also put near each motor converter to prevent back feeding from motors during an upstream fault. Other circuit breakers originally designed to be in the Baseline Architecture are replaced by super-fast disconnects, such as the circuit breakers at the bus end of the wing transmission lines and the circuit breakers at both ends of the central feeders. If a fault occurs in the distribution system (on the wing transmission, the bus, or the feeder), the isolation scheme is that the related circuit breakers will rapidly open to stop feeding the fault from the generator and motors, then DC disconnects can operate to isolate the faulty section, followed by close of circuit breakers to recover the power feeding from the generator to the remaining healthy system. With quick response of circuit breakers and super-fast disconnects, the whole process of fault detection, isolation, and recovery can be done in milliseconds with only small disturbances imposed on the system. Some study was done to examine the availability of superconducting disconnects and its performance. The finding is summarized in Appendix A.

Table 1 shows the sizing scenario for Architecture 1. Engines, generators, and AC/DC converters are sized by the one engine failure scenario according to NASA studies. The existence of redundant feeders, which increases the connectivity between bus and propulsor, allows the propulsors to be optimally sized for their own redundancy. Given the large number of propulsors, they are sized such that 14 out of total 16 propulsors can provide the full take-off power. Outer buses are sized the same as their connected generators. The inner bus is sized slightly larger to supply eight propulsors connected to it through primary feeders. While primary feeders are sized to the same rating as propulsors, redundant feeders are sized to spread the remaining power from its connected bus to propulsors that are primarily supplied from the other bus.

### 2.2.3 Modular Stack DC Architecture with Current Source (Architecture 2)

An alternative architecture to reduce weights of circuit breakers is to apply the Modular Stack DC (MSDC) technology developed by GE (sponsored by RPSEA), which connects all the generators and loads in series and uses a by-pass switch to short out the faulted branch (Refs. 5, 6, 7, and 8). The concept of MSDC is shown in Figure 4. Basically it is a current source architecture where generator converters run in a current control mode. Generators and motors are connected in series and a ring bus is formed. The bidirectional Bus Interface Units (BIU) interface generators and motors to the bus and provide the bidirectional power flow capability. For line-line faults occurring on any of the branches, instead of isolating the faulted branch using a circuit breaker, a bypass switch in parallel with the branch will be closed to bypass the faulted branch. Therefore, no DC circuit breakers are needed on branches, while lighter bypass switches and disconnects can do the job of fault isolation.

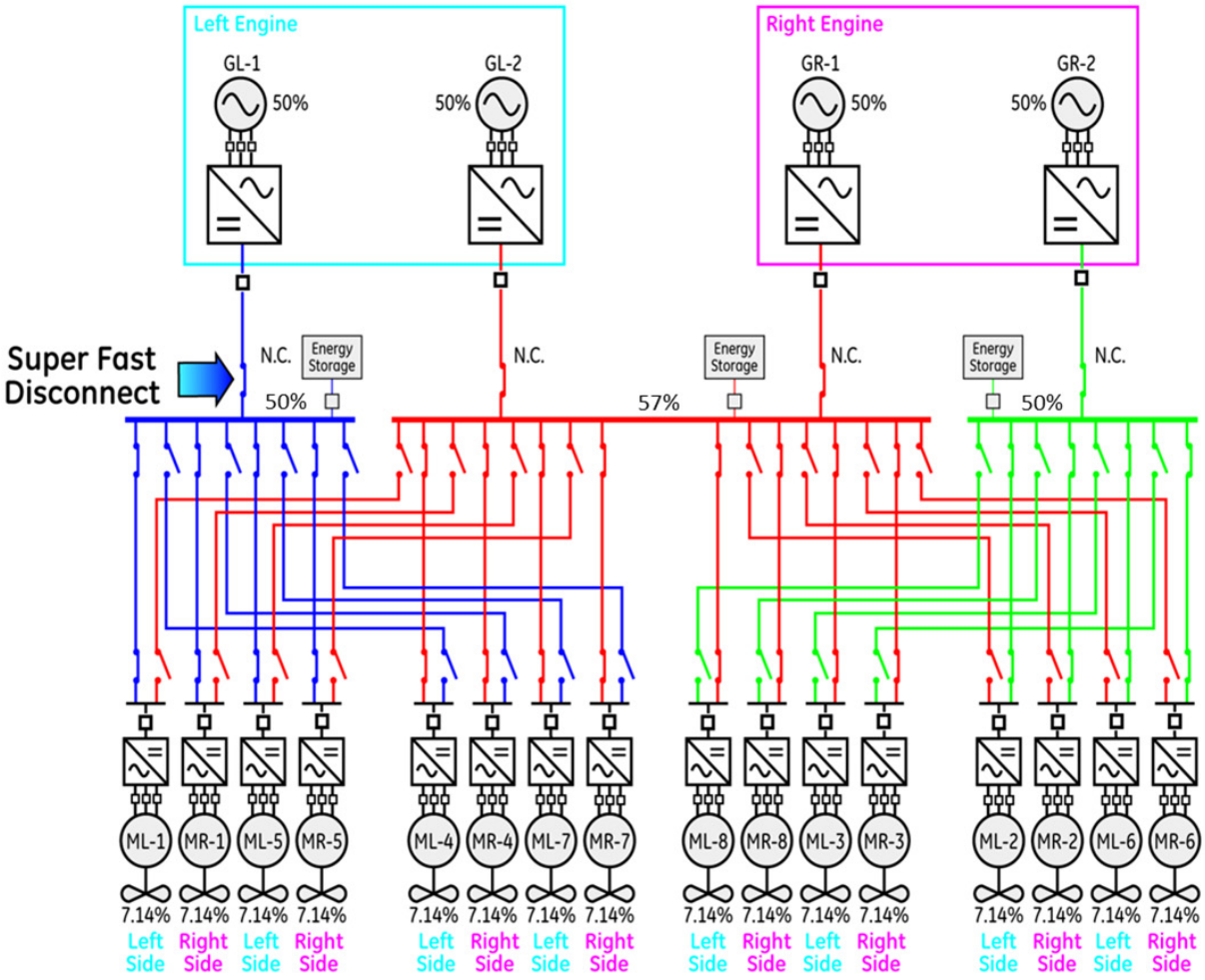


Figure 3.—Architecture 1, Voltage Source Architecture, 3-Bus Multi-Feeder Architecture with Integrated FCL, Power Conversion, and Circuit Breaker Function

TABLE 1.—SIZING SCENARIO FOR ARCHITECTURE 1

| Component | | Sizing method |
|---|---|---|
| Engine | | 1 engine failure |
| Generator/converter | | 1 engine failure (100%/2) |
| Transmissions lines | | 1 engine failure (100%/2) |
| Bus | Outer bus | 1 engine failure (100%/(3-1)) |
| | Inner bus | 8 propulsors (100%/(16-2) * 8) |
| Feeder | Primary feeder | 1 propulsors (100%/14) |
| | Redundant feeder | 1 engine failure (50% – 7.14% * 4)/4) |
| Propulsor (drive/motor/fan) | | 2 propulsor failure (100%/14) |

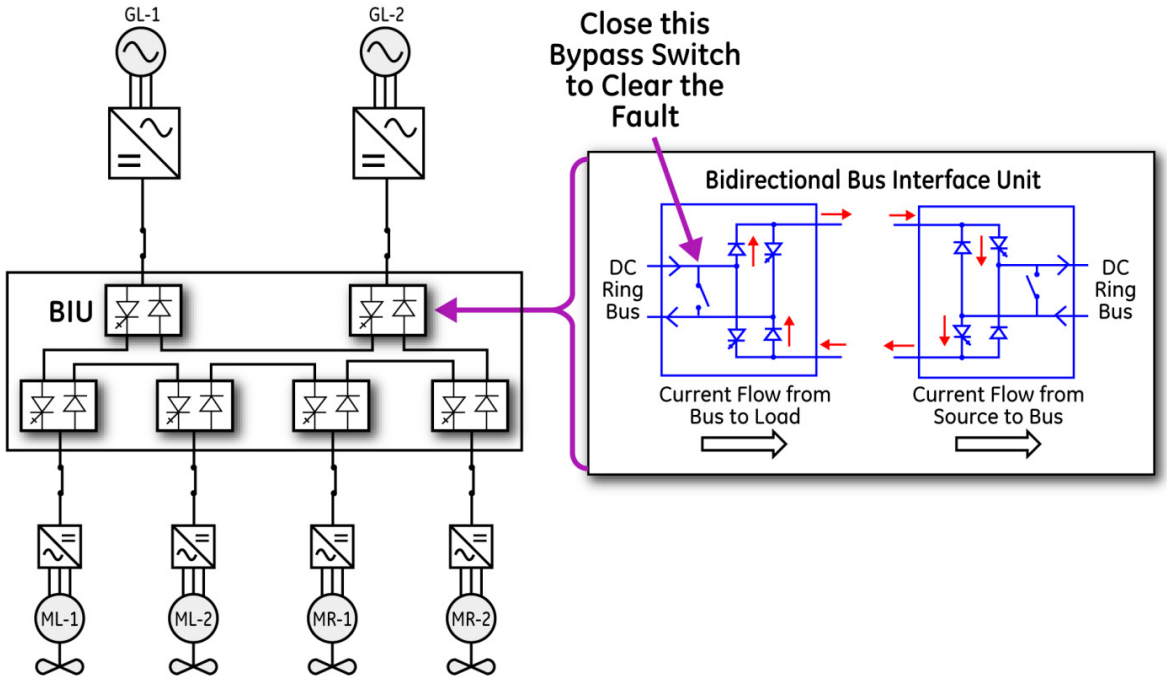


Figure 4.—Current Source Concept for Architecture 2

Table 2 indicates the scenario that sizes each element in the system. The size of each element is indicated in terms of percentage of 25 MW, the required power for rolling take-off. As is outlined in the table, a single engine failure scenario dominates all other off-nominal operations for this architecture.

Just like the concept of multiple buses in Architecture 1, when adopting MSDC more than one ring bus will be used to provide redundancy and improve system reliability. Figure 5 shows the system layout with this concept applied. The architecture consists of four subsystems. Each subsystem consists of one generator, one AC/DC converter, one bus with an associated energy storage device, and four propulsors with AC/DC converters as motor drives. All of the AC/DC converter and DC/AC converters are connected to the ring bus via a BIU. The BIU can control the power flow between the converter and the ring bus which is carrying constant current.

In normal operation, the load can be distributed among the 16 propulsors, e.g. each generator feeds 25 percent of the system power to each ring bus. During the one engine failure scenario, the two normally open switches between the two middle ring buses will be closed. And the two normally close switches in the two ring buses will open. Thus, the two middle ring buses forms a new ring bus. Via this new ring bus, one of the generators powered by the healthy engine can keep feeding power for the middle 8 propulsors. In other words, 12 propulsors can continue working together to provide the required power for rolling take-off.

If a line-to-line short circuit fault occurs in the system, such fault can be cleared by the BIUs and by-pass switch. For example, if feeder cable is shorted, the AC breaker in the propulsor will open to cut energy fed from the fan. At the same time, the by-pass mechanism in the BIU will also close to stop energy from the ring bus. After the feeder is bypassed by the BIU, the normally open switch will close to fully isolate the fault. Since in the ring bus system all of the generator and loads are connected in series and the operation of BIU and switch will not interrupt the current in the ring bus, the other propulsors will not even sense such fault. If the ring bus is shorted, the ring bus needs to be shut down by closing all of the BIU connected to the ring bus. In the worst case, (a permanent short circuit fault occurs inside the ring bus), the whole ring bus will be shut down, which equals to one engine failure fault.

TABLE 2.—SIZING SCENARIO FOR ARCHITECTURE 2

| Component | | Sizing method |
|---|---|---|
| Engine | | 1 engine failure |
| Generator/converter | | 1 engine failure (4 or 8 propulsors) |
| Transmission lines | | 1 engine failure (4 or 8 propulsors) |
| Bus | Outer bus | 1 engine failure (4 propulsors) |
| | Inner bus | 1 engineer (8 propulsors) |
| Feeder | | 1 propulsors (100%/14) |
| Propulsor (drive/motor/fan) | | 1 engine failure (100%/12) |

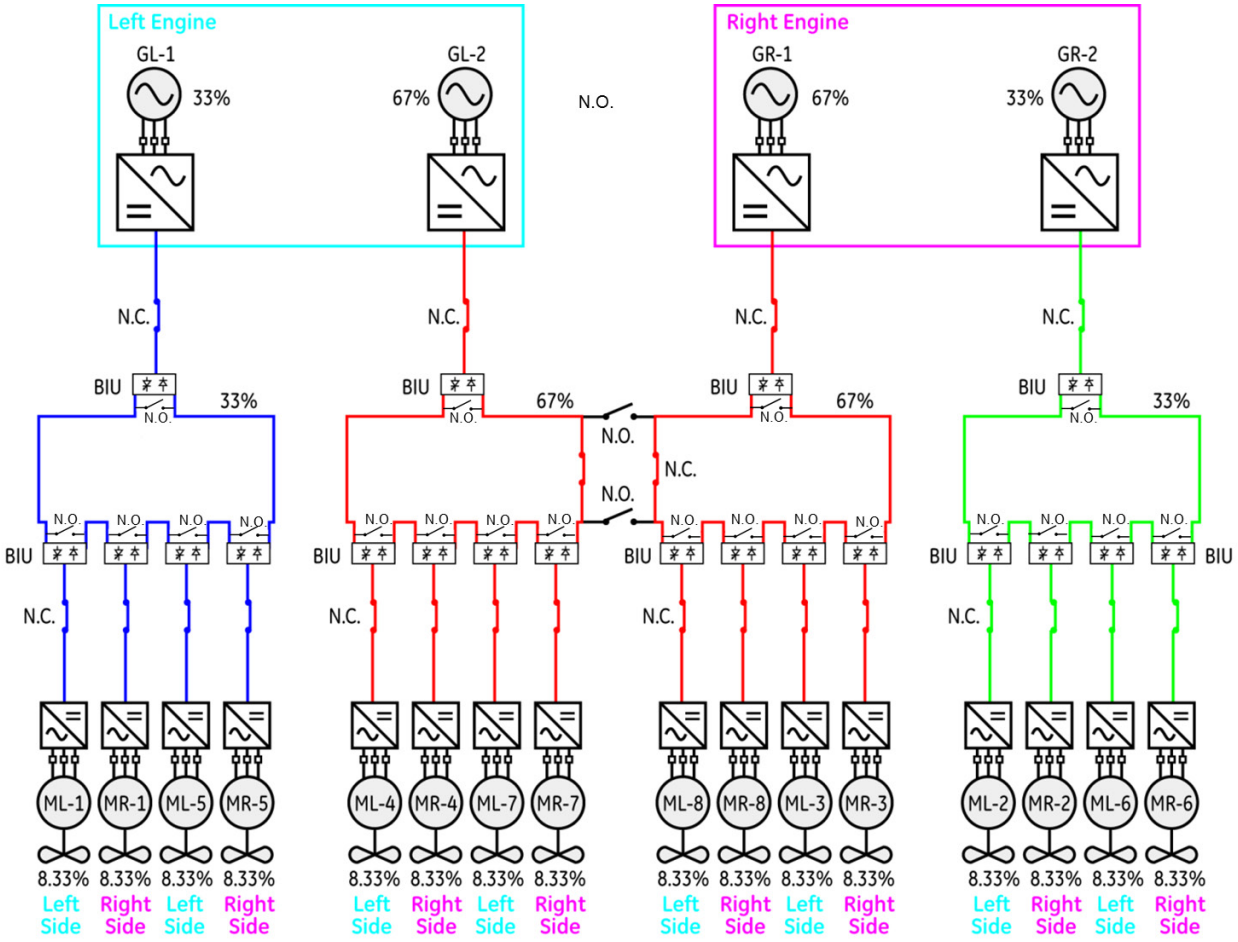


Figure 5.—Current Source Breaker-Free Architecture 2

If a line-to-ground fault occurs in the system, a fault current may flow through the ground path. In this case, the ring bus connected with the faulty point needs to be shut down by the BIU, following a similar method to the one mentioned above. Part of the system connected to the ring bus can be recovered after the fault is cleared by operating the corresponding disconnects.

Compared with the voltage source architectures, no DC breaker is used here. All of the fault can be cleared by BIU and by-pass switches. This is the key reason why the weights of circuit breakers can be reduced in the ring architecture.

### 2.2.4 Architecture Component Breakdown

Table 3 breaks down the proposed two architectures and the Baseline Architecture in terms of the number and power rating of each component.

### 2.2.5 Architecture Weight Assessment

The weight of two architectures is assessed and compared against the Baseline Architecture. The weight model for individual components will be updated in the following report sections; in this early study phase the component density values and assumption adopted in the earlier NASA study were used (Ref. 1). The calculated power density values in kilowatt/kilogram are summarized in Table 4 (Ref. 1).

Figure 6 shows the weight breakdown for three architectures. Compared with the Baseline Architecture, Architecture 1 reduces the system weight by about 370 kg, while Architecture 2 reduces by 160 kg. And the weight reduction is mainly from the protection represented by the yellow and green bars. As discussed earlier, Architecture 1 uses lighter fast disconnects to replace many of the circuit breakers, while Architecture 2 adopts a breaker-free architecture to reduce the protection weight.

TABLE 3.—ARCHITECTURE COMPONENT BREAKDOWN

| Component | | Baseline | | Arch 1-VSI | | Arch 2-CSI | |
|---|---|---|---|---|---|---|---|
| | | Count | Rating | Count | Rating | Count | Rating |
| Machines | Generators | 4 | 50% | 4 | 50% | 4 | 2-33%, 2-67% |
| | Motors | 14 | 8.33% | 16 | 7.14% | 16 | 8.33% |
| Converter | AC/DC | 4 | 50% | 4 | 50% | 4 | 2-33%, 2-67% |
| | DC/AC | 14 | 8.33% | 16 | 7.14% | 16 | 8.33% |
| Protection | AC CBs | 4 | 50% | 4 | 50% | 4 | 2-33%, 2-67% |
| | | 14 | 8.33% | 16 | 7.14% | 16 | 8.33% |
| | DC CBs | 8 | 50% | 4 | 50% | | |
| | | 56 | 28-8.33%, 28-5.56% | 16 | 7.14% | | |
| | Disconnects | | | 4 | 50% | 4 | 2-33%, 2-67% |
| | | | | 64 | 32-7.14%, 32-5.36% | 16 | 8.33% |
| | BIUs | | | | | 4 | 2-33%, 2-67% |
| | | | | | | 16 | 8.33% |
| Cable | Transmission | 4 | 50%, 2-30 m, 2-40 m | 4 | 50%, (2-30 m, 2-40 m) | 4 | 2-67%, 30 m; 2-33%, 40 m |
| | Feeder | 28 | 14-8.33%, 14-5.56%, 5 m | 32 | 16-7.14%, 6-5.36%, 5 m | 16 | 8.33%, 5 m |
| | Bus | 3 | 50%, 2-5 m, 1-10 m | 3 | 50%, 2-5 m, 1-10 m | 4 | 2-67%, 5 m; 2-33%, 5 m |

TABLE 4.—COMPONENT POWER DENSITY
IN KILOWATT/KILOGRAM

| Component | Power density (kW/kg) |
|---|---|
| Generators | 78.5 |
| Motors | 47.1 |
| Converters | 40 |
| DC circuit breakers | 200 |
| AC circuit breakers | 350 |
| BIUs | 200 |
| Disconnects | 600 |
| Cables | 500 A/kg/m |

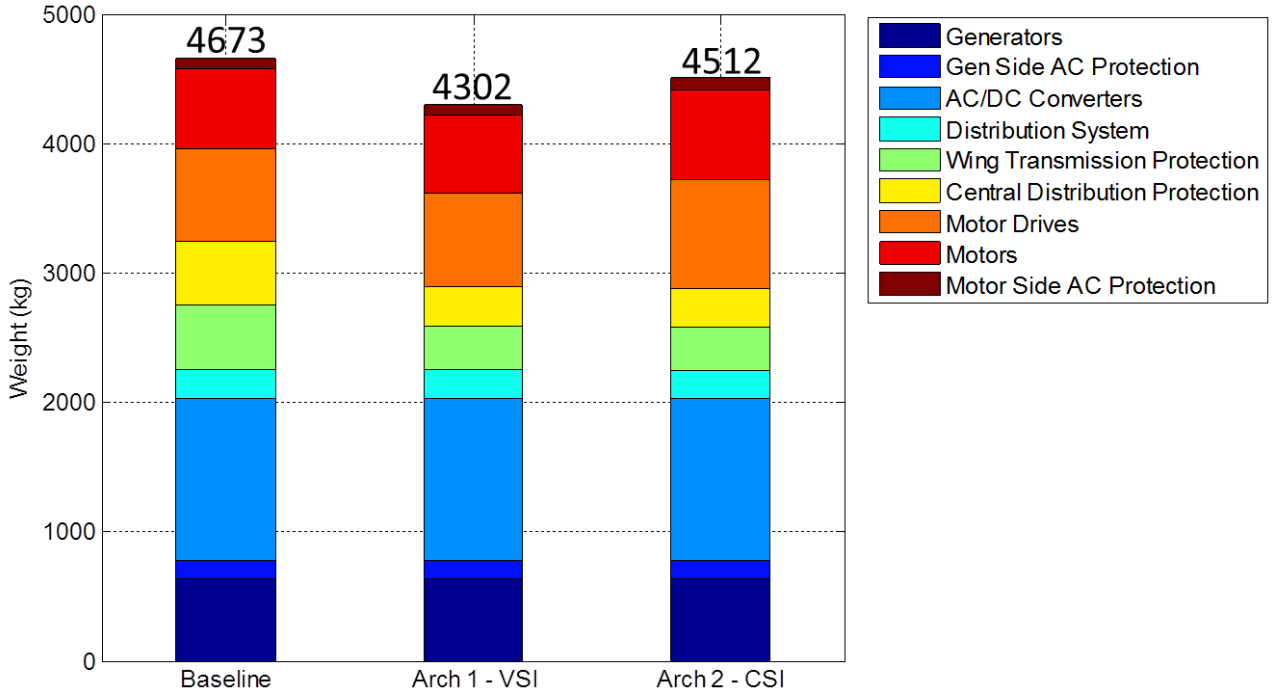


Figure 6.—Initial Weight Breakdown for Three Architectures

The weight of Architecture 1 is smaller than that of Architecture 2. This is because redundant feeders in Architecture 1 provide power rerouting capability for propulsors during a bus / generator / engine failure. This allows a reduction in propulsor size. This power rerouting capability is hard to implement in Architecture 2 with ring buses, especially during a bus failure.

Figure 6 indicates that more than 50 percent of the system mass comes from AC/DC and DC/AC converters. Considering the preferred DC grid architecture of the TeDP electrical system, it may be worth investigating DC electric machine technologies. In this way, it may be possible to complete DC architectures without the use of power electronics and possibly achieve a significantly lower system mass.

One option is the common DC machine comprised of a DC stator field winding, rotating armature coil, rotating commutator, and stationary brushes. Challenges exist with the design of a high voltage, high-speed commutator. In this machine, an AC voltage is generated within the rotating armature winding and the AC voltage is rectified by the rotating commutator and stationary brushes. Conventional DC machines generally operate at DC voltages below 1 kV because the solid conductor commutator segments, which lie next to each other on a cylindrical rotor, must be electrically insulated from each other. Electrical arcing between the commutator segments will be more difficult to prevent at higher voltages.

#### 2.2.5.1 Generator Option

Another option is the DC homopolar machine, which utilizes the Lorentz force between a constant radial unidirectional magnetic field and an axial current flowing within the winding on a rotor. This type of machine does not require a commutator because no alternating current or voltage is produced within the machine. However, brushes are still required to transfer the current from the rotor to a stationary wire. In addition, this type of machine is inherently a high-current, low voltage machine since the rotor winding is essentially a single turn coil. Thus it may be difficult to produce a brush to carry the high current necessary for this application. Two examples of this type of machine have been built (Refs. 9 and 10).

### 2.2.6 Architecture Efficiency Assessment

The first order efficiency assessment will be performed assuming consistent efficiency for components (generator, motor, and power converter) in different architectures, and it is assumed that there is no loss on superconducting cables and contactors. Then the assessment is about how many power conversion stages the power will flow through from generators to motors. For the baseline study, every unit power will flow through a total of five power conversion stages: generator side AC/DC converter, one transmission line solid-state circuit breaker, two feeder solid-state circuit breakers, and motor side DC/AC drive. For Architecture 1, there are a total of three power conversion stages since two feeder solid-state circuit breakers are replaced by hybrid breakers with superconducting contactors. For Architecture 2, power converters include: generator side AC/DC rectifier, generator BIU, motor BIU, and motor side DC/AC drive (a total of four power conversion stages with Architecture 2). With the above, the efficiency of Architecture 1 will be better than Architecture 2. Both them are better than the baseline.

### 2.2.7 Architecture Selection

The weight comparisons above estimate both Architecture 1 (voltage source architecture with fast disconnects) and Architecture 2 (Modular Stack DC Architecture with Current Source) were lighter than the Baseline Architecture, and that Architecture 1 is 210 kg lighter than that of Architecture 2. However, the relatively small estimated weight delta also requires that other metrics such as the bus voltage, flexibility, scalability, and technology readiness are considered to select one architecture for the following study.

In Architecture 1, the wing transmission, buses, and central distribution all operate at the same voltage level. While in Architecture 2 generator branch and motor branches are connected in series, wing transmission and bus voltage will be the sum of the connected motor branch voltages. Therefore, with the same voltage level of the motor converter, Architecture 2 will be with a higher bus and wing transmission voltage level. The insulation requirements will increase. As discussed in Section 2.3 and specifically Section 2.3.4, we propose to set the motor converter voltage to the maximum available blocking voltage of a single semiconductor device to optimize overall system efficiency. That voltage is estimated to be at least 5 kV based on certain projected assumptions. Then the bus voltage in Architecture 2 will be that voltage times the number of motor branches connected in a ring. When increasing the number of motors (propulsors) to scale up the system, a concern will be whether the high bus voltage reaches a value where the insulation becomes extremely challenging. (With the increase of voltage level, the design and control of electric field distribution under DC may become more challenging within both cables and cable joints and terminations. Due to the volume effect of insulation breakdown stress, moving towards higher voltage may require the increase of insulation, which can affect the overall size and weight of the system.)

Another advantage associated with voltage source type of Architecture 1 is actually demonstrated in the earlier NASA study. It is easy to increase the connectivity between generators and motors in a voltage source architecture to reduce the total power rating of propulsors. And considering the short distance of distribution cables required in the aircraft architecture, the trade of redundant feeders / transmission for reduced rating of propulsors usually brings in overall system weight benefit. This power rerouting capability is hard to implement in the ring architecture because of the series connection structure and the need for the interface unit, BIU.

A ring architecture has some attractive features for today's MV grid and it was adopted in GE's recent subsea program. First, it removes the need for a MVDC circuit breaker, which is a challenge with today's technology. Second, industry application usually prefers high transmission voltage (about 160 kV in GE's subsea program for example) to reduce the cable conduction losses, and the interface unit (BIU) in those applications can also be used to step down the voltage to a suitable level the load prefers. This function needs to be implemented by another stage of power converter in the voltage source architecture. So the BIUs are not additional components for the subsea application. However, with the assumption that the system under study is to be entirely cryogenic, we do not necessarily need to increase the transmission

voltage to reduce the thermal loss, and the entire system (including generation, transmission, and load) can run at the same voltage. Therefore, BIU is just an additional level of power conversion used to facilitate the ring bus structure and it washes out the "breaker free" feature of the ring architecture.

Due to the above reasons, the voltage source architecture (Architecture 1), shown in Figure 3, is recommended to use for this study. However, if some basic assumptions can be changed, the conclusions could be reversed, leading to some very interesting research topics for the future study. For example, if the DC motor can be used in the system instead of the synchronous machine, the DC/AC converter and AC/DC converter can both be replaced by simple DC/DC converters. The related benefits may not be obvious for the voltage source architecture, since the DC breaker is still needed to block the energy stored in the system's DC capacitors. However, this can bring much more benefits for the ring architecture, since the function of DC/DC converter can be integrated into the BIU. In other words, the weight and loss related to the DC beaker can be truly eliminated in the ring architecture. In addition, if a true bipolar force-commutated device becomes available, both the weight and loss in the DC breaker and BIU can be reduced significantly. This could also change the conclusion.

## 2.3 Initial DC Bus Voltage Range

Bus voltage is a critical parameter in future aircraft DC distribution systems which have a significant impact on system weight. Generally speaking for conventional conductors, higher voltage levels are desired as power demand increases. Increasing the voltage level allows the conductor current to decrease for the same power rating, which leads to smaller conductor dimension and lowers conductor weight. However, higher voltage levels require thicker insulation which contributes to an increase in system weight. With the assumption that the system under study is to be entirely cryogenic, the thermal loss / ohmic ($I^2R$) of superconducting cables and machines are negligible, a different thinking should be taken. Maximum power transmitted at high efficiency can be achieved by operating the system at an optimal voltage such that all anticipated currents through the superconducting cables are close to, but less than, the critical current (within safe margin), and the voltage losses in the dielectric are small. Furthermore, for aircraft application, cable insulation and electrical system layout must be designed appropriately considering Paschen's Law in order to avoid breakdown and partial discharge, especially in a cryogenic environment with lower air pressures. Given construction options with cryogenic cables and components, it may be desirable to operate the cryogenic system at pressures above ambient. It is expected that pressure structures will contribute more greatly to system weight than dielectrics materials within the pressurized environment. Due to the complications summarized above, the relationship between bus voltage and system weight is not expected to be monotonic (Ref. 1).

DC bus voltage selection needs a coordinated consideration of generator voltage and propulsor voltage. Voltage gain of power converters, which determines converter topology selection, depends on the voltage ratio of generator voltage over bus voltage or the ratio of bus voltage over propulsor voltage. Matching DC bus voltage and operating current appropriately with generator / propulsor voltage / current can minimize power conversion and simplify converter structure. It can, therefore, potentially reduce system weight and improve power efficiency. In addition, DC bus voltage level and generator / propulsor voltage level will determine voltage and current ratings of converter components, including semiconductor devices and passive filtering components.

DC bus voltage selection cannot be separated from DC system architecture design. Different system architectures may involve different power conversion technologies and different protection schemes, thus different switching, isolating, and current-limiting components.

Another important factor is the type of semiconductor devices that will be used in the system. It will be desired to understand the current density of different device technologies (like MOSFET, IGBT, IGCT, GTC and Thyristor) at different voltage levels. As shown in many studies (Refs. 11, 12, and 13), the electrical characteristics of the semiconductor devices change (sometimes drastically) when operated

at cryogenic temperature. The changes in both dynamic and static behavior are due to changes in physical parameters such as charge mobility, lifetime, etc. These changes depend on the operating temperature as well as the device internal architecture and their operating mode. GE is leading the adoption of silicon carbide technology, but since silicon carbide devices will not work well under a cryogenic environment and devices like silicon are well suitable for cryogenic temperature, those devices will be the main focus in the study. With the above-mentioned aspects, system architecture, converter technology, semiconductor devices, protection scheme, generator voltage, and propulsor voltage are all parts of the optimal system voltage selection equation.

Passive components such as capacitors and inductors also need to be optimized for operation in a cryogenic environment. Generally speaking the voltage breakdown strength of capacitors decreases, but their capacitance seems quite stable at low temperature (Ref. 13). Common inductor materials' core losses increase in a cryogenic application; therefore, it is best to avoid them (Refs. 14 and 15).

The manufacturability of the equipment also plays a major role in determining the optimal system voltage. Studies can show the theoretical optimal system voltage, but ultimately each piece of equipment must be producible. When studying the optimal system voltage, manufacturability metrics should be included so that the ability to produce the equipment is taken into consideration when optimizing (Ref. 1).

Overall, given the total power requirement of 50 MW, a systematic trade-off study is done in this task to obtain an initial range of DC bus voltage roughly within the 1 to 10 kV range. The study incorporates grid architecture design, converter topology selection, generator / motor voltage consideration, cryogenic electronics characteristics, superconducting cable characteristics, and power converter voltage consideration.

### 2.3.1 Generator / Motor Consideration

The entire electrical system is assumed to be superconducting and cryogenic and the electric generators and propulsion motors are assumed to be fully-superconducting, synchronous machines, including the wound rotor and stator windings (Ref. 15).

Generally superconducting electrical machines are built with an air-gap stator winding; in other words, iron teeth are not utilized between the coil sides of the armature winding. This is because the iron teeth would easily saturate given the very high magnetic field levels produced by the superconducting field winding. The coils are often still supported and insulated from each other using non-magnetic "teeth." However, there may be other ways to support the coils without using non-magnetic "teeth." An example coil supporting structure is shown in Figure 7 (Ref. 16). A stator tooth is represented by item 370, a stator coil is represented by item 380, and the machine frame is item 360. The stator yoke or back-iron, which is depicted just radially outward of the coils, may or may not be laminated magnetic material. Figure 8 (Ref. 16) shows an image of an air-gap winding in which item 110 refers to the armature winding placed within the air-gap between the stator yoke 180 and the rotor 220. A magnetic back-iron 180 is not strictly necessary, but it may be utilized to contain the amount of flux that fringes into the frame of the machine, thereby minimizing eddy current loss within the frame.

Several factors must be considered when selecting the voltage rating of the electric machines in the TeDP system, which is directly translated to the system's DC-bus voltage by a scaling factor. These factors include electric machine power density, efficiency, resilience to fault conditions such as short circuits, and system stability. The goal of the electric machine design for the TeDP system is to maximize the power density and efficiency of the electric machines, while maintaining acceptable short circuit and system stability conditions. However, the following fundamental analysis will provide rationale for why the voltage ratings of the electric machines have only a secondary effect on these critical system factors. The medium voltage range is very typical for conventional electric machines in the 1 to 10 MW range. Although insulation requirements will increase as the voltage increases, there is no evidence suggesting that the electric machine's coil construction or design will be limited by the assumed voltage range of this study.

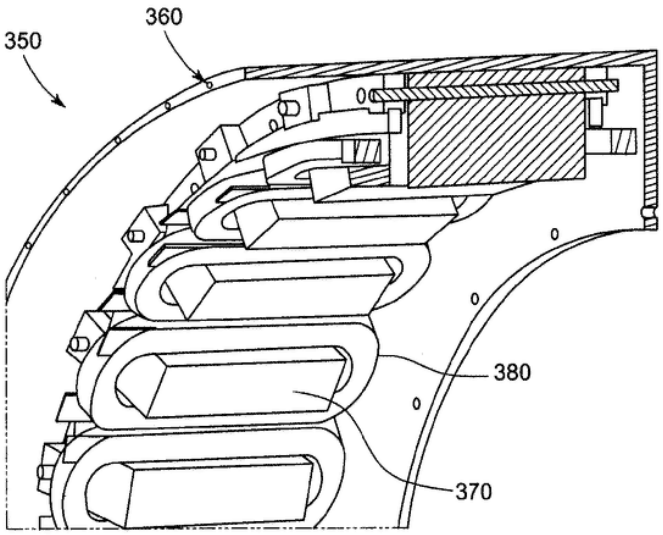


Figure 7.—Coil Supporting Structure for Air-Core Superconducting Stator Winding (Ref. 16)

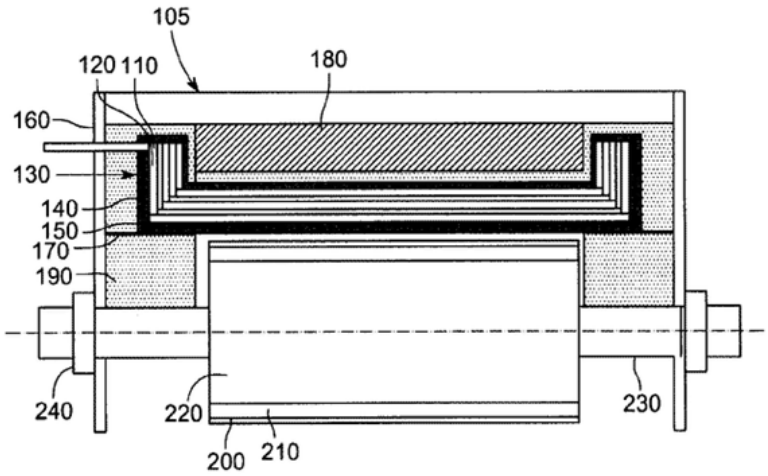


Figure 8.—Air-Core Superconducting Stator Winding (Ref. 16)

#### 2.3.1.1 Power Density

In order to maximize the power density (1) of an electric machine at a given speed, one must maximize the shear stress ($\tau$) within the air gap of the machine. Since shear stress (2) is directly proportional to the average air gap flux density ($\beta$) and armature current loading ($\sigma$), one should maximize both values within the cooling and current carrying capabilities of the SC wire utilized in the rotor and stator windings. Note that current loading refers to the amp-turns divided by the circumferential distance around the air-gap, and current density refers to the amount of amp-turns divided by the cross-sectional area of pure conductor within a coil.

The air gap flux density (3) and current loading (4) are proportional to the current density in the field winding and the armature winding, respectively. Air gap flux density is primarily driven by the amount of flux produced by the field winding. Therefore, it is assumed that the field and armature windings will operate at the current density and AC loss limits of the future state-of-the-art superconducting wire in order to maximize the power density of the electric machines.

As in any conventional electric machine, the armature phase voltage (5) is simply proportional to the rate of change of the air-gap flux times the number of turns per phase. If the number of turns per phase is

increased in order to increase the rated voltage of the machine, then the current per turn and the conductor area per turn must also decrease in order to keep the current density constant within the armature winding. The opposite is true if the voltage is decreased by decreasing the number of turns. In this way, the terminal voltage of the machine can be exchanged with the line current of the machine by changing the number of turns per phase. In addition, a similar exchange can be performed by changing the number of parallel circuits within the machine. Both methods of adjusting the rating of the machine do not affect the power density of the machine on a first order basis.

A secondary effect of the voltage rating on the power density of the electric machine is related to the amount of electrical insulation that is necessary between the machine's turns and phase windings. As the voltage increases, the amount of insulation increases, which decreases the amount of space available for current conducting wire. Thus the current loading may decrease. However, the decrease in current loading is much less than proportional to the increase in voltage. Therefore, the effect on power density is minimal as the voltage increases.

This study will use a baseline generator plus cooler power density of 34.6 kW/kg and a motor plus cooler power density of 20.9 kW/kg based on the mass estimates calculated in Reference 15 assuming a hypothetical BSCCO material for the superconducting wire.

$$\frac{S}{VOL} = 2\omega_m \tau \tag{1}$$

$$\tau = \sigma\beta \tag{2}$$

$$\beta = \frac{N_p \emptyset}{\pi DL} \tag{3}$$

$$\sigma = \frac{k_2 N I_a N_p}{D} \tag{4}$$

$$V_{LL} = \frac{2\pi f N \emptyset}{k_1} \tag{5}$$

| | |
|---|---|
| $S$ | electric machine apparent power (VA) |
| $VOL$ | air gap volume ($m^3$) |
| $\tau$ | shear stress (psi) |
| $\omega_m$ | angular speed of the rotor (rad/s) |
| $\sigma$ | current loading (A/m) |
| $\beta$ | average air gap flux density (T) |
| $N_p$ | number of poles |
| $\emptyset$ | flux per pole |
| $D$ | air gap diameter |
| $L$ | air gap length |
| $N$ | number of turns in armature circuit |
| $I_a$ | armature current |
| $f$ | frequency |
| $V_{LL}$ | line-to-line armature voltage |
| $k_1$ | winding scaling factor |
| $k_2$ | winding scaling factor |

#### 2.3.1.2 Efficiency

As stated in previous studies, the efficiency of the electric machines within the TeDP system will affect the weight of the cryogenic cooling components required, and, therefore, the power density of the overall system. As is the case with power density, the voltage of the superconducting electric machine has only a secondary effect on the efficiency of the machine.

The electrical loss within an electric machine can be thought of being driven by the same two "fields" that produce output power from the machine. In other words, electrical loss is dependent on current loading (or current density) and flux density.

AC loss within the superconducting wire is defined in Reference 15 as a combination of eddy current, hysteresis, and coupling eddy current losses. Note that all the loss components of the AC loss are dependent on current density and flux density. Eddy current and hysteresis loss within other magnetic structures within the machine are also driven by the flux density level. A conventional electric machine will possess the bulk of these losses within the iron stator and rotor cores. The modified Steinmetz Equation (6) is an example of the relationship between the loss in an iron material and the flux density level experienced by the iron material.

$$P_{LossCore} = K_h f^{\alpha} B^{\beta} + K_e f^2 B^2 \tag{6}$$

$P_{Loss\ Core}$ core (laminated iron) loss
$K_h$ hysteresis loss coefficient
$K_e$ eddy current loss coefficient
$f$ frequency
$B$ magnetic flux density

As stated previously, the voltage of an electrical machine can be varied by changing the number of turns without changing the flux density or current density levels within the machine. Therefore, the losses related to the flux density and current density levels of the machine can be isolated from the voltage of the machine.

This study will use a baseline generator plus cooler efficiency of 99.55 percent (roughly 99.95 percent motor only efficiency), and a motor plus cooler efficiency of 99.97 percent (roughly 99.997 percent motor only efficiency) based on the efficiency estimates calculated in Reference 15, assuming a hypothetical BSCCO material for the superconducting wire.

### 2.3.2 Cryogenic Electronics

Cryogenic Power Electronics is a definition that refers to power electronics equipment operated at very low temperatures. While the most common explored operative temperature is 77 K because it is quite easy to reach and maintain, the largest gain in both efficiency and size reduction may be achieved at higher temperatures, especially if the weight and efficiency of the cryocooler needs to be accounted for. Additionally, different materials have different optimal working temperatures (where optimal is intended as the temperature where they exhibit the lowest losses); therefore, an optimal system may be a one with subcomponents operated at different temperatures. This report lightly touches on the main power electronics components, highlighting benefits and downsides of their operation at cryogenic temperatures. Table 5 provides an example of the system weight impact of both component inefficiency and cryogenic temperature. This report does not consider operative temperatures that are not cryogenic even if it is suggested that a more extensive study, including a comparison with a high temperature system, can be done in the future.

TABLE 5.—CRYOCOOLER MASS EXAMPLE

| Cryocooler Mass vs. Efficiency (30% Carnot, 3 kg/kW input) | | | |
|---|---|---|---|
| 50 MW | Loss (kW) | Mass at 77 K (kg) | Mass at 100 K (kg) |
| 99.95% | 25 | 724 | 500 |
| 99.90% | 50 | 1,448 | 1,000 |
| 99.50% | 250 | 7,240 | 5,000 |
| 99.00% | 500 | 14,481 | 10,000 |
| 95.00% | 2,500 | 72,403 | 50,000 |
| 90.00% | 5,000 | 144,805 | 100,000 |

#### 2.3.2.1 Capacitors and Insulators

The behavior at cryogenic temperatures of capacitors strongly depends on the material chosen as dielectric. Polypropylene, polycarbonate, and mica exhibit very good behavior at cryogenic temperature (same capacitance and smaller dissipation factor) while tantalum exhibits an increase in dissipation factor (Ref. 13). Other material (Ref. 17) exhibits a much larger breakdown voltage. It is also suggested the use of cryogenic liquids as a good material for cryogenic insulators (Ref. 18).

#### 2.3.2.2 Inductors

The behavior at cryogenic temperatures of magnetic materials strongly depends on the magnetic material considered. In published work (Ref. 14) it has been found that for some materials permeability decreases as temperature decreases (for example ferrite and Kool Mu), others remain constant (for example MPP and High Flux), while the material resistance decreases as the temperature decreases (leading to increase in eddy currents induced losses) for all the material considered. The windings of the inductor will produce much less losses; therefore, the total losses of an inductor in cryogenic environment are comparable with total losses of the same inductor at room temperature.

Inductor for electromagnetic interference (EMI) shielding becomes much more effective at cryogenic temperature (given the fact that the magnetic material is more lossy at cryogenic).

It must be noted that the materials considered in literature are designed for room temperature and above; a magnetic material for optimized performance at cryogenic temperatures can be designed. So, it can realistically be predicted that in the near future, given the need, such a material can be designed and high efficiency cryogenic inductors could be produced.

#### 2.3.2.3 Semiconductors

This section presents an overview of the two most popular semiconductor materials, and the two most common devices structures and their expected behavior in a cryogenic system. The two materials considered are silicon carbide (SiC) and silicon (Si). Other materials that may be used to manufacture switching devices are not considered in this report because it may have fallen in disuse (such as germanium), is not currently considered for high power application (such as GaN), or is too early to be considered (such as diamond). Heterojunctions are also not considered.

##### 2.3.2.3.1 Silicon Carbide (SiC)

Silicon carbide material is a very promising material for high performance switches in power electronics. This material, due to its large band-gap and higher maximum operating temperature, exhibits an excellent switching behavior and quite low conduction losses, making it desirable for both high frequency and high power applications. In addition, this technology is currently entering the market with commercially-available product grade components.

Given the high performance behavior of this material, it has been considered for this application but ultimately rejected for cryogenic applications.

The performances of this material degrade as the operative temperature falls. This degradation has been observed for two structures, Schottky diodes (Ref. 19) and MOSFETs (Ref. 20), and, without going into details, it can be attributed to the increase of the trapped-electron density that occurs when the material temperature decreases.

SiC have been observed to display a drop in breakdown voltage capability as the temperature decreases.

#### 2.3.2.3.2 Silicon (Si)

Silicon is the most common material used for fabrication of power electronics switches. It is used for both high frequency applications and high power applications. This material is so commonly used for its availability, its properties, and the available know-how that has been created after many years of its use. While at room temperature and above it does not perform as advantageously as SiC material does, especially at medium power high frequency applications, it still remains the material of choice for high power applications, and any other cost sensitive applications. It has been shown in numerous works (as the latest review shows (Ref. 21)) that the behavior of this material greatly improves, in terms of lower losses (both conduction and switching) and switching speed, as the operative temperature decreases. The improvements are not monotonically related to the operative temperature: depending on the structure and the doping level, the devices built out of silicon exhibit an optimal temperature that could be between 70 and 200 K.

Si have been observed to display a drop in breakdown voltage capability as the temperature decreases. The breakdown capability drops to about 70 percent of its nominal value (at room temperature) when the operative temperature is about 77 K (Refs. 11 and 22).

##### 2.3.2.3.2.1 MOSFET

The MOSFET is generally a majority carrier device, which means that the conduction is associated with a resistive-like behavior, and the charge flow interruption is not associated with carrier lifetime. Because the mobility of the electrons increases as the temperature decreases, in this structure the conduction losses greatly decreases as the temperature decreases.

Figure 9 from Reference 12 shows the great improvement (in terms of much smaller on-resistance) when the device is operated at low temperatures.

The switching losses and speed are not affected as much as the conduction losses, at least for a traditional MOSFET structure.

It has been reported that a cool-MOS structure exhibits large advantages for both conduction losses (Ref. 22) and switching losses (Ref. 23).

##### 2.3.2.3.2.2 IGBT

The IGBT structure is mostly minority carrier device structure. This structure is designed to conduct large currents in a reduced area, making this the device of choice when high power density is required. The conduction is associated to both carrier mobility and carrier lifetime, and its switching behavior is associated mostly with carrier lifetime.

As the temperature decreases the mobility increases—making the “resistive-like” conduction losses decrease—but the lifetime decreases—making the conduction losses associated with carrier density increase. As these two phenomena are in opposition, this device structure exhibits an optimal working temperature where the mobility is high and the lifetime is not too low (Ref. 11).

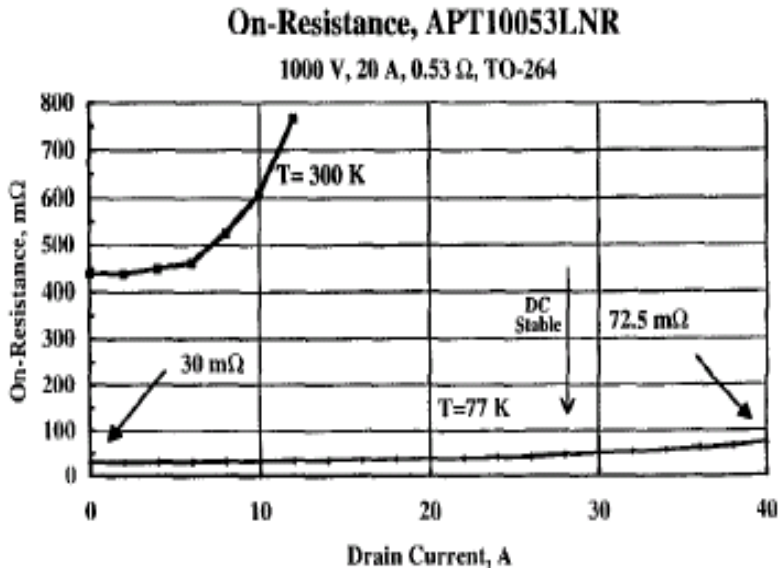


Figure 9.—MOSFET On-Resistance Versus Current for 77 and 300 K

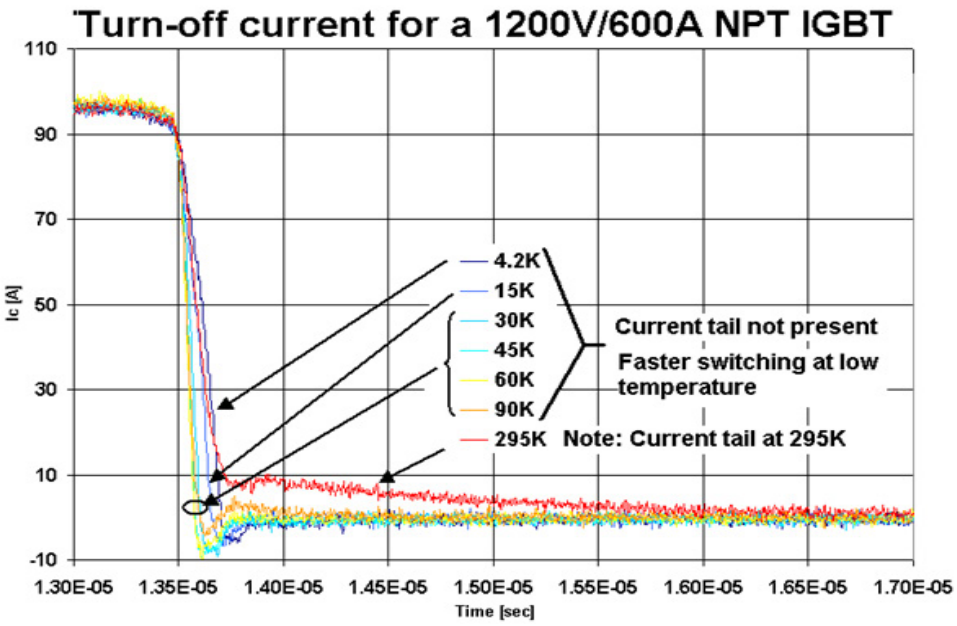


Figure 10.—IGBT Turn-Off as Function of Temperature

As the switching behavior benefits from a shorter lifetime, the switching time and switching losses decrease as the temperature decrease, making possible the use of this device at high frequency and high power.

Figure 10 shows the faster switching time (Ref. 24). It also shows that there is an optimal temperature at which the device is the fastest; above or below this temperature the device performances degrade. Figure 11 shows that a similar behavior applies for conduction losses. The device exhibits an optimal temperature. It must be noted that different IGBTs exhibit different optimal temperatures and different gains—this is an indication that the performances are connected with doping levels and device design. An IGBT device can be designed to have optimal performances at cryogenic temperatures.

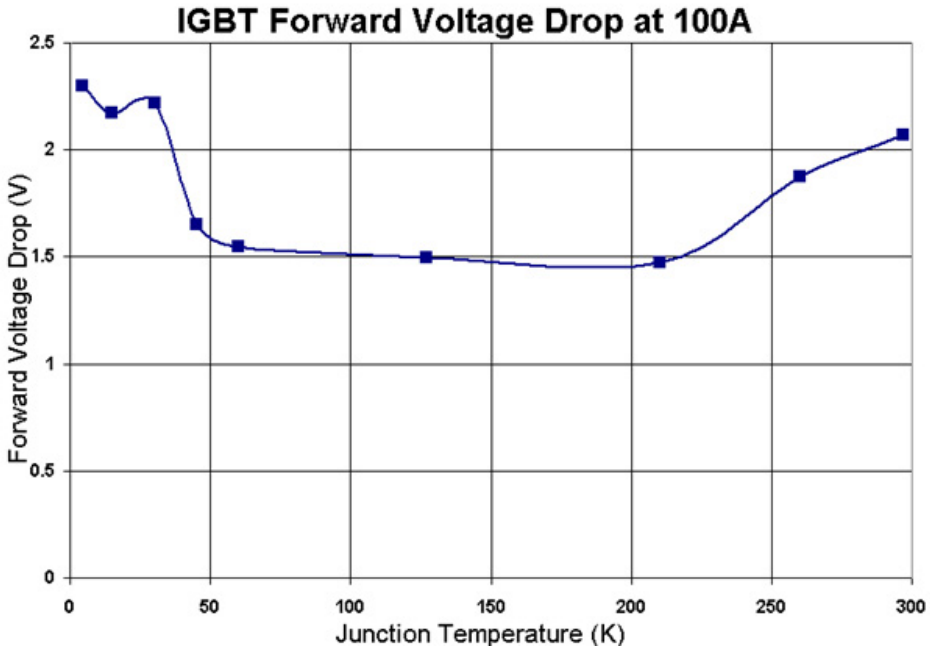

Figure 11.—Conduction Losses as a Function of Temperature

#### 2.3.2.3.2.3 Comparison

In order to select the proper component as MOSFET or IGBT structure, a comparison of losses and cooling must be done.

MOSFETs behave as a resistor; therefore, if they are paralleled, not only the losses per device decrease, but the system efficiency improves. This is not true for the IGBTs—as the conduction losses are proportional to the current that flows in them, paralleling multiple devices does not improve the system efficiency; it only reduces the power loss per device. This is true at any temperature. For this comparison only, structures with same active areas are considered.

Figure 12 shows a comparison of IGBT and MOSFET performances where the choice of the proper structure depends on the cooling removal capability. Figure 12(a) illustrates that with the choice for the cooling capability system represented, the MOSFET can manage more power than the IGBT for the same amount of losses; while Figure 12(b) shows the opposite—if the system can remove larger losses, than the better choice will be the IGBT.

Figure 13 shows a comparison between conduction losses of IGBT and MOSFET. The data for the IGBT have been measured, while the data for the MOSFET have been extrapolated from previous works.

It must be noted one more time that, if massive paralleling is considered, then the MOSFET structure will always be the choice. Massive paralleling will bring additional issues such as signal coordination, device selections, layouts, etc. that may make this approach unrealistic.

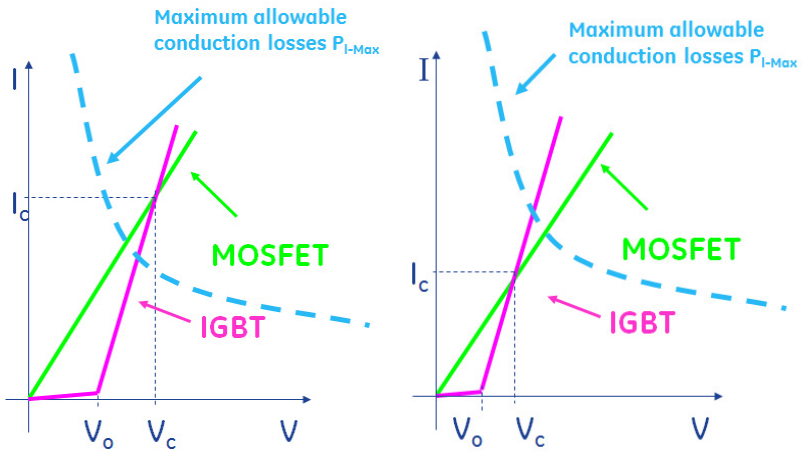


(a) MOSFET Better Performing (b) IGBT Better Performing

Figure 12.—Comparison of IGBT Performance and MOSFET Performance

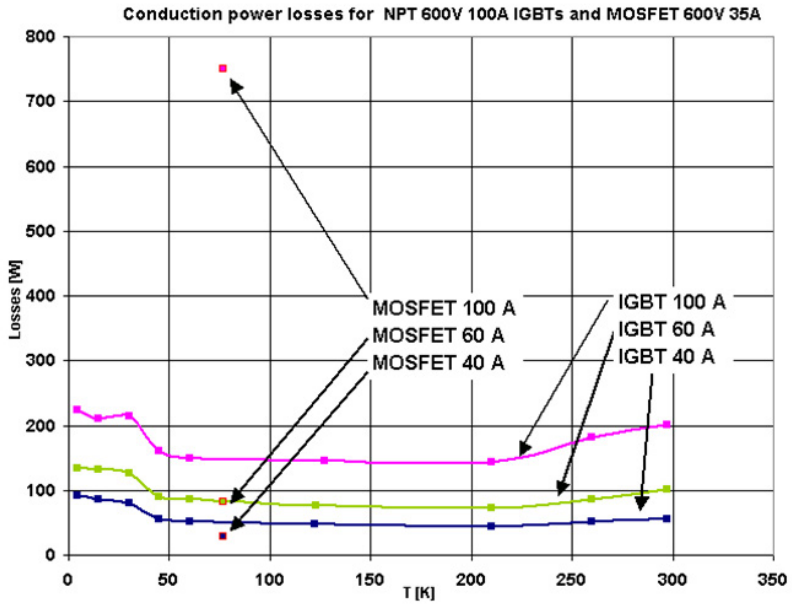


Figure 13.—Conduction Losses; MOSFET IGBT Comparison

When operating at cryogenic temperatures, the maximum power that can be removed from the junction increases. This is due to the fact that the thermal conduction of silicon increases as the temperature drops, making it easier for the heat to reach the cryo-bath, therefore, limiting the junction temperature rise for same heat produced. This allows for larger maximum currents that the device can carry (as shown in Figure 14).

Figure 15 shows the calculated thermal conductance and specific heat for silicon as a function of temperature according to Reference 25.

As mentioned in the previous section, an IGBT structure gains even during switching performances. As the temperature drops, the lifetime of carriers decreases making the switching transition much faster, therefore, allowing for higher operational frequencies and higher power capabilities.

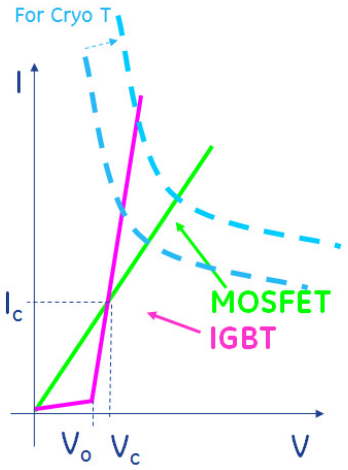


Figure 14.—Effect of Cryogenic Temperature on Maximum Power Management

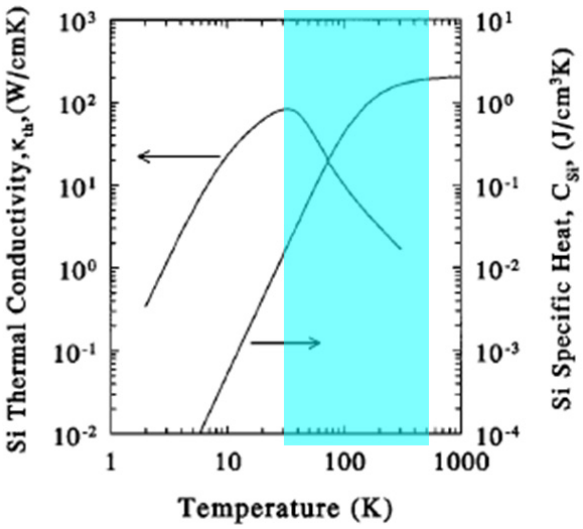


Figure 15.—Thermal Quantities as Function of Temperature

In general, it is possible to state that as the temperature is decreased, a MOSFET structure exhibits the most improvement during conduction, while the IGBT structure exhibits less improvement during conduction, but a much improved transition time and transition losses.

Figure 16 represents in general terms the effect of lowering the temperature on the two structures: at room temperature the MOSFET has low switching losses and high conduction losses, the IGBT has high switching losses and low conduction losses. As the temperature decreases the switching losses of the MOSFET decrease a little, but conduction losses decrease a lot. The opposite is true for the IGBT.

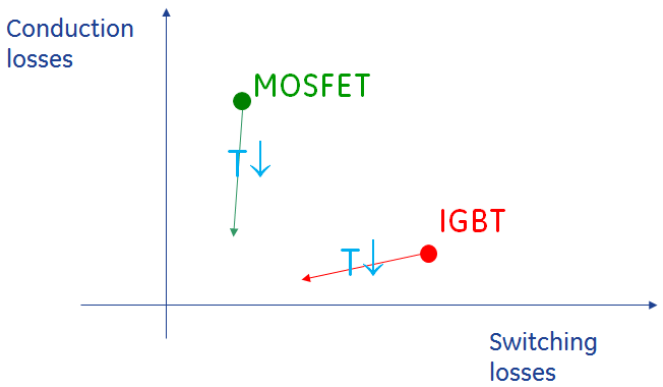


Figure 16.—MOSFET and IGBT Losses as a Function of Temperature

#### 2.3.2.3.3 Doping Effects

The doping level has a large effect on the optimal operational temperature of the device as well as the overall performances. As the temperature decreases and carrier lifetime decreases, the concentration of ionized dopant also decreases, culminating in carrier freeze-out where there are no more charges available for conduction. This phenomenon is prevalent in minority carrier devices. In order to counter-balance this effect, a device with larger doping level may be more beneficial, especially at deep cryogenic levels.

#### 2.3.2.3.4 Semiconductor Selection Conclusions

In conclusion, for cryogenic applications at high power and high voltage, when massive paralleling is not considered, the semiconductor device of choice is the Si IGBT optimized for low temperature operations (it is difficult to compare with coolMOS given the fact that only two works have been found—one does not cover transition times and losses (Ref. 22), and the other one (Ref. 23) is dated). As the device will be able to carry much more current than it can at room temperature but it will be able to block less voltage (about 30 percent less) than it could at room temperature, it is advisable that the topology of choice will take advantage of these new characteristics: high current capability, lower voltage capability, and higher switching frequency capability. The cryogenic temperature of choice will be addressed in the following sections.

### 2.3.2.4 Cryocoolers

Cryocooling is the most important reason that kept and still keeps cryogenic power electronics from entering the market. Most of the works on this topic focus on the benefits introduced by the semiconductor devices, some focus on the benefits and behaviors of the passives, and very few on the physics of cryocooling and the power balance involved at system level.

If the cryo-bath is kept at 77 K and the heat to be extracted is rejected at 300 K (room temperature), the Carnot cycle Coefficient Of Performance (COP) (not to be confused with efficiency) is only 34 percent. Considering that today's practical coolers exhibit a COP of about 30 percent of the Carnot cycle, it is clear that a realistic COP is about 10 percent, which means that for 1 W of heat to be extracted at 77 K and rejected at 300 K the system will consume 10 W, making the total losses 11 W. The losses to be compared with a system operating at room temperature are 11 W and not 1 W. As described, it makes it very difficult to build a cryogenic power electronics system with a clear advantage over a traditional system. For example, with 2.1 percent loss as the target, the power converters at room temperature need to be designed with 97.9 percent efficiency, while the power converters at cryo-temperature need to be designed with 99.8 percent efficiency (0.2 percent loss) since 2 percent power (10X) is needed to reject the heat to room temperature.

Because of the nature of the Carnot cycle and cryocoolers, the COP drastically increases as the cryogenic temperature increases; for example, if the cryo-bath is at 150 K and rejects at 300 K, the COP of the Carnot cycle is 100 percent and assuming same percentage of the Carnot cycle COP of 30 percent (even if it improves for a smaller variation of temperatures), it brings the overall COP to 30 percent. In this new example about 3.5 W will be needed to remove 1 W, bringing the total losses to 4.5 W: a much smaller number than the first case.

A breakeven plot of required efficiency of a device operating at 150K versus its efficiency at room temperature is reported in Reference 26. For example, if room temperature device efficiency is 80 percent, and it is cooled down with a Gifford-McMahon cycle, its minimum efficiency needs to be about 95 percent; if it is cooled with Stirling cycle it needs to be 90 percent.

#### 2.3.2.5 Power Electrics Conclusions (Device, Temperature, and Voltage)

This short study did not take into consideration the use of SiC material at room temperatures or above. While such a study will be very helpful, and the authors wish it could be done in the near future, it is outside the scope of this work. Additional complications introduced by such a study will be the losses in the connectors' cryo-to-room-temperatures in terms of conduction losses and added losses rejected into the cryogenic bath, and the losses of the new cooling system to keep the SiC within an acceptable temperature.

The use of cryogenic environment will not only allow power savings in the single elements, but will also allow the overall system size reduction by the use of small passives (such as capacitors and inductors) by enabling much higher switching frequencies. Additionally semiconductor devices, as well as passive elements, have higher reliability and are more robust to over currents when operated at cryogenic temperatures than at room temperature.

In conclusion, for the semiconductor devices, it is recommended the use of Si IGBT optimized for a high cryogenic temperature (i.e., 150 K). The IGBT should be rated for about 5 kV at cryogenic temperatures (see study on topology efficiency) and kAs level. While such devices cannot be found today, it is quite realistic extrapolating that they will exist in the near future. (There are currently devices rated for 6.5 kV at room temperature and devices rated for several kA at temperatures larger than 300 K.)

### 2.3.3 Cable Consideration

Superconducting wire has changed the industry with its revolutionary ability to conduct over 100 times the electrical current of conventional wire. The high power density of superconducting wire dramatically reduces the size, weight, and overall cost of large-scale electrical systems, and also increases the efficiency of the electrical systems compared with systems based on traditional copper wire.

HTS cables use tapes or wires made of superconducting materials as current carrying elements. $Bi_2Sr_2Ca_2Cu_3O_{10}$ (BSCCO) with a critical temperature of 110 K and $YBa_2Cu_3O_7$ (YBCO) with a critical temperature of 92K are commercially available superconductors used in HTS cable.

BSCCO as the first generation HTS wire has been produced in multi-filamentary structure in silver. BSCCO wire is available in km length with a current density of 100 A/mm$^2$ and above at 77 K.

YBCO as the second generation of HTS wire has been produced mainly in the form of a thin, wide, multilayer tape. YBCO tape is currently available in hundreds of meters length with a current density of 100 A/mm$^2$ at 77 K. YBCO wire is fabricated by an automated, continuous process using thin film deposition techniques, similar to those used in the semiconductor industry. Therefore, YBCO has inherently better price / performance ratio than BSCCO.

Alternatively, magnesium diboride ($MgB_2$) with a critical temperature of 39 K is used for superconducting cables operated at lower temperatures. $MgB_2$ wire has been produced in multi-filamentary structure in matrix. $MgB_2$ wire is available in km length, with a current density approaching 1000 A/mm$^2$ at 20 K.

SuperPower and American Supercondutor (AMSC) are the two major manufacturers of produce HTS wire.

For SuperPower wire, the total wire thickness is only 0.095 mm. It uses Surround Copper Stabilizer (SCS) with no sharp corners, which is good for high voltage applications and can be easily soldered for joints. It uses high-strength Hastelloy substrate for better mechanical properties and lower AC losses. SuperPower is able to deliver 2g HTs wire in 100 to 300 m typical length with high critical current of 100 A (standard) in 4 mm width tape. At 77 K, this wire can operate up to 1 T maximum field.

SuperPower 2G HTS wire has been successfully constructed and tested in various applications, such as transmission cable, Fault Current Limiter (FCL), high filed magnet, and coils. For example, Advanced Conductor LLC constructed a Conductor On Round Core (CORC) cable consisting of 20 tapes, wound into six layers, forming a cable with an outer diameter of 7 mm and then wound into a two layer, 12 turn magnet. The CORC cable magnet reached a winding current of 1950 A at 20 T. A record winding current of 4100 A at 19.81 T was demonstrated in 2012. Another example is a 30 m 2 G HTS cable constructed by Sumitomo Electric Industries and installed in National Grid systems in 2008 as part of the Albany HTS cable demonstration. AC losses of 0.36 W/kA-m were demonstrated.

In superconducting power cable, layers of HTS tapes, which transmit the power, are stranded around a metal of hollow former. The HTS tapes are surrounded by high voltage insulating material, commonly referred as dielectric. Furthermore, a cryostat insulates the whole cable core against ambient temperature. The HTS tapes are usually cooled with liquid nitrogen ($LN_2$) (77 K), which is pumped through the cable cryostat. Consequently, the dielectric is also immersed in $LN_2$. Therefore, this cable is generally called a cold dielectric cable. Such a cold dielectric cable may be of benefit to the aerospace example considered, as it allows conductor elements to see pressures higher than ambient.

In a HVDC cable design, the inner layers of HTS tapes transmit power while the outer layers are grounded. Induced current in outer layer will eliminate the electromagnetic fields of the inner layers. Therefore, the electromagnetic field is contained inside the superconducting screen. The cable inductance can be reduced significantly.

For medium voltage (up to 72 kV), concentric cable offers the most compact design with the best utilization of HTS tapes. All three phases and a screen, each separated through dielectric, are stranded around a hollow former. The former can be used as a return channel for $LN_2$. Concentric cables exhibit no external magnetic fields as well.

The design of superconducting HVDC cable is very similar to the design of superconducting HVAC cable. The inner HTC layers are separated through the dielectric from a screen consisting of copper wire only. With bipolar HVDC cable system, with voltage levels up to ±320 kV a transmission power of 4.5 GW and even more is easily attainable.

From nkt cables' HTS Triax energy cable systems datasheet, their three phase MVAC cable constructed with 1G BSCCO-type HTS tape can provide phase current up to 3.4 kA, and phase voltage up to 42 kV. The weight of the HTS cable core (three phases, thermal insulation not included) is ranging from 3.5 kg/m (1.25 kA phase current) to 8 kg/m (3.4 kA phase current).

In this study, each wing transmission line needs to carry power of 12.5 MW and current of 6.25/V kA, while V is the DC bus voltage (in kV) in the bipolar DC system. Lower voltage level will lead to higher current rating for superconducting cables. Therefore, DC bus voltage selection should also consider superconducting cable's current carry capability. At the same time, higher insulation requirement is associated with higher bus voltage. The impact of voltage on cables is more of a trade-off between cable rating and insulation requirement. Figure 6 illustrates the early study estimate that distribution cables only contributed around 5 percent of the whole system mass; however, when the cable insulation is considered in addition to the superconducting core, and if greater lengths are required due to limitations in bend radius, then cable mass will contribute to the optimum system voltage. The cable impact will favor

higher voltage within the considered range of approximately 1 to 10 kV. Section 6.6 covers the mass assumptions used for both the superconducting core and the transferline.

### 2.3.4 Power Conversion Consideration

As mentioned in Section 2.3.2, at cryogenic temperature the equivalent resistivity of both IGBT and MOSFET will be significantly reduced and IGBT will have a much lower resistivity compared with MOSFET. Thus, even considering the constant voltage drop across the IGBT, the total voltage drop of IGBT is still much less than that of MOSFET for a given silicon area at a high level current.

To keep high power density, IGBT is selected to build the cryogenic converter.

For a converter, the power rating can be estimated as

$$P_{sys} = NV_{dc}I \tag{7}$$

in which, $P_{sys}$ is the converter power rating, $V_{dc}$ is the single device blocking voltage, $N$ is the number of series connected devices in the converter to block the total DC bus voltage, and $I$ is the system current flowing through each device. $N$ is related to converter topology, e.g., $N$ is 1 for a 2 level converter and is 2 for 3 level converter topologies.

For an IGBT device, the conduction loss in the device can be expressed as

$$\begin{aligned} P_{loss\_cond} &= V_{ce}I \\ &= \left(V_0 + R_{ceon}I\right)I \approx V_0 I \end{aligned} \tag{8}$$

in which, $P_{loss\_cond}$ is the device conduction loss, $V_{ce}$ is the voltage drop of the IGBT when it is carrying current, $V_0$ is the constant voltage drop part and $R_{ceon}$ is the equivalent resistor of the IGBT. Since the constant voltage drop is dominant, $V_{ce}$ can be estimated close enough as $V_0$. Cryogenic test conducted at GE-GRC shows that with about six Si IGBT chips in parallel, the conduction loss on the equivalent resistor of the IGBT is about one tenth of the loss on the constant voltage drop. This supports the assumption of using the constant voltage drop to estimate the conduction loss. $V_0$ is determined by the silicon material and semiconductor manufacture process and does not change much with device voltage or current rating.

The converter loss mainly consists of two parts: device conduction loss and switching loss. If the percentage of device conduction in the overall converter loss is $k$, the converter efficiency can be expressed as

$$\begin{aligned} \eta &= 1 - \frac{P_{loss\_cond}}{kP_{loss}} \\ &= 1 - \frac{NV_0 I}{kNV_{dc}I} \\ &= 1 - \frac{V_0}{kV_{dc}} \end{aligned} \tag{9}$$

Because $k$ and $V_0$ are constants, higher $V_{dc}$ is desirable to achieve higher efficiency. In other words, IGBT with higher blocking capability can help increasing system efficiency.

For example, if the target converter system efficiency ($\eta$) is higher than 99.8 percent, the voltage drop across the single IGBT is $1V$, and conduction loss is 80 percent of the overall converter loss, then

$$\begin{aligned} \eta &\geq 99.8\% \\ \frac{V_0}{kV_{dc}} &\leq \frac{0.2\%}{2\times 2\times 2} \\ \frac{1V}{80\%V_{dc}} &\leq \frac{0.2\%}{2\times 2\times 2} \\ V_{dc} &\geq 5kV \end{aligned} \tag{10}$$

In this calculation, the first factor of 2 represents the two stages of power conversion: one on the generator side and on the propulsors side. The second factor of 2 represents the two converters in each stage: the DC/AC or AC/DC converter and the DC breaker for voltage source architecture or the BIU for ring architecture. The third factor of 2 represents the number of series connected device in each converter during the operation.

The calculation is only an example to show the idea. The exact number may change with different projected $V_0$ and $k$. The voltage threshold also depends on how technology evolves. If DC motor technology is mature enough to be used in 2035, for the ring architecture, the function of DC/AC and AC/DC converter can be integrated into the BIU, so the impact of the second factor of 2 can be eliminated. In addition, if bipolar IGBTs become available, the third factor of 2 can also be eliminated. Thus, to meet the same efficiency number, devices with lower blocking voltage can be used. Or in other words, the system efficiency can be improved with the same device.

For the voltage source architecture, the transmission line voltage can be equal to the single device blocking voltage ($V_{dc}$), if a simple two level converter is used. In this example case, it can be 5 kV. For the ring architecture, the transmission line voltage is $MV_{dc}$, M is the number of propulsors.

## 2.4 Conclusions

One voltage source architecture (Architecture 1) and one current source ring bus architecture (Architecture 2) are proposed and compared against the Baseline Architecture (Architecture 3 proposed in first study).

- Both architectures reduce system weight. Weight reduction in Architecture 1 (8.6 percent) is achieved by an advanced fault isolation scheme with the usage of high power density fast disconnects. Architecture 2 adopts a breaker-free architecture to reduce the system weight (by 3.6 percent).
- Architecture 1 uses redundant feeders to reduce the propulsor size, which makes it 210 kg (5 percent) lighter than Architecture 2. This power rerouting capability is hard to implement in Architecture 2.
- In Architecture 1 the whole system (including wing transmission, buses, and distribution feeders) operate at the same voltage level, while in Architecture 2 bus voltage is multiple times of feeder voltage. A higher insulation requirement is associated with Architecture 2.
- The need for a Bidirectional Interface Unit in Architecture 2 detracts from its weight benefit achieved by removing the need for DC circuit breakers.
- Based on the above reasons, Architecture 1 is selected for the following study. The development of new technologies, such as DC machines and bipolar semiconductor devices, will possibly change the selection and significantly reduce the system weight.

Given the initial range of 1 to 10 kV, DC bus voltage study incorporates grid architecture design, generator / motor voltage consideration, cryogenic electronics characteristics, superconducting cable characteristics and power converter voltage consideration.

- Machine weight mainly depends on its power rating and it is not sensitive to voltage rating (see Section 2.3.1.1).
- A 1 to 10 kV medium voltage range is very typical for conventional electric machines in the 1 to 10 MW range. Although insulation requirements will increase as the voltage increases, there is no evidence suggesting that the electric machine's coil construction or design will be limited by the assumed voltage range of this study.
- For cryogenic applications of high power, when massive paralleling is not considered, the semiconductor device of choice is the Si IGBT optimized for low temperature operations.
- Cryogenic device will be able to carry much more current than it can at room temperature and block less voltage (30 percent less) than it could at room temperature.
- The impact of voltage on cables is a trade-off between cable rating and insulation requirement. When only considering the superconducting core mass for cables, one may conclude that they would be only a secondary effect on the system weight; however, cable construction for cryogen and thermal insulation significantly add to the weight and will impact voltage level selection, as shown in later sections.
- Semiconductors with the maximum blocking voltage should be used to increase system efficiency. At cryogenic temperature, the equivalent resistor of IGBT device is negligible and the forward voltage drop demonstrates a constant value and dominates IGBT's conduction loss. To achieve a certain target converter efficiency level, a lower bound of DC voltage can be calculated. A calculation based on Architecture 1 and the best approximation of related coefficients indicates DC bus voltage should be greater than 5 kV to meet 99.8 percent converter efficiency requirement.

# 3.0 Mechanical Versus Solid-State Circuit Breakers

## 3.1 Comparison of Different Solutions

DC circuit breakers add system weight in the TeDP Electrical System. The first phase study shows that approximately 30 percent of the entire electrical system weight is from DC circuit breakers (Ref. 1). The voltage source architecture proposed above uses lighter fast disconnects to replace many of the DC circuit breakers, which significantly reduce the weight of DC circuit breakers to 10 percent of the system weight. In this task, we review and compare different types of DC circuit breakers and propose a solution for high-efficiency and high power density DC breakers.

The three promising approaches we consider in this study include:

1. Conventional DC breakers used at ambient temperature
2. Cryogenic Solid-State Circuit Breaker
3. Cryogenic Hybrid Circuit Breaker

The steady-state rating of the DC breakers in this study is considered to be 1 kA continuous in a 10 kV circuit.

### 3.1.1 Mechanical Circuit Breaker

Cryogenic DC circuit breaker technology has not been developed. For electromechanical DC circuit breakers, the cryogenic temperatures would cause the material to become brittle and fragile (Ref. 1). Therefore, conventional DC breakers have to be used at ambient temperature in the TeDP application, and connections are needed through the cryostat wall.

Conventional DC breakers have been nominally designed for approximately 4 kA and up to several kilovolts (Ref. 27). They are able to break up to 50 kA of fault current (Refs. 27 and 28). The power density is in the neighborhood of 100 kW/kg, with contact resistance in the range of 10 to 100 μΩ (Ref. 29). The advantage of using conventional DC breakers is that it is a well-known technology, with a proven track-record. So, it is low risk. However, the large size and high response time (up to 10 to 100 msec) makes it not suitable for architecture we proposed in the selected Architecture 1. Meanwhile, it can only be used at ambient temperature. The need for connections through the cryostat wall increases system complexity.

### 3.1.2 Solid-State Circuit Breaker

Compared with mechanical circuit breaker, Solid-State Circuit-Breakers (SSCB) have been proposed for the grid applications (Ref. 30). Solid-state circuit breakers based on high power semiconductors potentially offer enormous advantages when compared to the conventional mechanical solutions, since solid-state breaker is able to switch in a few microseconds. Hence, the maximum current will never be far away from the rated current and the whole process will just last for around a few hundreds of microseconds. Meanwhile, advanced semiconductor packaging techniques can enable adequate cooling performance. However, compared with mechanical breaker, higher on resistance of the semiconductor switch also creates high conduction loss. Based on the previous analysis and summary of cryogenic semiconductors in this report, the silicon IGBT is preferred in a high power cryogenic application. With the cryogenic technology, the on resistance of the semiconductor can be greatly reduced. Nevertheless, the forward voltage drop of the silicon IGBT generates high loss for conducting the main current, which is still a concern in the TeDP system because of the high efficiency target. Therefore, a hybrid solution that combined both mechanical and solid-state technologies is desired for the DC protection in the aviation system.

### 3.1.3 Hybrid DC Circuit Breaker

Literature (Ref. 31) describes a hybrid HVDC breaker. During normal operation, the current only flows through the lower-impedance bypass, which consists a fast mechanical disconnect in series with a semiconductor-based load commutation switch. When a fault occurs, the load commutation switch immediately commutates the current to the main HVDC breaker, which is separated into several sections with individual arrester banks and the fast disconnect opens (Ref. 31).

The recent advances in cryogenic contactors (Ref. 32) suggest that the eventual development of cryogenic hybrid DC breakers is likely, because a cryogenic contactor can be used to construct the cryogenic hybrid breaker shown in Figure 17.

The breaker is comprised of a cryogenic contactor in parallel with an electronic snubber. During normal operation, the main current only goes through the cryogenic contactor, which leads to very small conduction loss. The parallel semiconductor only conducts the current during transient process. Because DC voltage level in the TeDP electrical system is up to 10 kV, probably only two switching sections are needed in the snubber path considering single device's capability around 5 kV. Then the voltage across the contactor will be around 2 V (around 0.7 V forward voltage drop for single silicon IGBT device). Detailed analysis shows that the contactor itself can open to force commutation without generating arc or damaging itself. Therefore, the load commutation switch in series with the contactor can be removed to further reduce the conduction loss. The detailed analysis of this cryogenic hybrid DC breaker will be shown in the next section.

Based on the preliminary comparison, the characteristics of the three DC protection candidates are summarized in Table 6. With the consideration of fast response, higher efficiency, compact size, and lighter weight, the hybrid circuit breaker combined with cryogenic technology is selected as the DC protection system for the TeDP electrical system.

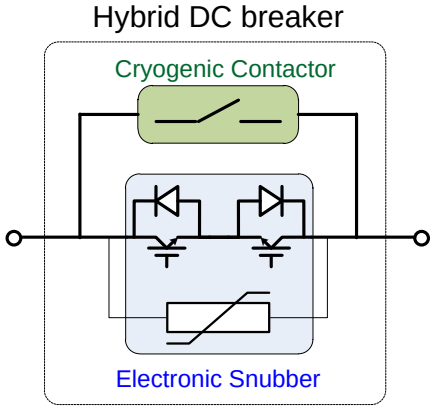


Figure 17.—Cryogenic Hybrid DC Breaker

TABLE 6.—COMPARISON OF CANDIDATE DC CIRCUIT BREAKER SOLUTIONS

| | Response time | Fault current | Arcing | Size and weight | Efficiency |
|---|---|---|---|---|---|
| Mechanical circuit breaker | 10 to 100 ms | High, poorly controlled | Yes | Large (100 kW/kg) | High |
| Solid-state circuit breaker | 10 to 100 μs | Controlled | Minimal | Medium (200 kW/kg) | Low |
| Hybrid circuit breaker | 100 μs to 1 ms | Slightly higher than fault current | Minimal | Medium (175 kW/kg) | High |

## 3.2 Operation and Analysis of Proposed Hybrid Circuit Breaker

Operation during a fault is as follows: When the fault is detected by whatever protection / control logic is employed by the power system architecture, the electronic snubber is placed in the conducting state and the cryogenic contactor is opened. When the contacts part, the current will commutate into the snubber. Commutation will be detected by a rise in voltage across the snubber, due to the conduction of the snubber electronics. At that point, the snubber will be turned off, and the voltage across it will rise in response to the inductive energy stored in the rest of the network. The snubber will incorporate zinc oxide (ZnO) voltage suppressors to clamp the voltage and to absorb inductive energy trapped in the network.

After the fault is cleared, the breaker is reset as follows: The snubber is switched to the conducting state, and then the contactor is closed.

There are several parameters to be considered in this application:

1. Steady-state current of 1 kA and open circuit voltage of 10 kV.
2. Contact resistance. On the order of 1 μΩ is projected for a cryogenic contactor, resulting in steady-state losses of 1 W per breaker.
3. Contactor operation time. Using a repulsion coil, on the order of 100 μsec should be possible.
4. Interruption current. During a fault, the current through the DC breaker will rise. The rate of rise can be limited by including a superconducting inductor in the circuit.
5. Snubber conduction voltage. It is projected that this will be on the order of 2 V for electronic devices capable of conducting 1 kA for 100 μsec, and capable of withstanding 10 kV stead-state, and pulse voltages of 16 kV for a few milliseconds.
6. Contactor-snubber loop inductance. On the order of a 100 nH is expected.

These parameters are related as follows. When the contactor contacts part, the current that they were carrying will commutate into the electronic snubber. This will create a brief pulse of voltage across the contacts. Details of the voltage waveform depend on stray capacitance, loop inductance, and the effective resistance of the snubber. As the contacts part, their resistance will go from 1 μΩ to infinity over a very short time period, typically 10 to 100 nsec. During this time, the voltage will rise from 1 mV, to several volts, then back down to the steady-state voltage of the snubber, on the order of 2 V. It can be shown that the amount of energy dissipated in the contacts during the commutation process is approximately equal to the energy stored in the loop inductance. We expect that the current during the commutation process with be on the order of 2 kA, so with a 100 nH loop inductance, we expect to dissipate 0.2 J in the contacts. With this small value we do not expect any damage to the contacts.

It is projected that the ratings of cryogenic contactors could easily reach 50 kA. None-the-less, we would like to minimize the amount of current flowing through the contacts at the moment of interruption, in order to minimize the voltage spike when the contacts part, and to minimize the amount of energy dissipated in the contacts. To that end, we propose including a superconducting inductor in the circuit to limit the rate of rise of current during the fault. An inductance of around 1 mH is suggested. That will limit the rate of rise of current to 10 A/μsec during a fault, so the current through the contacts will be around 2 kA when the contacts part 100 msec after fault initiation. Of course, the ZnO voltage clamp in the electronic snubber will have to be sized to absorb this energy, approximately 2000 J, and the cryostat will have to absorb this amount of heat. It is not expected that this will happen very often. In the case of a single temporary fault, this will happen only once. In the case of a permanent fault, the amount of energy will depend on the number of reclose attempts.

Based on recent data, it is now assumed that a 5 kA, 10 kV superconducting contactor will be available by 2025, since superconducting contacts are already available in that current range. High temperature superconducting disconnects are presently available with current rating in the 1000s of ampere range, and the literature recently reports resistance in the 1 μΩ range (Ref. 32). The most

promising technique at this date is YBCO with a thin silver plating. Contact resistance on the order of 1 μΩ has already been reported, with contact force in the range of 10 to 500 N, which is well within range of the electromechanical techniques used in conventional power contactors.

Note that "superconducting" is a misnomer for the expected contactor, since the resistance is not zero. However, it is low enough so that the power losses (0.36 W per contactor at 600 A) are acceptable.

It is expected that the design of the superconducting contactor will resemble that of a conventional contactor, except its actuation coil will be superconducting, and its contacts will have very low resistance. Size and weight of the superconducting contactor will be comparable to that of a conventional contactor.

The actuation coil is expected to have zero steady-state losses. It may or may not have small energy losses during opening and closing, but it is not expected that the contactors will be called upon to operate very often, so that does not really matter.

Another consideration for this application is contact life (number of switching operations). At present there is not much information on how many times superconducting contacts may be operated before requiring replacement. The work of Reference 32 indicates that physical degradation of the contacts may be an issue. That said, the technology is still in its infancy, so it is quite likely that by 2025 it will advance to achieve contact lifetime comparable to that of conventional contacts. Also, in this application, it is not expected that there will be any contact erosion due to arcing, since the contacts will be opened only when there is no current through them, and will be closed only when the voltage across them is small.

Opening speed is also of interest in this application. In conventional contactors, the usual design employs a spring to open the contactor, and an electromagnet to close it. It is possible to increase the opening speed by using a spring to close, and an electromagnet to open. In any case, it is expected that opening time of around 1 millisecond is possible.

If it is required to open much faster than that, it is possible to use a repulsion disc principle. Because the repulsion disc would be superconducting, extremely high forces could be developed, so it would be possible to achieve opening times on the order of 100 μsec.

# 4.0 Design, Operation, and Weights of Hybrid Breakers and Disconnects in a TeDP Electric Grid

This section provides details for the design and operation of cryogenic hybrid breakers and disconnects for fault isolation and grid reconfiguration in a turboelectric distributed propulsion electric grid, using the grid architecture shown in Figure 18.

A viable fault isolation and grid reconfiguration strategy can be based on cryogenic hybrid breakers and disconnects with the following features:

- Low steady-state losses
- Rapid fault isolation and grid reconfiguration
- Supports optional reclosing attempts after a fault

During a fault, hybrid breakers provide fault clearing and disconnects provide galvanic isolation and / or grid reconfiguration. The strategy can be illustrated with a few fault scenarios.

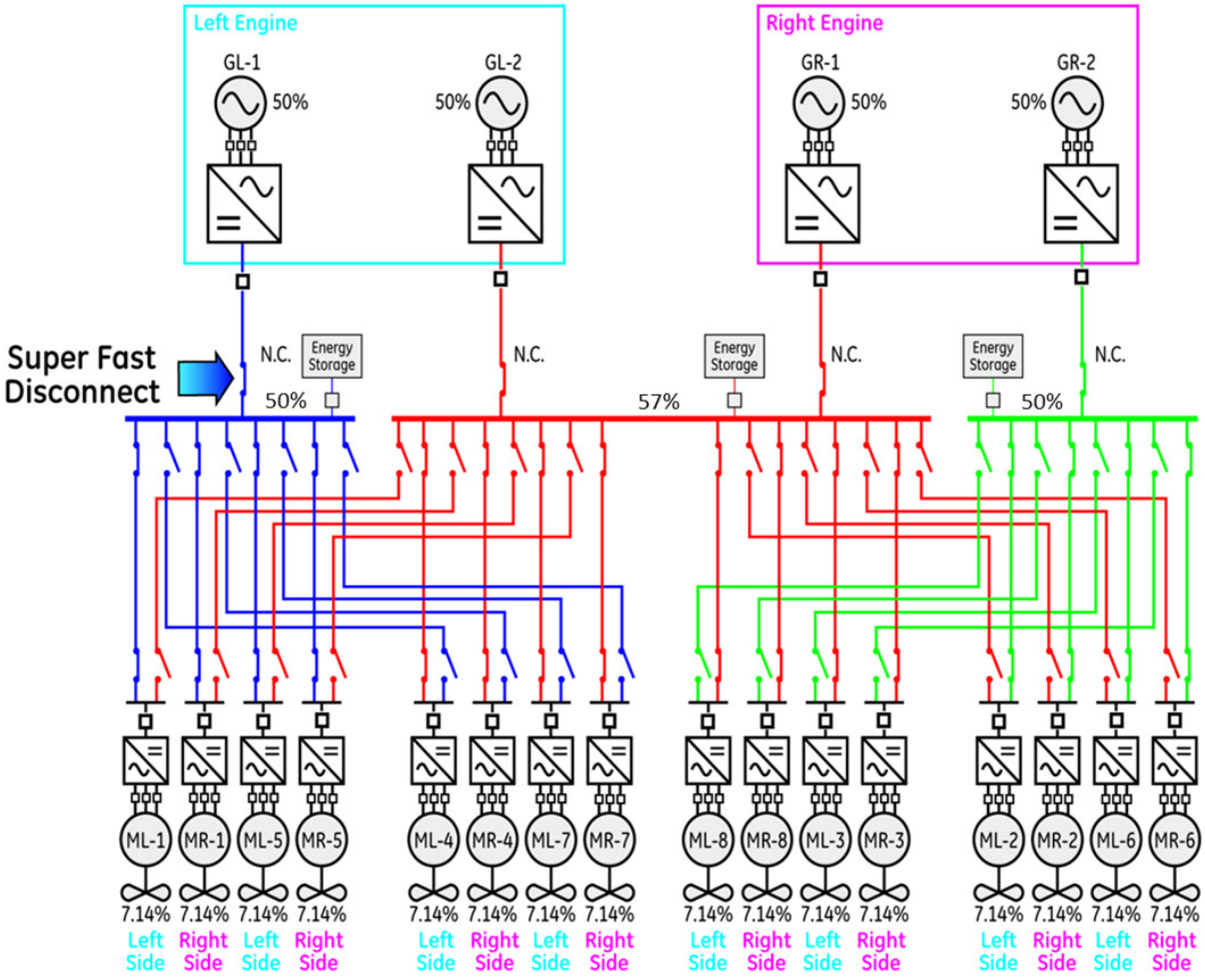


Figure 18.—Three-Bus Multi-Feeder Architecture with Integrated FCL, Power Conversion, and Circuit Breaker Function

The first scenario is a flash-over on one of the feeders, such as on the blue feeder to motor ML-1. In this scenario, depending on the details of what triggered the flash-over, it might be possible to clear the fault and completely restore the grid simply by tripping and reclosing the DC breaker that supplies power from generator GL-1 as well as the DC breaker feeding power to the motor ML-1. The scenario proceeds as follows:

1. There is a flashover on the blue feeder to ML-1.
2. DC breakers for GL-1 and ML-1 clear the fault in about 300 μsec. This time includes 100 μsec to get the contacts in the breakers open to full gap and begin the interruption process, and 200 μsec to drive the fault current to approximately zero.
3. After the fault current reaches approximately zero, there will be a small amount of leakage current, because in the proposed design the breakers do not provide galvanic isolation. In the proposed design, the leakage current will have both a DC component and an AC component. The DC leakage will be about 2 mA, and is due to the DC leakage through the DC breaker driven by the 10 kV DC voltage across the breaker. The AC leakage will be about 20 mA, driven by ripple voltage across a capacitor in the breaker included specifically to generate a capacitive current of about 20 mA. This creates ideal conditions to clear the fault arc. Because the AC component of current is greater than the DC component, there will be current zeros. Because most of the current is capacitive, the fault arc will experience "soft switching" in which voltage builds up relatively slowly after current zero.
4. If the fault clears, it is possible to quickly and completely restore the grid by reclosing the two breakers. It is a good idea to reclose the breakers in two stages. During the first stage, the electronics in the breakers are turned to the conducting state, but their contacts are not closed. This enables a very fast "trip-free" re-opening of the breakers if the fault persists. In this scenario, it is assumed that the fault is cleared, so the breaker controls proceed to the second stage in which the contacts are closed.
5. The second scenario is one in which there is a persistent fault. In that case the scenario starts with steps 1 to 3 of the first scenario, but in step 4, the reclose operation results in a trip-free operation in which the electronics turn off, and the fault current is interrupted. At that point the DC disconnects at either end of the feeder will open to provide galvanic isolation of the fault. Details of the interruption of the DC and AC leakage currents will be included in the discussion of the details of the operation of the DC disconnects (see Section 4.3).

Another option is to forego the reclose attempt. That is a system control design decision that it might be best to defer until actual fault testing can be done. The decision will depend on the probabilities of clearing various types of faults.

In the case of a permanent fault, after the fault is removed, the next step is to attempt to restore power to motor ML-1. That is done by simply closing the disconnects for the alternate (red) feeder to ML-1, with the breaker for ML-1 open to block in-rush current into the electronics for ML-1. There is a remote possibility that there is a fault on that feeder, in which case the disconnects will be damaged. In that case, breakers will be tripped and reclosed to clear the fault, and ML-1 will be permanently out of service.

Assuming that the disconnects are successfully closed, the next step is to close the breaker for ML-1. If that is successful, ML-1 is in service. If not, the prudent thing to do would be to trip the ML-1 breaker, and take it out of service.

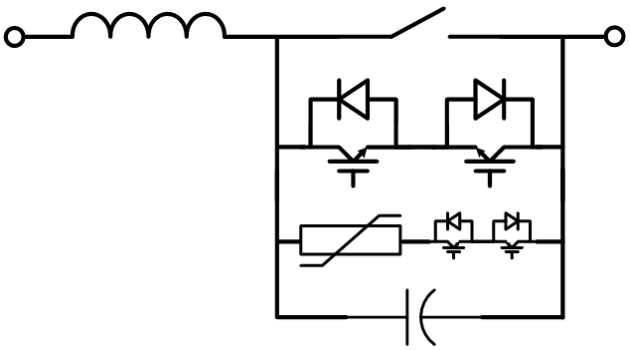

Figure 19.—Proposed Hybrid DC Breaker

## 4.1 Hybrid DC Breaker

The proposed hybrid DC breaker is shown in Figure 19. Its major components consist of:

- Series inductor, L, which is used to control the rate of rise of fault current, thereby managing the amount of current that is flowing when the breaker interrupts the fault, and the amount of energy that must be dissipated.
- Cryogenic electromechanical switch to carry load current and momentary fault current. Soft switching is achieved by arranging for the primary electronic snubber to be conducting when the switch is opened or closed.
- Primary electronic snubber to limit the amount of voltage across the mechanical switch when it opens or closes.
- Zinc-oxide surge suppressor, which provides several functions, including:
  - Driving the fault current to zero in the least amount of time after the electromechanical switch opens.
  - Limiting the peak transient voltages on the system during fault interruption.
  - Quickly damping post-fault clearing transients to improve the conditions for arc extinction in the case of a flash-over.
- Secondary electronic snubber in series with the ZnO surge suppressor, to limit the amount of DC leakage current passed by the breaker.
- Shunt capacitor. A small amount of capacitance is connected in parallel with the breaker to contribute a small amount of capacitive current to the fault. This will improve the conditions for extinction of a flash-over arc.

Operations of the DC breaker include fault interruption, reclosing, and resetting.

Fault interruption proceeds as follows:

First, the fault is detected quickly. Conventional fault detection techniques, including differential techniques, can be used to detect the fault in a few tens of microseconds after the fault current exceeds maximum normal operating values. Both the primary and secondary electronic snubbers will already be turned on; they can be left on continually during normal operation conditions. As soon as the fault is detected, opening of the electromechanical contacts is initiated. Contacts will part almost immediately, but it will take around 100 μsec to achieve full contact gap and full voltage withstand capability of 20 kV.

Actually, contact parting is a process that takes on the order of 10 to 100 nanoseconds, rather than an instantaneous event. During the process, the contact pressure drops from normal design pressure to zero, and the contact resistance rises from approximately 1 μΩ to infinity. This creates a brief voltage pulse to appear across the contacts that commutates the fault current into primary electronic snubber. As a result

of the commutation process, some energy will be dissipated in the contacts. It can be shown that the amount of energy dissipated is approximately equal to one half of the square of the fault current times the inductance of the commutation loop, typically on the order of 100 nH. Contact parting will take place almost as soon as the fault takes place, so the current will still be around 1000 A, and the energy dissipated by the contacts will be around 0.05 J, which is really a miniscule amount, and should not cause any arcing or damage to the contacts.

Current will quickly commutate into the primary electronic snubber as the contacts part. However, at that point it is still too soon to switch the primary electronic snubber into a non-conducting state. That is because it will take a certain amount of time for the contacts to achieve full voltage withstand. Based on experience with repulsion coil actuation, we believe full contact gap can be achieved in approximately 100 μsec.

Therefore, the controls will deliberately delay 100 μsec after the electromechanical switch starts to open before placing the primary electronic snubber in the non-conducting state. Assuming that the value of the series inductance is equal to the optimal design value of 1 mH, at that time the fault current will have risen from 1000 to 2000 A.

When the primary electronic snubber is placed in the non-conduction state, fault current diverts into the shunt snubber capacitor, causing it to rapidly charge to the clamping voltage of the ZnO surge suppressor. In order to quickly drive the fault current to zero without creating excessive transient voltages, we suggest setting the clamping voltage at 20 kV in a 10 kV system. This will drive the fault current to zero in 200 μsec after the electronic snubber goes into the non-conducting state, for a total time of 300 μsec to interrupt the fault. At this point in the process the secondary electronic snubber is still conducting, so there will be significant (on the order of 2 A) leakage current. In order to drive the leakage current still lower, at this point the secondary electronic snubber is placed in the non-conduction state, limiting the DC leakage current to a value on the order of 2 mA. By selecting a value of capacitance for the shunt snubber capacitor to pass around 20 mA of AC capacitive current, ideal conditions are created for the extinction of a flash-over.

The hybrid DC breaker affords the grid designer the option of attempting a fast reclose if the fault is cleared. This can be achieved very quickly by simply placing the primary electronic snubber back into the conducting state, without reclosing the electromechanical contacts. This enables a reclose without incurring a delay for electromechanical reset. If the reclose is successful, the controls can then execute a reset operation. If not, the controls can execute a “trip-free” operation by proceeding through the fault interruption steps without having to open the electromechanical contacts, since they will already be open. During the time between reclose and reset, there will be a voltage drop across the breaker on the order of 1 or 2 V, resulting in a power dissipation of 1 or 2 kW. Therefore, the time delay between reclose and reset should be kept as short as possible.

Generally speaking, it is difficult to achieve both fast opening and fast closing of electromechanical switches. So, with a 100 μsec opening time, a closing time on the order of 1 msec is a reasonable target. That will result in a total energy dissipation during the delay to reset of 2 J, which is a reasonable number.

The reset operation itself is trivial. Simply close the electromechanical switch with the primary electronic snubber in the conducting state. This will assure that the voltage across the contacts is less than about 2 V during contact closing.

We next turn our attention to remaining design questions, starting with the optimal value for the series inductor.

The function of the series inductor is to limit the peak fault current and the total amount of energy that the ZnO must dissipate. If the value of inductance is too high, the energy due to the initial current dominates. If the value of inductance is too low, the energy due to rapidly rising fault current is too high. There is a value of inductance that minimizes the amount of energy, given by the following equation

$$
\begin{aligned}
&L = \frac{V_0 \cdot \Delta t_1}{I_0} = 1\,\text{mH} \\
&V_0 = \text{normal operating voltage} = 10\,\text{kV} \\
&\Delta t_1 = \text{time delay to open contacts} = 100\,\mu\text{sec} \\
&I_0 = \text{value of load current prior to fault} = 1000\,\text{A}
\end{aligned}
\tag{11}
$$

Interestingly enough, with the optimal sized series inductor, the peak fault current is equal to 2 times the initial load current.

Also, it can be shown that the total energy dissipated in the ZnO during the fault interruption process is given by

$$
\begin{aligned}
&E = 2 \cdot \frac{V_{MAX}}{V_{MAX} - V_0} \cdot V_0 \cdot I_0 \cdot \Delta t_1 \\
&E = \text{energy dissipated in the ZnO} \\
&V_{MAX} = \text{ZnO clamping voltage}
\end{aligned}
\tag{12}
$$

For the values of design parameters being considered (10 kV system, 1000 A load current, 100 μsec opening time) and a clamping voltage of 20 kV, the amount of energy dissipated in the ZnO suppressor is 4000 J.

Equations (11) and (12) are based on the approximations that the equivalent circuit model of the generators and electronics is an ideal DC voltage source. In reality, the model is more complex than that. For example, a more detailed model will typically include inductance that will help limit the rate of change of fault current. The more complex model will not substantially change the details of the operation of the breaker. However, it will reduce the value of inductance needed to limit the rate of rise of current and will reduce the amount of energy dissipated in the ZnO suppressors. When it is time to actually design and build the grid, it is recommended to perform simulations with detailed models to determine the actual values of the hybrid DC breaker circuit parameters.

Also, Equations (11) and (12) were developed for the generator DC breakers. For the motor DC breakers, the amount of inductance needed and the amount of energy dissipated in the ZnO suppressors will be considerably less than the generator DC breakers. Again, it is recommended to perform simulations to determine the actual values needed for the motor breakers.

We have considered alternate methods to the use of the ZnO suppressor to control transient voltages during fault interruption, including a shunt snubber capacitor, and have found that the ZnO is the best method, for a variety of reasons, including:

- For a given value of peak transient voltage, the ZnO suppressor reduces the fault current to zero in less time than any other method. That is because the voltage across the breaker is approximately equal to the peak value during the entire time interval during which the fault current is going to zero.
- With the use of a ZnO suppressor, residual voltage and current transients are very small immediately following the first current zero. This facilitates clearing of flash-over arcing. This is in contrast with a capacitive snubber, for example, which produces substantial voltage and current transients after the first current zero.
- With the use of a ZnO suppressor, there is very little electrical energy involved in a reclose-reset operation. This is in contrast with the use of a shunt snubber capacitor, which will contain a substantial amount of energy that must be dissipated in a reclose-reset operation.

We note that in addition to the intentional DC component of the voltage in the grid, there will be a ripple component as well, on the order of 500 V at 1000 Hz. This can actually be used to advantage to enhance arc extinction in the case of a temporary flash over. There are two reasons for this. If the amount of ripple current through the breaker is larger than the DC leakage current, there will be real current zeros, which will give the arc a good chance of extinguishing. Also, of the three general types of circuit impedance (inductive, resistive, capacitive), capacitive impedance provides "soft-switching" interruption, because the instantaneous value of the voltage across the arc immediately after current zero is zero. This provides both zero current and zero voltage conditions at the moment of interruption. In order to take advantage of this effect, the shunt capacitor should be sized to pass a ripple current of approximately 10 times the DC leakage current of the breaker. So, for example, with a DC leakage current of 2 mA, a ripple current of 20 mA would be reasonable. With 500 V ripple voltage at 1000 Hz, this would require a capacitance of about 13 nF, which is quite reasonable.

We also note that the secondary electronic snubber does not need to be rated for full system voltage, because of the extreme non-linearity of the ZnO suppressor that it is in series with. For example, through careful design, it should be possible to achieve approximately even voltage division between the two elements. In order for that to happen, the secondary electronic snubber should not be turned off until the voltage across the breaker drops down from 20 to 10 kV.

Finally, we note that measurements of the behavior of metal-oxide varistors have been made at $LN_2$ temperatures (Ref. 33), and no issues have been identified. In fact, performance improves at low temperatures, because one of the main considerations in applying metal-oxide varistors is the increase in leakage current as temperature rises.

## 4.2 Loss, Size, and Weight

We now turn our attention to steady-state loss, size, and weight of the hybrid DC breaker. Major components include an inductor, cryogenic electromechanical switch, primary electronic snubber, secondary electronic snubber, snubber capacitor, and ZnO suppressor.

### 4.2.1 Weight and Size Estimation for the Series Inductor

The inductor design is sized to limit the rise of a fault current as described in Equation (11). To avoid saturation, an air core inductor is typical. A solenoid shape was selected and dimensions were estimated based on YBCO tape. The inductance calculation used the approximation below:

$$L \approx N^2 \mu \frac{d^2 \pi}{4l} \cdot \frac{1}{1 + 0.45\frac{d}{l}} \tag{13}$$

where $L$ is inductance in Henry, $N$ is the number of turns, $\mu$ is permeability of air, $d$ is the coil diameter, and $l$ is the length of the cylindrical coil. The YBCO current was designed to be 70 percent of critical current for the estimated parallel field and coolant temperature. This resulted in an inductor with approximate length of 13 cm and a diameter of approximately 17 cm. The weight of the conductor and supporting ring was estimated as 6.5 kg.

### 4.2.2 Cryogenic Electromechanical Switch

The actual contacts in a cryogenic electromechanical switch are a small portion of the total size and weight. Most of the size and weight is due to the mechanisms used to achieve high speed operation. The design value of the opening time of the cryogenic electromechanical switch of 100 μsec pushes the limits of electromechanical technology.

A very good candidate for high speed operation is repulsion coil technology in which a pulse of current applied to a pancake coil quickly develops a large force in a copper disk via induced current. This

approach was used to advantage in a prototype HVDC breaker developed under contract to the U.S. Department of Energy in 1978 (Ref. 34). The repulsion disk was used to achieve high speed operation of a large valve with an approximate mass of 0.5 kg against a seating force of approximately 2000 N, with the valve starting to move in a few microseconds, and significant flow area in 100 μsec. Magnetic repulsion was used to high speed opening. A simple spring was used for closing. Tests showed that extremely high velocity could easily be imparted to the valve poppet nearly instantaneously. Application requirements for the repulsion coil in the HVDC breaker are approximately the same as for the cryogenic electromechanical switch, so we expect the size and weight to be approximately the same. Furthermore, the physics of the operation of a repulsion coil indicate that its ability to generate large forces improves as the temperature is lowered, so we would expect significant improvement in performance at $LN_2$ temperature.

The three largest components of the repulsion coil system were the repulsion coil, the copper disk, and the pulse electronics. The electronics were modest in size in 1978; if they were replicated now, they would be much smaller, and projection to the time of RTAPS deployment suggests they will be small enough to be overshadowed by the coil and disk, which constituted a can shaped cylinder approximately 8 cm high and 8 cm in diameter, and which weighed approximately 3 kg.

Regarding losses for the repulsion coil system, the only continuous losses are in the charging circuit for the pulse generating capacitor, and can be managed to practically vanishing values by using a low leakage capacitor.

### 4.2.3 Primary and Secondary Electronic Snubbers

#### 4.2.3.1 Requirements

Requirements were explained in the previous sections. It is assumed that the grid can be designed so that the electronic snubbers are unidirectional. If that is not that case, then we will have to double up, and use two sets of snubbers to handle the bidirectional case.

Due to the fact that snubber 1 in the breaker needs to conduct a peak current of 2 kA, exhibit a voltage drop of less than approximately 3 V at 1 kA, and be able to block 20 kV, makes it the more difficult to design than snubber 2.

#### 4.2.3.2 State-of-the-Art

Currently available IGBT silicon devices have a maximum blocking voltage capability around 6.5 kV and a peak current capability of about 1.5 kA, and exhibit a voltage drop of about 3.5 to 4.5 V at 1 kA at room temperature. This makes them not a good option for this application. Example parts include Mitsubishi/Powerex CM750HG-130R and Infineon FZ750R65KE3.

Cryocooling these existing devices will de-rate the maximum blocking voltage to about 70 percent of the room temperature capability and also decrease the conduction voltage drop. In order to block 20 kV, 5 IGBT in series will be required, which will require a voltage drop per device equal to 0.6 V at 1000 A in order to meet the specifications. Given the published data on these two switches, cryocooling will decrease the voltage drop per device from about 3.5 to 4.5 V at 1 kA at room temperature to about 1.5 to 2.5 V at 1 kA at cryogenic temperature. This is not adequate to meet the 0.6 V required.

Thyristor technology, on the other hand, if cryocooled, can provide the desired performance in terms of blocking voltage capability and forward voltage drop at 1 kA. State-of-the-art thyristors can block voltages as high as 8 kV and conduct currents as high as 2.3 kA (Infineon T2563 NH and T600N).

If cryocooled, their voltage blocking capability can still be considered to be about 70 percent of the rated voltage, making it capable of withstanding 5.6 kV. Therefore, only four devices will be needed. Three volts distributed over four devices connected in series translates to a 0.75 V drop per device at 1 kA when cryocooled. Given the performance of the parts at room temperature (drop of 2.75 V at 5 kA), the required performance of 0.75 V cryocooled becomes very feasible. Unfortunately the thyristor cannot be easily turned off, which is a must for this application.

#### 4.2.3.3 Future Developments

It is clear that high level of doping, and a proper doping profile, lead to a part with large voltage withstanding capability as well as very low conduction voltage drop. This has been demonstrated for the thyristor already. Very large levels of doping have been avoided for IGBTs structure due to fact that it will lead to slow turn-off transitions. However, for this application, turn-off requirements are not that demanding. Typical IGBT turn off times are on the order of 0.1 μsec, while all that is needed for this application is turn-off less than about 20 μsec, so there is plenty of margin. Furthermore, cryocooling will increase the turn-off speed and decrease the conduction voltage drop making it possible to extrapolate that, in the near future, for cryogenic applications, an IGBT with such doping concentrations and doping profile will exist and will be comparable in size to an existing thyristor.

#### 4.2.3.4 Weight and Size Estimation for Electronic Snubber 1 (20 kV, 3 V at 1 kA, max 2 kA)

Using the thyristor size and mass we can extrapolate that a stack of four devices will be a cylinder about 200 mm long, and have a diameter of 175 mm approximately, and an estimated weight of about 16 kg.

#### 4.2.3.5 Weight and Size Estimation for Electronic Snubber 2 (5 kV, max 2 kA)

This snubber will require only one element; therefore, we can extrapolate that a single device will be a cylinder about 50 mm long, and have a diameter of 175 mm approximately, and an estimated weight of about 4 kg.

### 4.2.4 Weight and Size Estimation for Snubber Capacitor

The value of the snubber capacitor will be on the order of 10s of nanofarads, which is quite small, even with a 10 kV DC and 20 kV peak rating. Order of magnitude size and weight is less than that of a hockey puck.

### 4.2.5 Weight and Size Estimation for Zinc-Oxide Suppressor

Since the ZnO suppressor will be operating in a contamination-free environment, we assume that it can be comprised primarily of ZnO material, without the need for the ceramic insulators that are included in the design of station surge arrestors for protecting the ZnO from contamination.

The key design parameters for the ZnO suppressor are peak electric field, peak current density, and total energy dissipated. From Reference 33 we conclude that there will not be any issues with operation at $LN_2$ temperatures. From Figure 3 of Reference 35, we can see that it is possible for a ZnO suppressor to support an electric field of 2000 V/cm, and a current density of 10 A/(cm*cm). We will come back to energy dissipation later.

For a nominal load rating of 1000 A and 10,000 V, and switch opening time of 100 μsec, the previous analysis indicates a peak voltage across the ZnO of 20,000 V, and a peak current of 2,000 A. If we combine these values with the supported electric field and current density, we find the required length is 10 cm, and the required area is 200 $cm^2$, for a total volume of 2000 $cm^3$. The density of ZnO is approximately 5.6 grams/$cm^3$. So, based on peak current and voltage considerations, the weight of the ZnO is 11.2 kg.

We now go back and check the energy dissipation. The analysis in the previous sections indicates that there will be about 4000 J dissipated in the ZnO when the DC breaker operates. This comes out to be 2 J/$cm^3$, which is very low for ZnO. To put that in perspective, typical energy dissipation capabilities of station arrestors are on the order of 2.6 kJ/kV, or 26,000 J at 10 kV. So there is plenty of margin with respect to energy dissipation; in this application all that we need to worry about is peak electric field and peak current density.

#### 4.2.5.1 Hybrid DC Breaker Preliminary Sizing Model

Table 7 provides the basis for a sizing scalar. Major component masses were estimated for a design point, which then allows calculation of a kilowatts/kilograms scalar of 187 kW/kg if no packaging or containment is considered. As will be described in later sections, if high pressure cryogen is assumed, this significantly reduced the power density to ~140 kW/kg, as shown in the table. The containment mass of 18.5 kg assumes an aluminum capsule designed for 650 psi cryogen.

The loss model assumes that the experimental values of ~1 μΩ can be achieved at current levels, which would span the range of the study voltages.

## 4.3 DC Disconnect

The circuit for the DC disconnect is shown in Figure 20. It has a relatively simple design because the electrical behavior of the DC breaker creates nearly ideal soft-switching conditions for the opening of the disconnects. The residual current through the breaker has a DC component of about 2 mA, and an AC component of about 20 mA through the breaker's shunt snubber capacitor. The disconnect consists of three elements: a cryogenic contactor, a snubber capacitor, and a snubber resistor. The contactor offers low resistance (approximately 1 μΩ) carrying of normal load current. The snubber capacitor assists interruption of residual DC current, and the snubber resistor prevents a spike of current through the contactor when it closes. The two functions of the DC disconnect are to open to isolate a fault and to close to reconfigure the grid subsequent to fault isolation.

TABLE 7.—POINT DESIGN SUMMARY

| Design Point Sizing | |
|---|---|
| Rated Current | 1,000 A |
| Rated Voltage | 10,000 V |
| Power | 10,000 kW |
| **Major Components** | |
| Electronics snubbers | 20 kg |
| ZnO | 10 kg |
| Switch | 3 kg |
| Inductor (below) | 11.42 kg |
| Subtotal | 44.42 kg |
| Bracket and wiring adder | 20% |
| Bracket and wiring adder | 8.88 kg |
| Minimum Component Volume | 0.012 $m^3$ |
| Containment Volume | 0.042 $m^3$ |
| Containment mass | 18.53 kg |
| Total Mass | 71.84 |

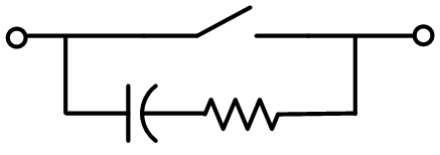

Figure 20.—DC Disconnect

In the case of a permanent fault, the DC breaker reduces the current from fault levels of thousands of A to DC and AC leakage currents of around 2 and 20 mA, respectively. If it is determined that the fault has not cleared, the appropriate DC disconnects are opened to complete the isolation process. They simply open. The leakage current will quickly commutate into the RC snubber. The amount of energy dissipated by the contacts during the very brief time interval that the contact resistance rises to infinity is determined mainly by the stray inductance of the commutation loop. An order of magnitude computation based on 100 nH and 20 mA indicates the amount of energy dissipated is on the order of 20 pJ, which is miniscule. So, the opening duty is very mild. The general shape of the switching waveforms is shown in Figure 21. At the time of contact opening, the current through the disconnect has been reduced to 2 mA DC resistive leakage, and 20 mA AC ripple at 1000 Hz.

No effort is made to synchronize the opening of the disconnect with the current zeros; it is not necessary to do so. At the instant the contacts part, whatever current that is flowing through them is quickly transferred to the RC snubber, so on the time scale of Figure 21, the current through the contacts makes a step change to zero. At that point the current flows through the RC snubber. There is a very small step in voltage, on the order of 2 V, generated by the step change of current through the snubber resistance. The major portions of the voltage are from the DC and AC components of the leakage current. The instantaneous contributions of these two sources at the instant of contact parting are both zero, because the voltages on the various capacitors in the circuit cannot change instantaneously. The AC component of the recovery voltage results from a voltage divider action between the capacitors, with an instantaneous value at contact parting of zero. The DC component of the leakage current produces an exponential decay in current as it charges the disconnect snubber capacitor, so there is a component of voltage across the contacts that rises exponentially to 10 kV. There is also a small contribution to the recovery voltage as a result of the interaction between the disconnect snubber capacitor and the breaker inductance, but it is small because the product of the residual leakage current times the equivalent surge impedance (square root of L/C) of the snubber capacitor and breaker inductance is small. Therefore, the major contribution to the recovery voltage imposed on the disconnect after its contacts separate results from charging the snubber capacitor via the breaker leakage current.

In order to determine how large C must be, we must consider the DC leakage current, and how quickly we can allow the 10 kV to appear across the contacts after they part. It should be possible to achieve full contact gap in 100 μsec, so the time constant formed by C and the equivalent leakage resistance should be set appropriately. A time constant of around 1 msec should be more than adequate. With a DC leakage current of 2 mA at 10 kV, the equivalent leakage resistance is 5 MΩ. To achieve a 1 msec time constant, C should be around 200 pF, which is a very small value.

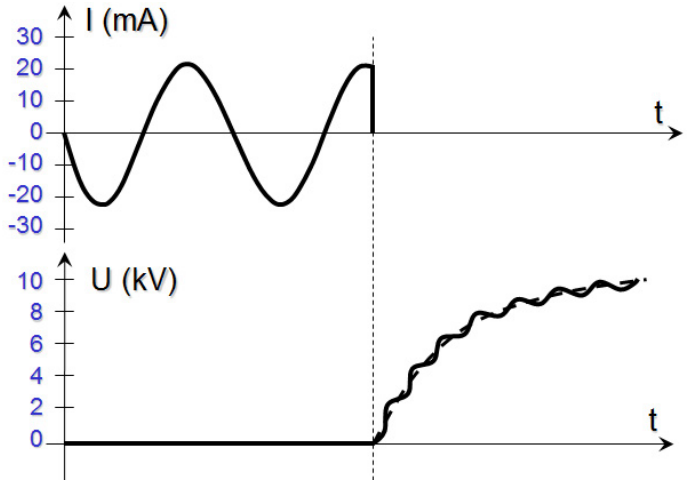


Figure 21.—Current and Voltage During the Opening of Disconnect

In order to determine R, we must consider how much voltage we can allow across the switch as it opens, and how much current we can allow as it closes. With a target of 2 V during opening, with 20 mA, R should be approximately 100 Ω. During closing, with the snubber capacitor charged to 10 kV, there will be a current pulse with 100 A peak and time constant of 0.02 μsec, which does not present any issues.

### 4.3.1 DC Contactor Preliminary Sizing Model

Table 8 provides the basis for a sizing scalar. Major component masses were estimated for a design point, which then allows calculation of a kW/kg scalar of 1540 kW/kg. It is notable that containment and packaging mass are estimated to be quite low due to the small volume of active components.

The loss model assumes that the experimental values of ~1 μΩ can be achieved at current levels, which would span the range of the study voltages.

## 4.4 Hybrid AC Breaker

There are two general approaches on implementing a hybrid AC breaker for use in the propulsion electric grid, depending on whether or not we are looking for a fault-current-limiting breaker, or if all we need is interruption of the fault current at the first naturally occurring current zero. If current-limiting is required, the thing to do is to use three of the hybrid DC breakers shown in Figure 19 for three phase current-limiting AC service as well, with some minor changes. For AC service, the logic for sizing the components in Figure 19 changes. It is recommended to do some simulations when it comes to implementation time to determine appropriate sizes of the components. In the case of AC service, residual leakage current through the breaker after it operates is on the order of 20 mA AC, so there is an excellent chance that a temporary fault will clear. If it does clear, the breaker can execute a fast reclose / reset operation as described for the DC breaker. If it does not clear, then the backup strategy is to turn off the generator and turn it back on. If that fails, then the generator will have to be taken out of service.

If current-limiting is not required, then the hybrid AC breaker can be implemented using thyristors. One pole is shown in Figure 22. There is a cryogenic contactor to carry load current during normal conditions, two anti-parallel thyristors to provide soft switching of the contactor, and possibly a snubber capacitor to limit the rate of rise of recovery voltage across the thyristors. In this case, a ZnO suppressor is not needed, because operation of the breaker does not trap any inductive energy.

TABLE 8.—CONTACTOR DESIGN POINT SIZING

| | |
|---|---|
| Rated Current | 1,000 A |
| Rated Voltage | 10,000 V |
| Power | 10,000 kW |
| Major Components | |
| Switch | 3 kg |
| Snubber RC | 1.00 kg |
| Subtotal | 4.00 kg |
| Bracket and wiring adder | 20% |
| Bracket and wiring adder | 0.80 kg |
| Volume | 0.004 |
| Containment mass | 1.69 kg |
| Total Mass | 6.49 |

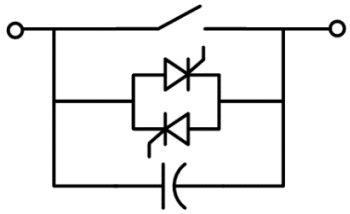

Figure 22.—Proposed Hybrid AC Breaker

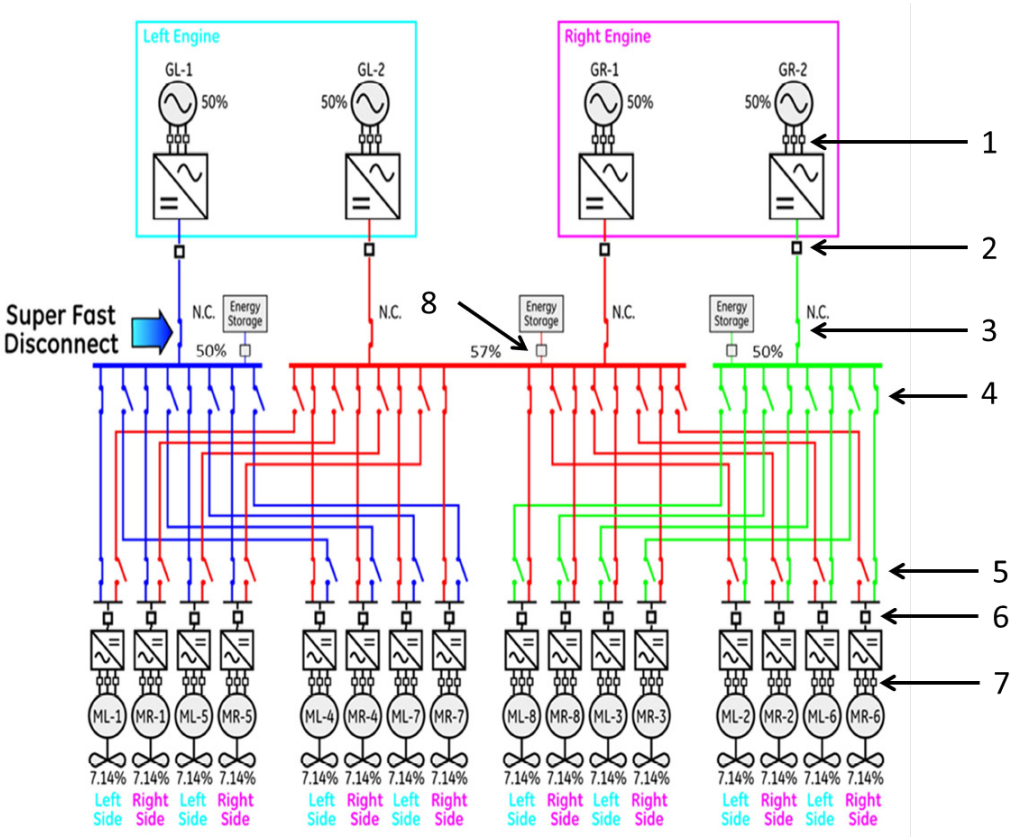


Figure 23.—Switching Devices in Architecture 1

Under normal conditions, the thyristors are gated on, just to be always ready. In the case of a fault, the contactor is opened. In this case, speed of the contactor is not as important as for the DC case, but we will assume the use of the same contactor as for the DC case, since it will be available, and that the time between contact parting and fully open contacts is 100 µsec. So, 100 µsec after contact parting, gating of the thyristors is turned off, and the fault is cleared at the first natural current zero.

The thyristors are sized for full system voltage, and for ½ cycle of full fault current.

## 4.5 Breaker and Disconnect Locations

Figure 23 shows Architecture 1 with eight switching devices by number. The types of those switches are described below.

- Switch 2, 6, and 8 are hybrid DC breakers
- Switch 3, 4, 5 are DC disconnects
- Switch 1 and 7 are hybrid AC breakers

All of the three types are addressed in detail in the previous sections.

## 4.6 Hybrid DC Breaker Operation in the System

This section provides more detail for two aspects of the operation of cryogenic hybrid breakers during fault interruption in a turboelectric distributed propulsion electric grid that were observed during simulations:

1. For a fault at the terminals of a motor, the fault current flows through two hybrid breakers. As a result, there are two inductors instead of one inductor in series during the rise and interruption of fault current. Consequently, compared to a fault at a generator bus, the fault current rises and falls more slowly and fault clearing time and dissipated energy increases a little bit.
2. After the fault current falls essentially to zero, the incremental resistance of the ZnO snubber is very high. As a result, there is very little damping for the voltage oscillations produced by the interaction of the snubber capacitor and the series inductor, and a ringing voltage is produced after the interruption is complete.

### 4.6.1 Motor Faults

The relevant circuit for a motor fault is shown in Figure 24. There are two inductors in series with the fault. This will lower both the rate of rise of current prior to breaker operation and the rate of fall after the breaker opens. This will have the following consequences:

1. The amount of current flowing when the breaker opens will not be as large as for a bus fault.
2. The amount of time required to drive the current to zero will be slightly larger than for a bus fault.
3. The amount of energy dissipated by the ZnO snubber will be slightly greater than for a bus fault.

It is useful to examine four relevant cases:

1. Bus fault at full voltage.
2. Bus fault at reduced voltage.
3. Motor fault at full voltage.
4. Motor fault at reduced voltage.

For the purposes of this discussion, full voltage is 10 kV and reduced voltage is 8 kV. The ZnO is designed to clamp at 20 kV. The series inductor is 1 mH. Nominal load current is 1 kA. The time between fault detection and breaker operation is 100 μsec.

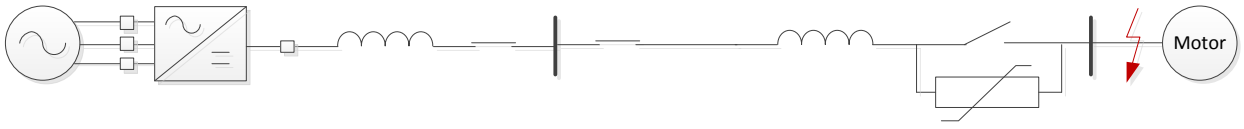


Figure 24.—Circuit Condition for Motor Fault

For a bus fault at full voltage, 10 kV, the current starts from 1 kA and rises to 2 kA, 100 μsec after the fault. The breaker operates and the ZnO clamps at 20 kV. This applies 10 kV across the inductor, producing a rate of change of current of negative 10 A/μsec. It takes an additional 200 μsec for the current to fall to zero. During that time, 4000 J are dissipated in the ZnO. In summary:

- System voltage: 10 kV
- Fault location: bus
- Total time to operate: 300 μsec
- Peak current: 2 kA
- Energy dissipated in ZnO: 4000 J

For a bus fault at reduced voltage, 8 kV, the current starts from 1 kA and rises to 1.8 kA, 100 μsec after the fault. The breaker operates and the ZnO clamps at 20 kV. This applies 12 kV across the inductor, producing a rate of change of current of negative 12 A/μsec. It takes an additional 150 μsec for the current to fall to zero. During that time, 2700 J are dissipated in the ZnO. In summary:

- System voltage: 8 kV
- Fault location: bus
- Total time to operate: 250 μsec
- Peak current: 1.8 kA
- Energy dissipated in ZnO: 2700 J

For a fault at the motor, there are two inductors in series. With full system voltage, 10 kV, for a fault at the motor terminals, the fault current through the breaker rises at a rate of 5 A/μsec to a peak current of 1.5 kA. The breaker operates and the ZnO clamps at 20 kV. This applies 10 kV across the pair of inductors, producing a rate of change of current of negative 5 A/μsec. It takes an additional 300 μsec for the current to fall to zero. During that time, 4500 J are dissipated in the ZnO. The two inductors form a voltage divider that places 15 kV on the generator buss. In summary:

- System voltage: 10 kV
- Peak bus voltage: 15 kV
- Fault location: motor
- Total time to operate: 400 μsec
- Peak current: 1.5 kA
- Energy dissipated in ZnO: 4500 J

Finally, with a system voltage of 8 kV, for a fault at the motor terminals, the fault current through the breaker rises at a rate of 4 A/μsec to a peak current of 1.4 kA. The breaker operates and the ZnO clamps at 20 kV. This applies 12 kV across the pair of inductors, producing a rate of change of current of negative 6 A/μsec. It takes an additional 233 μsec for the current to fall to zero. During that time, 3266 J are dissipated in the ZnO and 13 kV appears at the generator bus. In summary:

- System voltage: 8 kV
- Peak bus voltage: 13 kV
- Fault location: motor
- Total time to operate: 333 μsec
- Peak current: 1.4 kA
- Energy dissipated in ZnO: 3266 J

Comparing the full voltage bus fault with the full voltage motor fault we see that the energy dissipation is increased slightly from 4000 to 4500 J, and the total operating time is increased from 300 μsec to 400 μsec.

### 4.6.2 Ring Down

During simulations, a ringing transient voltage was observed after interruption. Figure 25 is a typical example. The top figure is the voltage across the ZnO and the lower figure is the current through the ZnO during ZnO operation. The mechanism producing the transient is the interaction between the snubber capacitor and the series inductor after the ZnO stops conducting. The question arose whether or not the transient is a real effect, or perhaps it was an artifact of the simulation. Analysis shows that for the circuit used, some ringing is expected, but it is not likely to be as pronounced as shown. For the actual circuit, its amplitude will depend on subtleties that would be difficult to model in a simulation, such as the values of stray capacitance and stray inductance in the circuit, and the high frequency losses of the series inductor.

Although there are no obvious problems that the ringing might engender, intuitively it would seem to be a good idea to prevent them if possible. There is a relatively easy way to do so, by increasing the high frequency losses of the series inductor. This can be done by connecting a resistor in parallel with the inductor. The breaker circuits before and after the addition of the resistor are shown in Figure 26 and Figure 27. The much cleaner post-interruption voltage waveform is shown in Figure 28.

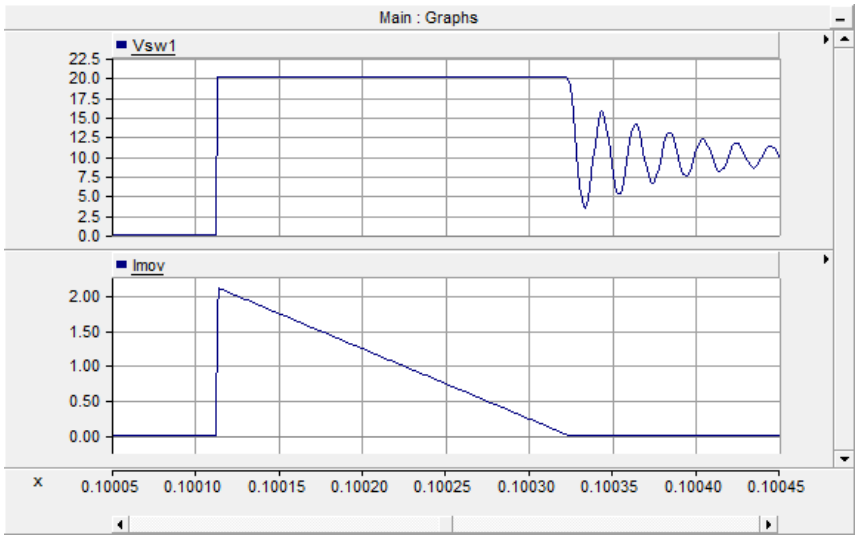


Figure 25.—Typical Voltage Ringing after ZnO Suppresses Overvoltage

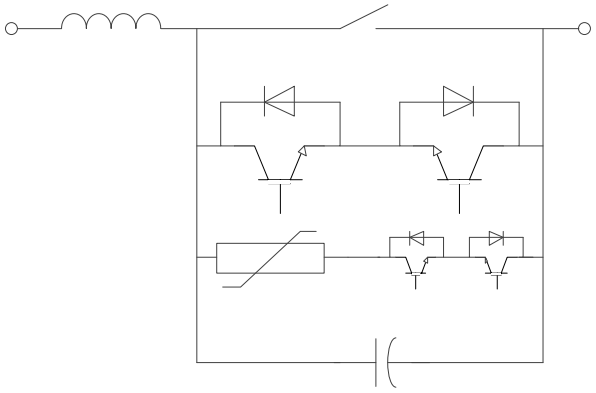

Figure 26.—Original Hybrid DC Breaker Circuit

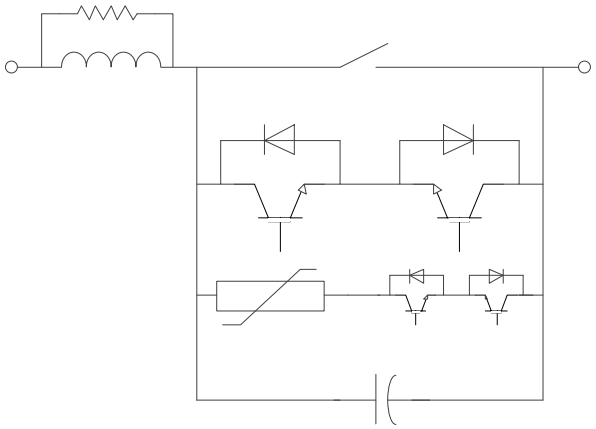

Figure 27.—DC Circuit Breaker with the Additional Resistance

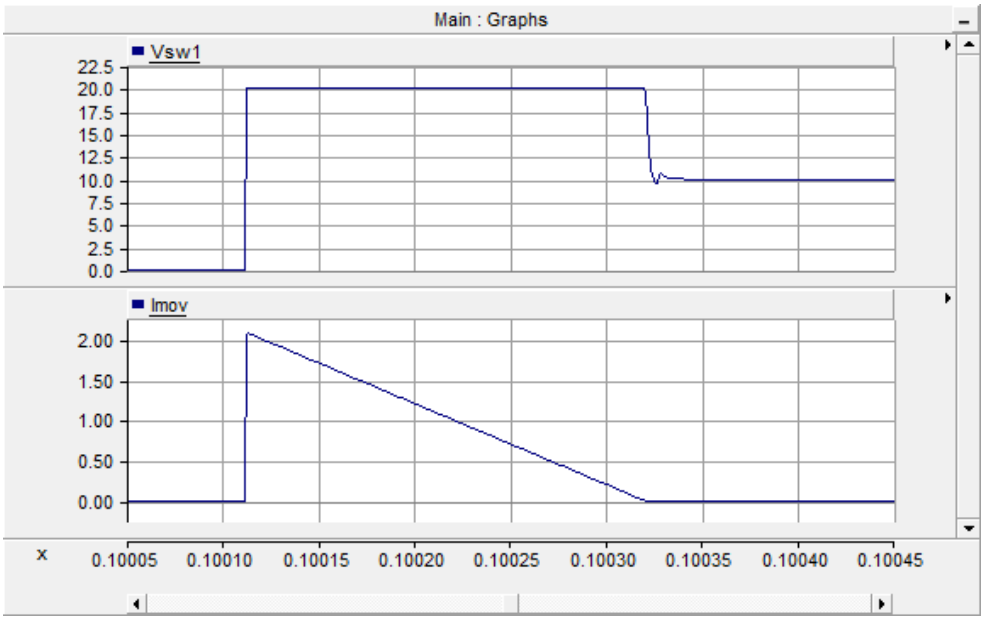


Figure 28.—Effective Voltage Waveform After Adding Additional Ramping Resistance

The value of the resistance is not critical; there are a broad range of values that will work. It should not be so low as to significantly add to the fault current, but it should be low enough to provide damping. An order of magnitude computation indicates it should be approximately equal to the square root of the ratio of the series inductance over the snubber capacitance, which is about 30,000 Ω. However, since it is likely that stray capacitance is likely to be several picofarads, we may wish to raise the value of the snubber capacitance a bit, which would lower the required value of resistance. It could be dropped down quite a bit from 30,000 Ω without substantially raising the fault current. For example, a value of 1,000 Ω would provide plenty of damping, with a contribution to the fault current of only 10 A.

Furthermore, the steady-state rating of the resistor is zero, since it normally does not carry any current. What does matter is the amount of energy it will absorb. For a 1,000 Ω resistor, the dissipation during fault interruption is only 20 J.

Though potentially a minor effect, the desire to add this resistor was identified through system simulation discussed in the following sections.

# 5.0 Transmission Cable Considerations

Initially superconducting transmission cable mass estimates assumed only the superconducting core mass per unit length. This section addresses some assumptions to allow estimation of the transfer line, which refers to the line construction to carry cryogen and provide insulation through a vacuum jacket. Though the cooling system was not part of the study scope, some assumptions and calculations were required to make an estimate. As the reader will see in this and following sections, the transfer line mass, at the existing technology level, adds a significant mass to the transmission system mass estimate.

Based on the early analysis and literature on cryogenic semiconductors, a two operating cooling fluid system was assumed for the purpose of progressing system weight estimates related to the transmission lines. The cooling system is summarized below.

- Power Conversion Operating at ~150 K: Selected to minimize system losses (electrical and cooling).
- Electric Machines Operating at ~30 to ~60 K: Selected based on the assumption of machine incorporating state-of-the-art HTS into machines that would achieve TRL 4 to 6 in the 2025 timeframe, given that these HTS materials require cooler temperatures for moderate fields. It is recognized and acknowledged that ventilation of the same electric equipment enclosure with electronics and machinery cooled by different cryogens at different thermodynamic state will introduce heat transfer challenge requiring a novel approach. Our assumption is that this challenge is not a show-stopper, and will avail itself to a practical engineering solution.

If these assumptions change and technologies advance, it is still anticipated that the models presented will provide an approach to updating estimates. For example, a single coolant at another temperature could be selected and the system resized.

Lastly, in order to estimate the weight and thermal (heat leak and pumping pressure drop) losses of the transmission system, the cooling approach and fluids were required. Use of a supercritical fluid was assumed, referencing earlier DOE-funded, Fusion Energy studies (Refs. 36 and 37) of cryogenic convection heat transfer along elongated flow paths with distributed heat input For cryogen flow in transfer piping, loop pressurization to the supercritical state is attractive compared to saturated or subcritical states because it avoids two-phase flow transition events and associated hydrodynamic instabilities that can be prevalent in other thermodynamic regimes. Forced convection heat transfer coefficients on the order of 1 $kW/m^2$-K are achievable with supercritical flows.

Furthermore, by tuning flow rate and path inlet conditions, supercritical flows can be engineered to resist temperature rise (or even cool) as they absorb heat from external sources (Refs. 38 and 39). Supercritical $N_2$ and Ne were selected for the power electronics and superconducting loops respectively. If need be, the superconducting loop model / sizing can be updated for lower temperature operation with hydrogen to enable machine sizing at increased power density.

Two submodels were developed: one for the supercritical $N_2$ flow loop, cooling both generator and motor power conditioning electronics, the other for the Ne-cooled superconducting transmission cable and machinery windings. Both submodels include a 1-D flow network and associated heat transfer calculus to estimate cryogen pressure drop and temperature change from inlet to outlet, based on user inputs as well as parameter value exchange with the master system sizing model. The $N_2$ submodel is informed by vacuum-insulated, corrugated transfer tube technology (commercially available, with design information embedded in the model). The other submodel is similar, but substitutes Ne for $N_2$ and adds HTSC transmission line technology (commercially available, with design information embedded in the model). In both submodels, the commercial component information includes key design geometry, bend radii limits, ampacity ratings, heat leak, and weight values as look-up tables or curve fits. Accordingly, the TeDP sizing studies are limited by interpolation within the present range of embedded values.

Cryogen supply conditions are also constrained based on the currently-hypothesized temperature and pressure ranges. If needed, that range can be shifted or expanded by updating the submodels.

Figure 29 and Figure 30 show the $N_2$ and neon cooling system layouts used for estimation of coolant flow, transmission line sizes, heat leak, pressure drop, and pumping power. As can be seen, central manifold and breaker boxes are assumed; this will likely not be the case in practice when designing for redundancy, but it provides a reasonable basis for estimating transfer line lengths and size. These configurations are used only to estimate cable and transfer line estimates, but no other equipment shown on the diagram. Additional assumptions used with these structures for system estimates are listed below:

- N3-X fuselage dimensions
- 213 ft wingspan:
  - Power plants / generators located at wing tips.
  - Propulsion fans / motors proximal to airframe center.
- Pristine DC power output from generators. Zero harmonic content.
- Circuit breakers cooled by Ne.
- Ohmic losses of HTS splices are negligible.
- Landing shock, aircraft maneuver, and wing flexure do not quench HTS bus.
- Electrical intertie between neon-cooled and $N_2$-cooled circuits established by resistive current leads that are conduction-cooled (passive heat-sinking; no cryocooler-anchored thermal intercept station).

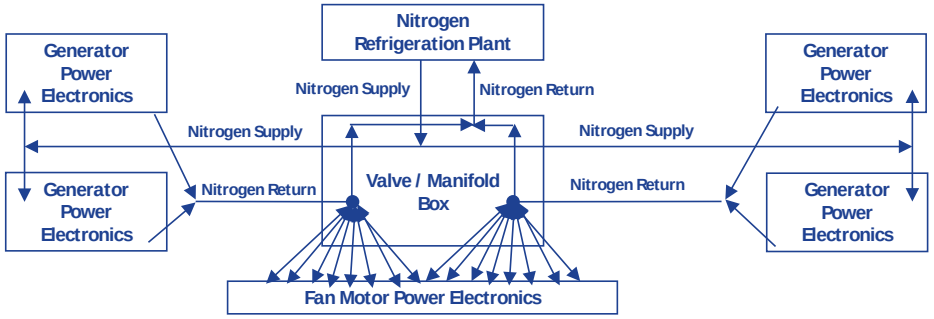


Figure 29.—Nitrogen Cooling System

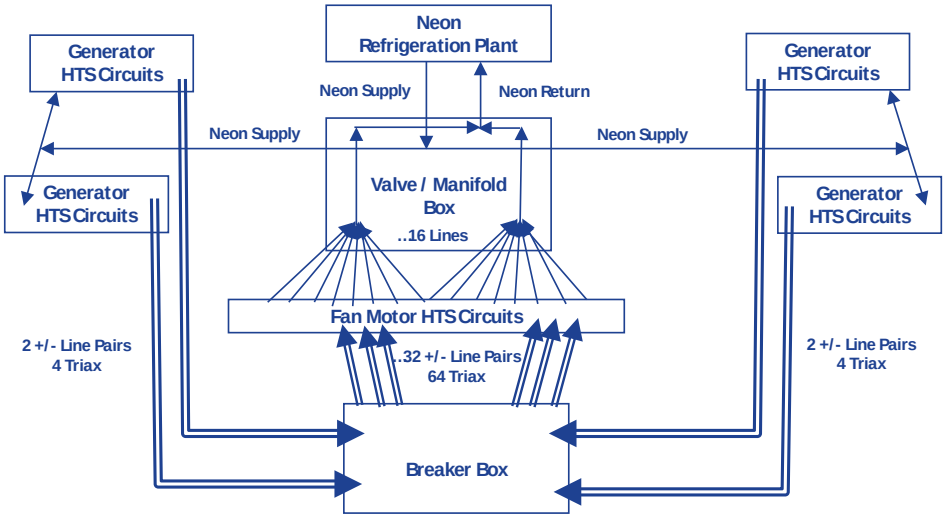


Figure 30.—Neon Cooling System

The following assumptions resulted in a significant mass increase compared to the HTSC core only estimates made earlier in the study. Length estimates increased significantly due to bend radius assumptions. The mass estimates shown in Table 9 assume an 8 kV bus voltage. Mass per unit length for both the transfer line and superconductor core are included and are based on the power requirements of the cable lengths estimated and the masses listed in Section 6.6.

TABLE 9.—TRANSMISSION AND DISTRIBUTION MASS ESTIMATE

| | |
|---|---|
| Ne System | |
| HTSC | 1070 kg |
| Transfer Line | 3477 kg |
| Ne Cryogen | 210 kg |
| $N_2$ System | |
| Transfer Line | 432 kg |
| $N_2$ Cryogen | 81 kg |
| Total | 5270 kg |

# 6.0 Component Sensitivities to Voltage

## 6.1 Sensitivity of Components to System Bus Voltage

The first order mass and efficiency sensitivity of components to bus voltage is simply summarized in Table 10. This table assumes a given power level and a voltage range from approximately 1 to approximately 10 kV.

Electric machines have already been shown to scale with power; the remaining three component classes are discussed below. At the end of this section, a summary is provided of mass efficiency scalars that can be used for study.

## 6.2 Sensitivity Analysis of Weight and Efficiency for Transmission Lines

The transmission lines are weight-sensitive to a voltage change at fixed power example. A decrease in voltage results in an increased current requiring more current-carrying superconductor. It should be noted that a significant portion of mass associated with state-of-the-art superconducting transmission lines is associated with cooling and insulation of the line. Estimates including the construction for cooling and insulation become more complicated as it involves feeders of various power levels, cooling flow requirements, and step changes in the overall size of tubes. These were provided as part of a study sizing tool spreadsheet, but a plot, Figure 31, can be used as a generalization.

In Figure 31, transmission line mass is shown to decrease with increasing voltage. In addition to the HTSC mass, the transfer line that carries the cryogen and provides the vacuum jacket must also be included. Across the range of voltages considered this was estimated as 4 kg/m. Using these numbers and an HTSC line length of 700 m, the mass as a function of voltage can be estimated. This will be similar to the spreadsheet tool, but not identical due to the tool's additional detail in transfer line mass estimates and lines of different ratings supplying to different components (motors and generators).

The reader will note that the majority of the mass is the transfer line, not the HTSC core.

## 6.3 Sensitivity Analysis of Weight and Efficiency for RTAPS Hybrid Breakers / Disconnect Switches

To a first approximation, the size, weight, and losses of RTAPS hybrid breakers and disconnects depends only on rated power (rated voltage time rated current), with no dependence on system voltage, over a modest range of system voltage, such as from 5 to 50 kV.

At a high level, this can be seen as a result of the fact that it is possible to design a building block breaker or disconnect module of a certain voltage and current rating, and then connect the modules in series / parallel to achieve a higher voltage and current rating. Suppose that the system voltage is M times the voltage rating of the building block, and system current is N times the current rating of the building block. Then, M*N building blocks will be required, M in series, N in parallel. The overall size, weight, and losses will be M*N times the size, weight, and losses of a single building block.

TABLE 10.—FIRST ORDER SENSITIVITY FOR
VOLTAGE RANGE OF ~1 TO ~10 kV BUS VOLTAGE

| Component | Weight sensitivity | Efficiency sensitivity |
|---|---|---|
| Electric machines | No | No |
| Power conversion | Yes | Yes |
| Protection Breakers and Contactors | No | Yes (small impact) |
| Transmission lines | Yes | No |

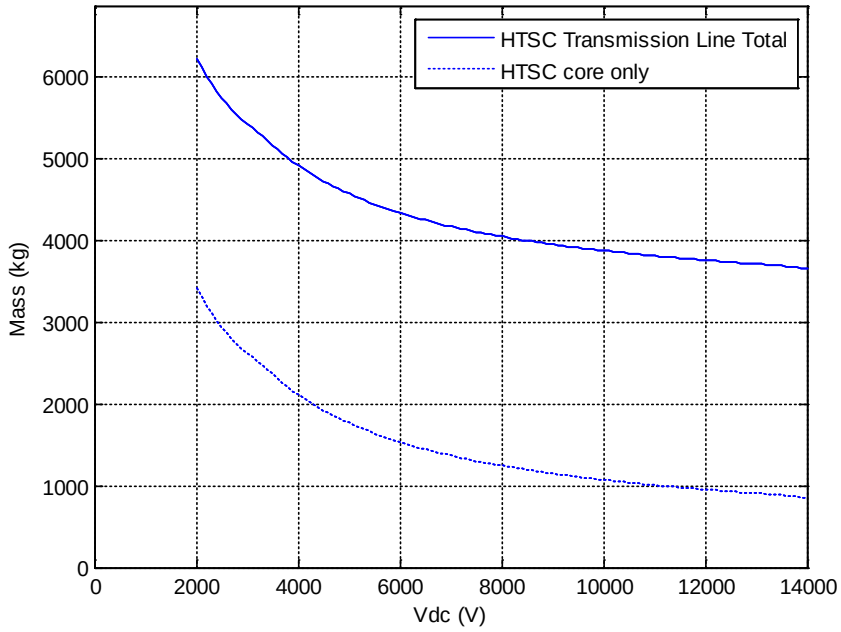


Figure 31.—HTSC Core and Total Transmission Line Mass (700 m) vs. DC Link Voltage

It is useful to explore the design of two of the major components of the hybrid breaker: the ZnO surge suppressor, and the electronic snubbers.

For the ZnO, the key design constraints are the maximum allowable electric field and current density in the material. Consider a ZnO cylinder. The required area of the cylinder is equal to the peak current divided by the maximum allowable current density. The required height of the cylinder is equal to the peak voltage divided by the maximum allowable electric field. Therefore, the size and weight of the cylinder is equal to the peak current times peak voltage divided by the product of maximum allowable current density times maximum allowable electric field. In other words, the size of the ZnO is proportional to the rated power of the grid being protected.

A similar argument, based on electric fields and current density, holds true for the electronic snubbers.

For the contacts themselves, several identical contacts can be placed in series and parallel to achieve a given voltage and current rating. It can be shown that the total losses will be proportional to the number of contacts needed.

The only components of the breakers and disconnects that may depend on system current rating are the superconducting connections between other components. Since their sizing depends mainly on current, as the system voltage rating goes up, for a given power, the current rating will go down, so the size of the superconducting connections should go down. However, the size and weight of the connections is a small fraction of the total for the breakers and disconnects, and can be ignored in a first approximation.

## 6.4 Sensitivity Analysis of Weight and Efficiency for Power Converters

The purpose of this effort is to understand the impact of the DC link voltage to the weight and efficiency of the power converter under cryogenic environment. Three major components of the power converter are considered: power stack, passive filter, and cooling system. Three-level Neutral-Point-Clamped (NPC) converter topology (as shown in Figure 32) is selected for the study, since it is widely used in the power industry for medium voltage power conversion application.

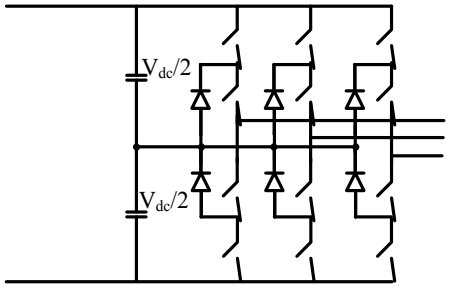


Figure 32.—Three-Level NPC Converter

### 6.4.1 Power Stack

The power stack consists of the semiconductor devices, the auxiliary circuits, and the bus bars. As discussed in the previous report, Si-based IGBTs are preferred in cryogenic environment due to its improved loss performance. The output characteristics curve of the IGBT will be very steep at low temperature, which means the forward voltage drop is not sensitive to the current flowing through the device. In this study, the forward voltage drop of the IGBT is assumed to be 1 V per IGBT, regardless of the voltage rating of the device. The switching loss of IGBT will also be reduced significantly at cryogenic temperature, mainly due to the reduced tailing time (Ref. 40) and the improved diode reverse recovery performance (Ref. 41). The turn-on loss and turn-off loss at cryogenic condition are assumed to be reduced to 50 and 20 percent, respectively compared to operation at room temperature. Three commercial IGBTs (FZ750R65KE3, FZ1200R45KL3, FZ1200R33KL2C) are used as the benchmark to extrapolate how the switching loss and the power density vary with the device rated voltage. Although mature and widely used in the high power industry, the technology of Si IGBT is still evolving (Ref. 42). This results in a projection of 20 percent improvement for the switching loss is assumed in the study.

For device voltage rating selection, a safety factor of 0.6 is applied. For example, if the voltage across the device is 2 kV when the device is turned off, then a 3.3 kV device will be selected. The maximum single device rating is assumed to be 10 kV. If the required blocking voltage is higher than 12 kV, two devices will be put in series as one switch unit.

In this study, the switching frequency of the IGBT is considered to be a function of the device rated voltage. In general, the device with higher voltage rating will have lower switching speed and higher switching loss, and, therefore, the maximum feasible switching frequency will be lower. Considering the common practice, we choose 1.8 kHz for the 3.3 kV device and 600 Hz for the 10 kV device. Then the switching frequency for any other voltage rating can be extrapolated. The fundamental frequency is assumed to be 60 Hz in the study. Since the ratio of the switching frequency over the fundamental frequency is not high, the switching frequency is rounded to be the integral multiple of the fundamental frequency in order to avoid subharmonics. Therefore, the variation of the switching frequency is not continuous.

### 6.4.2 Passive Filter

The design of passive filters involves many different aspects of the system, including system stability, standards applied to the system, hardware layout, control and modulation scheme, etc. Some of the aspects require very detailed converter design, e.g., the EMI consideration, since it is related to not only the converter voltage / current / control setting, but also the parasitics inside the converter and the ground connection. In this study, we choose Total Harmonic Distortion (THD) and energy storage as the criteria for sizing the passive filter. This approach avoids the excessive details of the converter hardware design, and it represents a good lump-sum estimation of the passive components for the sensitivity study.

Spectrum analysis is performed to extract the harmonic voltage content at the output of the 3-level NPC converter, with which the required inductance to meet certain THD requirement can be calculated. Five percent THD is assumed in the study. For the DC link capacitor, its main function is to maintain the stability of the bus and minimize the voltage ripple. The energy storage requirement is applied for the capacitance selection (Ref. 43). In this case, we assume that the DC link voltage will not drop below 90 percent of the rated value even if the input power was interrupt for three switching cycles.

The sizing of the inductor follows the same approach as the one used to size the inductor of the hybrid circuit breaker. It is an air core design. The sizing of the capacitor is based on energy storage. A film capacitor is selected due to its good energy density and reliability. The state-of-the-art energy density of the film capacitor is 0.4~1 kJ/kg. A 5 kJ/kg is used in the sensitivity study as future projection (Ref. 44).

### 6.4.3 Cooling System

The power stacks (including the DC link capacitors) of the converter are installed in a cryogenic tank or vessel in order to maintain the low operating temperature for the semiconductor device and minimize interconnection between difference interfaces. All the electronics components are assumed immersed in the cryogen. The weight and volume of the coolant and the tank depend on the volume of the power stacks and the package fill factor. The fill factor represents the fraction of volume that is occupied by the power stacks. The fill factor of the present medium voltage converter is below 0.2. For this aerospace case, a projection of 0.4 is used.

The approach to size the tank is the same as the one used for the containment of the hybrid DC circuit breaker.

### 6.4.4 Conclusion

Figure 33, Figure 34, and Figure 35 show results for the voltage sensitivity study. The saw tooth shape ripple is due to the quantization effect of the switching frequency, as described in the power stack section.

From 2 to 12 kV, only one IGBT is used for each switching unit in the converter. When the DC link voltage is higher than 12 kV, two IGBTs in series are used for each switching unit since the required rated voltage is higher than 10 kV, which is the assumed maximum voltage rating for a single device.

As shown in Figure 33, the converter efficiency increases with the DC link voltage when the DC link voltage is lower than 12 kV. It is mainly due to two factors. Firstly, at cryogenic condition the device forward voltage drop is not sensitive to the amplitude of the current and the device voltage rating. As far as single IGBT device is used for each switching unit, higher DC link voltage will lead to lower current, and, therefore, lower conduction loss. Secondly, as mentioned in the previous section, the switching frequency will reduce if the voltage rating of the device increases. Therefore, the effect of higher switching loss of the high voltage rating device is compensated. When the DC link voltage is higher than 12 kV, two IGBTs in series will be needed. The forward voltage drop for each switching unit is doubled, which causes the step change in the efficiency.

Figure 34 shows the weight breakdown of the converter and Figure 35 shows the overall weight density. As the DC link voltage increase, the size of the power stack reduces due to the improved power density of the higher voltage rating device. However, the size of the passive filter increases because of the reduced frequency. It creates a sweet spot in the voltage range of 4 to 8 kV. When the voltage crosses 12 kV, two devices with lower voltage rating in series will be used. Here a higher switching frequency is feasible and leads to a step reduction in the system weight.

These results are included in the sizing tool as curve fits over the 2 to 10 kV voltage range.

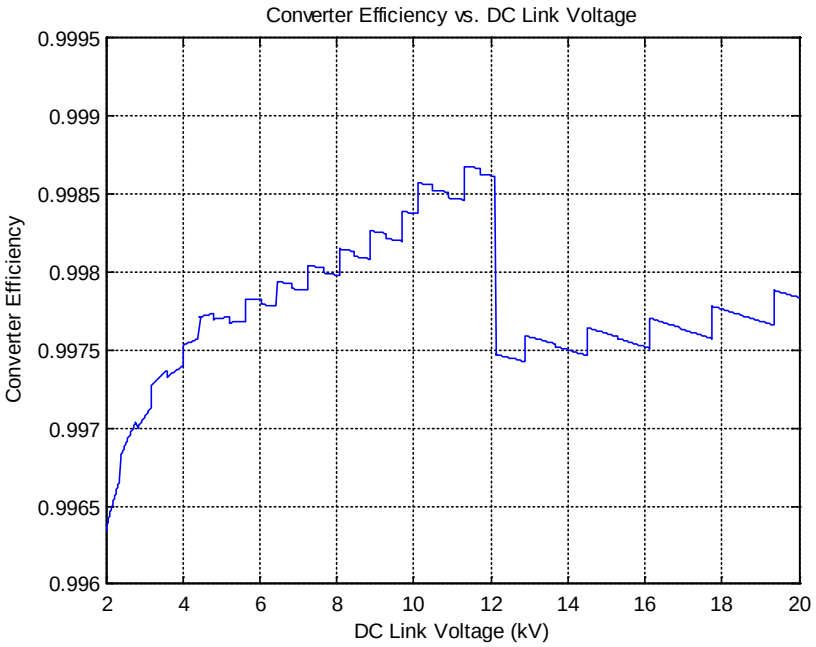


Figure 33.—Efficiency versus DC Link Voltage

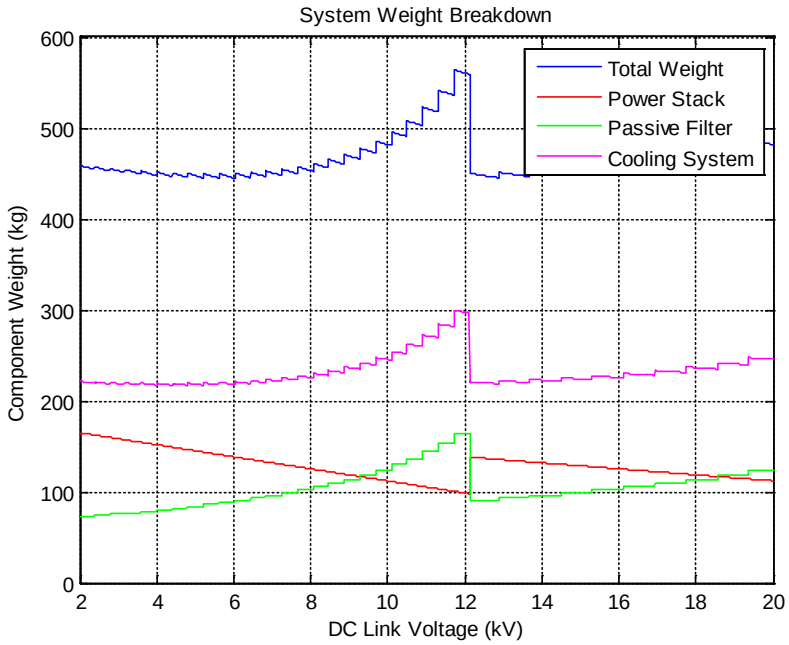


Figure 34.—Power Converter Weight versus DC Link Voltage (Note: "Cooling System" refers only to cryogenic pressure vessel, and not cryocoolers.)

## 6.5 Sensitivity and Scalar Summary

### 6.5.1 Generators and Motors

As described above, generator and motors are scaled largely on power, not voltages. Machine design was not the focus of this tasked order, so recent NASA RTAPS reports were used to select mass and efficiency models or scalars, see Table 11.

### 6.5.2 Breakers and Contactors

Breaker and contactor models or scalars were developed by completing a conceptual sizing for a given rating and then scaling with power. The components that make up the hybrid breaker or contactor would all scale with power. An important assumption in the scalars below is that these components would be part of a pressurized system up to 650 psi. This results in a minimum mass for a pressure vessel, which for the AC breaker and DC contactor may be reasonable as a housing even at lower pressures. For the larger hybrid breaker, the pressure vessel mass may decrease if the system pressure is reduced.

Efficiency is modeled as a resistance. As reported earlier, a combination superconducting material and silver contact patch were proposed based on literature. It was assumed that contact resistance of $1\times10^{-6}$ Ω could be achieved for all contactors regardless of current.

### 6.5.3 Power Conversion

Mass and efficiency models detailed above took into consideration estimates of projected device ratings, switching and conduction losses, and EMI filter components, as well as a simple estimate for a pressure vessel containment (Table 12). From these more detailed estimates, curve fits were used to provide scalars or models for use at the system level (Figure 36 and Figure 37).

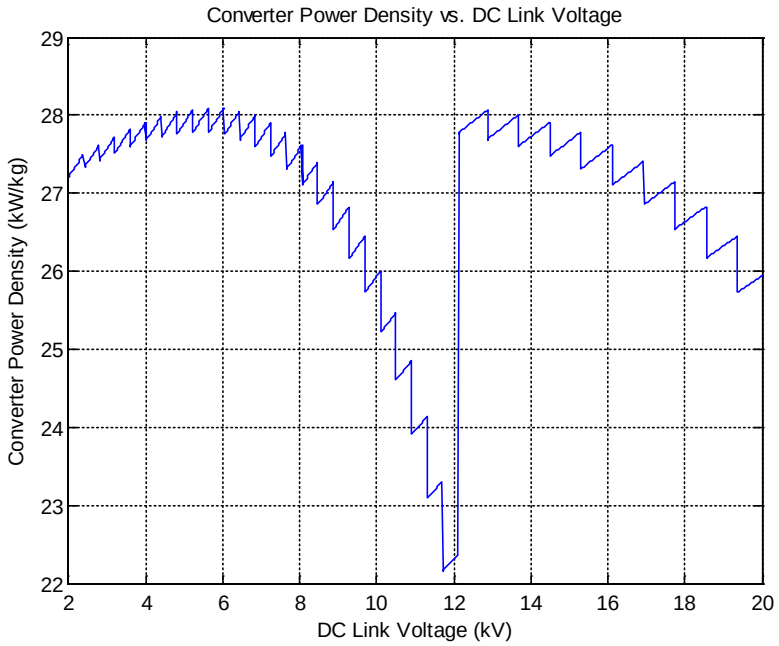


Figure 35.—Converter Power Density versus DC Link Voltage

TABLE 11.—GENERATOR AND MOTOR WEIGHT AND EFFICIENCY

| Component | Weight scalar | Efficiency (%) |
|---|---|---|
| Generator | 78.5 kW/kg | 99.955 |
| Motor | 47.1 kW/kg | 99.97 |

TABLE 12.—HYBRID BREAKER AND CONTACTOR POWER DENSITY AND EFFICIENCY

| Component | Weight scalar | Weight scalar with no pressure vessel | Efficiency |
|---|---|---|---|
| Hybrid AC Breaker | 329 kW/kg | 362 kW/kg | $1\times10^{-6}$ Ω per phase |
| Hybrid DC Breaker | 139 kW/kg | 188 kW/kg | $1\times10^{-6}$ Ω |
| DC Contactor | 1541 kW/kg | 2083 kW/kg | $1\times10^{-6}$ Ω |

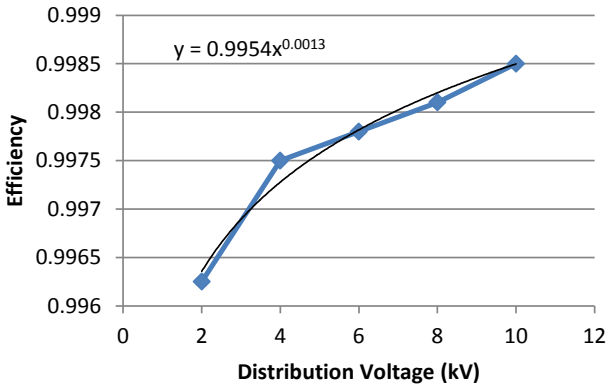


Figure 36.—Efficiency Relation

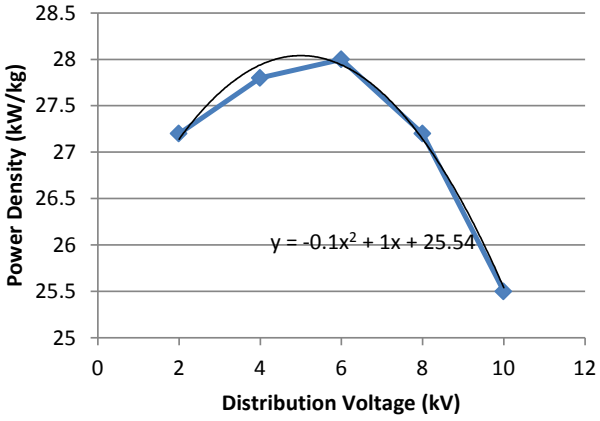


Figure 37.—Power Density Relation

TABLE 13.—HTSC CORE MASS PER UNIT LENGTH AS A FUNCTION OF DC CURRENT RATING
[+/- implies a "go and return"]

| Total triax cable DC ampacity (+/- kA DC) | HTSC core mass (kg/m) |
|---|---|
| 0.9 | 1.28 |
| 3.8 | 3.51 |
| 6.0 | 4.74 |
| 7.5 | 5.59 |
| 9.0 | 6.45 |
| 10.2 | 7.04 |
| 11.8 | 7.39 |
| 11.8 | 7.39 |

## 6.6 Superconducting Cables

The mass per unit length estimates for superconducting cables are based on product data from transmission lines shown in Table 13. Across the range of voltages considered and the power required by various feeder components, an adder of approximately 4 kg/m should be used to account for the transfer line which carries the cryogen and provides the vacuum jacket around the HTSC core. Efficiency is assumed to be 100 percent besides the impact of heat leak on the cryogenic system.

# 7.0 Narrowed Range of DC Voltage

## 7.1 Approach to Narrowed Range of DC Voltages

With nearly all estimates based on forward-looking projections and uncertainty in the development, it is desirable to understand the potential impact of incorrect projects and determine if a broadly applicable conclusion can be reached.

Based on the work of earlier milestones, this study need only consider the power conversion equipment (with its impact on cryocooling capacity) and transmission lines to evaluate the impact of DC link voltage. Three parameters were varied over a wide range to determine if incorrect assumptions or estimates would greatly impact the preferred DC voltage. All cases show the greatest decrease in the component mass, with increasing voltage, occurs by approximately 6 kV. For the architecture selected and the various component assumptions, a minimum occurs at about 8 kV. For cases where cable mass and cryocooler mass dominate, the minimum mass is achieved at the highest voltage achievable without the need of paralleling two devices in a single switching unit (12 kV in this study). Though the cases with higher cryocooler power density may indicate a lower system mass with adoption of a 3-level power converter, it should be noted that this system mass is similar to the minima at a lower voltage with a 2-level power converter. Given the wide range of estimates in length and power densities, a voltage of over 6 kV would capture much of the weight reduction; a minimum may occur between 6 kV and 10 to 12 kV.

## 7.2 DC Voltage Range Selection

After more detailed consideration of all the major system components above, the sensitivities summarized in the last section indicate that the voltage range selection can focus on the power conversion equipment and transmission lines. The impact of transmission lines is simply that higher voltage allows smaller, lighter lines for a given system power (lower current). For power conversion, both efficiency and weight are sensitive to voltage. Efficiency impacts weight as the losses impact the mass of the cryocooling system. It should be noted that this study is assuming all components will be in a pressurized cryogenic environment which will also serve to provide the electrical isolation.

The relevant trends for the power electronics and transmission line masses as a function of voltage, for the architecture selected under this contract, are shown in Figure 38 to Figure 41. From Figure 38 and Figure 39, it should be noted that power electronic losses, and thus cooling system weight, decrease with increasing voltage. Power conversion efficiency is applied to ~100 MW, which is 50 MW generator power converters and 50 MW motor power converters. These losses then need to be removed by the cryocooler system.

In Figure 40, transmission line mass is shown to decrease with increasing voltage. In addition to the HTSC mass, the transfer line that carries the cryogen and provides the vacuum jacket must also be included. Across the range of voltages considered, this was estimated as 4 kg/m. Using these numbers and an HTSC line length of 700 m, the mass as a function of voltage can be estimated. This will be similar to the spreadsheet tool but not identical, due to the tool's additional detail in transfer line mass estimates and lines of different ratings going to different components (motors and generators). Electrical insulation mass within feeder is minimal compared to the transfer line that provides the vacuum jacket and cryogen flow path.

From Table 13 and Figure 40, the reader will note that the majority of the mass is the transfer line, not the HTSC core. Later plots in this report will vary parameters to show trends if total transmission line mass per unit length were less.

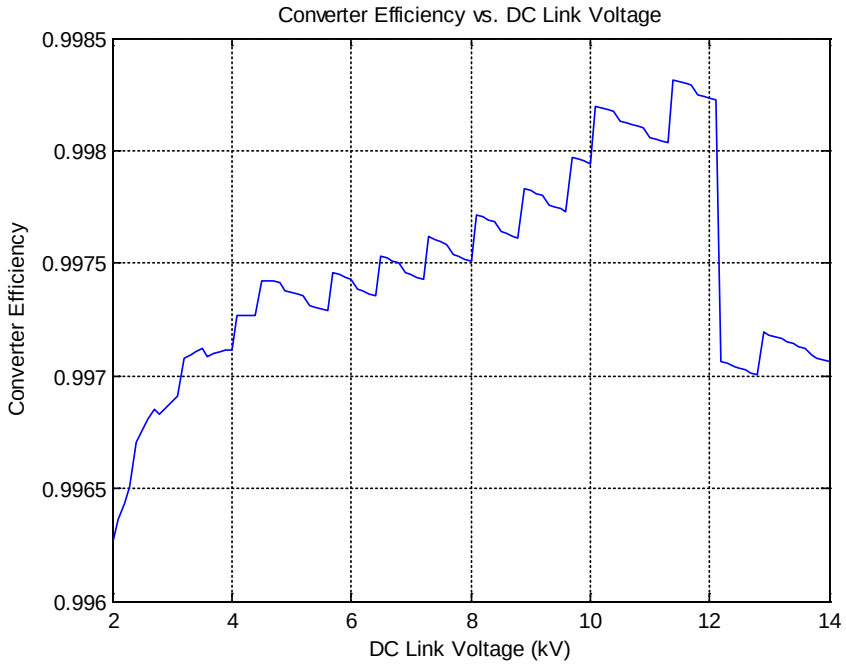


Figure 38.—Power Converter Efficiency vs. DC Link Voltage

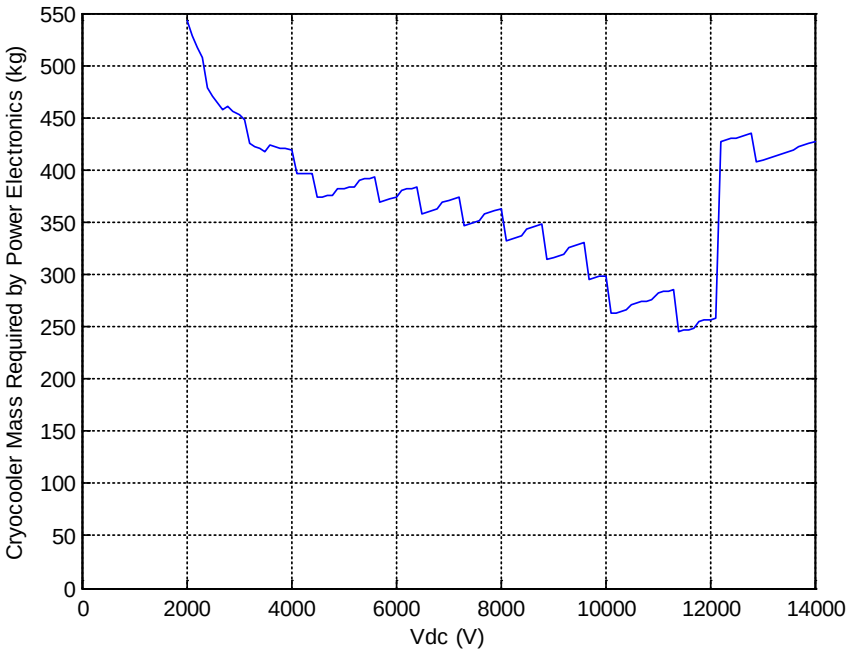


Figure 39.—Power Converter Losses (for 100 MW) vs. DC Link Voltage

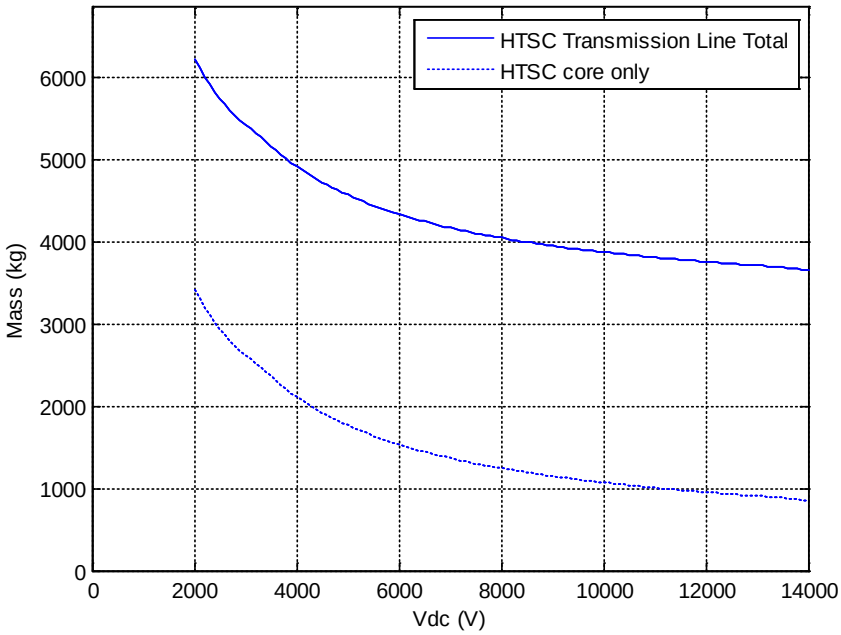


Figure 40.—HTSC Core and Total Transmission Line Mass (700 m) vs. DC Link Voltage

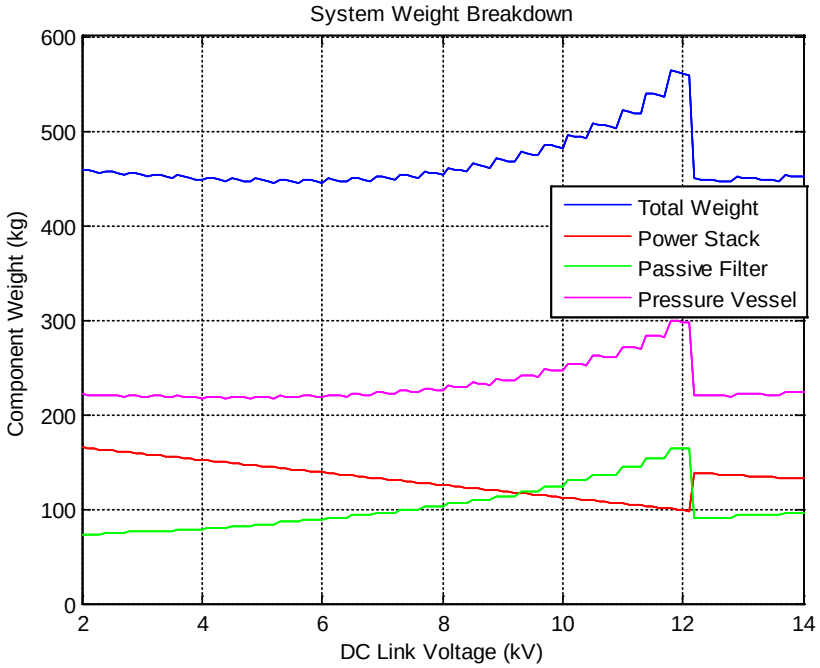


Figure 41.—Power Conversion System Mass Breakdown for 12.5 MW Generator Power Converter

The trends above both point to using the highest voltage allowed by the power electronic devices in order to reduce system mass. The only estimate that may contribute to a system weight minima is power conversion mass. Specifically, the mass of filter components increases as voltage increases because switching frequency is estimated to need to decrease to keep switching losses reasonable. Additionally, the mass of the packaging or containment increases as the filter volume increases with voltage. Both of these influences result in increasing mass as 12 kV is approached. The containment mass (shown in Figure 39 and Figure 41) is for a capsule pressure vessel allowing a ~650 psi cryogen system. Plots shown later will use this containment or packaging mass as the extreme heavy end and will also neglect the containment or packaging to indicate the extreme light end of the estimate to show trends if a lower pressure (1 atm for example) system were selected.

The reader is reminded that the 12 kV step change (shown in Figure 38, Figure 39, and Figure 41) is based on a projected IGBT voltage rating beyond which a 3-level converter topology is employed. It should also be noted that referenced transmission cable sizing (HTSC core and transfer line) is extrapolated at voltages above ~10 kV.

If transmission line length is long, this will dominate weight estimates. This study estimated 700 m of HTSC transmission cable, including s-shaped bends between major components, and further estimated the need for additional cryogen transfer lines (without HTSC cores) to supply other components with cryogen. Earlier studies had estimated total lengths of approximately 300 m of HTSC transmission line. Results for both lengths are considered to determine if length estimates, or equivalently mass per unit length, may influence voltage selection.

As previously stated, a Cryocooler mass scalar [3 kg/kW (input)] was provided by NASA for the purpose of converting power electronic efficiency (loss) to a mass. Figure 42 to Figure 44 show the impact of varying this assumption to determine its impact on the choice of DC bus voltage. This change in cryocooler mass scalar could equivalently be considered to show the trends of more or less efficient power conversion, or a higher temperature power conversion system that must not lift the heat as far.

For Figure 42 to Figure 44, the left plot does not include any packaging (pressure vessel) for the power converters. The right plot includes an estimate for the pressure vessel packaging of the power converter, which is required if the high pressure supercritical coolant system is assumed. The left and right plots can be compared to consider the impact of a high pressure system versus a lower pressure system.

The relative value of the transmission and power conversion weight represent the full system (50 MW generation and 50 MW fan motor loads).

Figure 43 assumes a heavier cryocooler (0.5 kW/kg), which increases the impact of power converter loss, thus the shape of Figure 39 is clearly visible in the figures above.

In Figure 44, the impact of power converter losses is minimized with the assumption of a very power dense [0.3 kg / kW (input)] cryocooler. In this plot, the shape of the power electronics mass and the transmission line mass trend is more visible than the shape of the power electronics efficiency trend.

In Figure 45, the cryocooler mass scalar of 3 kg/kW (input) is again used; however, a 130 K cryogen is assumed, which results in less cryocooler input power to lift the heat.

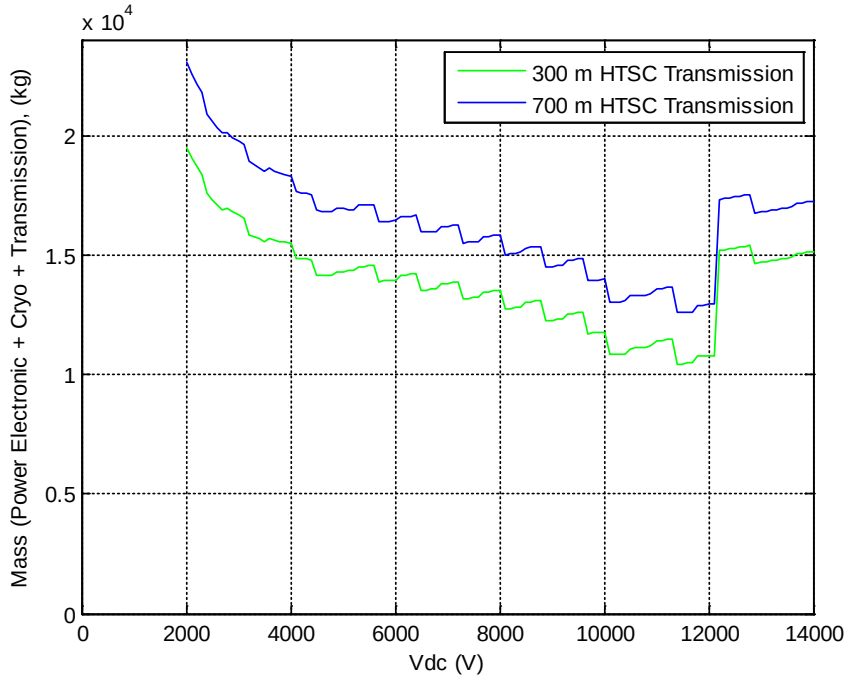


(a) Without Power Converter Containment

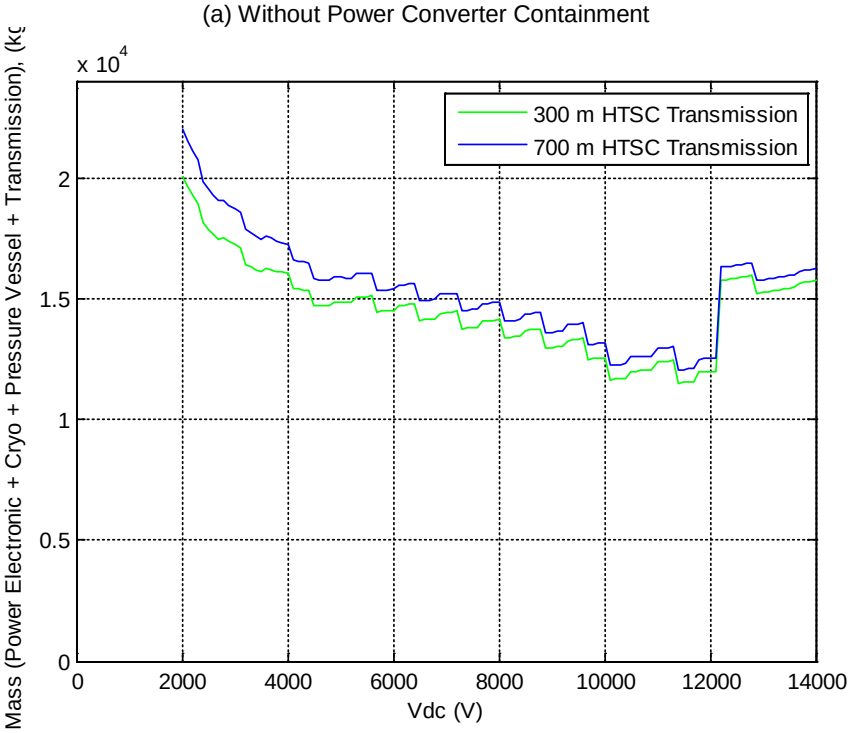


(b) With Power Converter Containment

Figure 42.—Power Conversion and Cryocooling and Transmission Line Mass vs. DC Link Voltage 3 kg/kW (input) Cryocooler scalar, 50 K cryogen, 300 K ambient

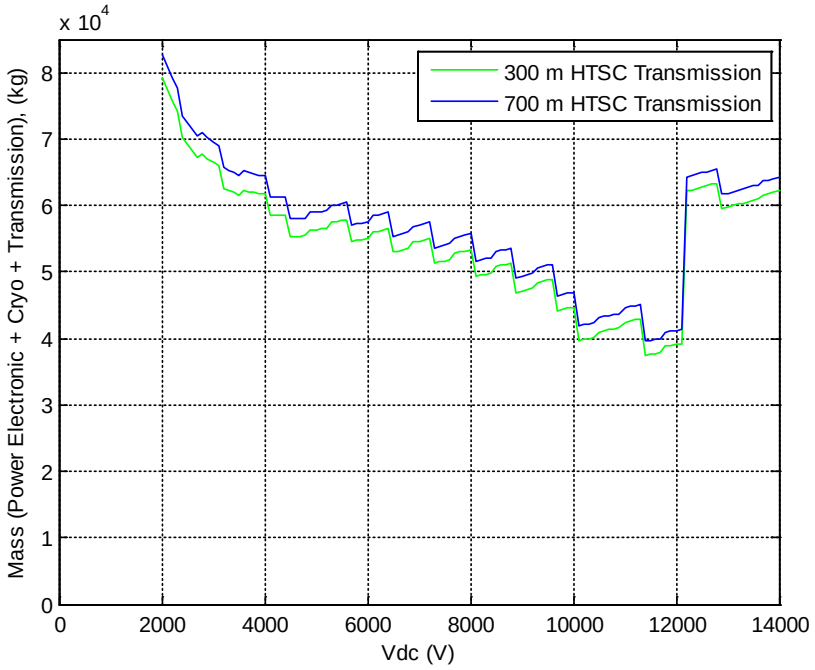


(a) Without Power Converter Containment

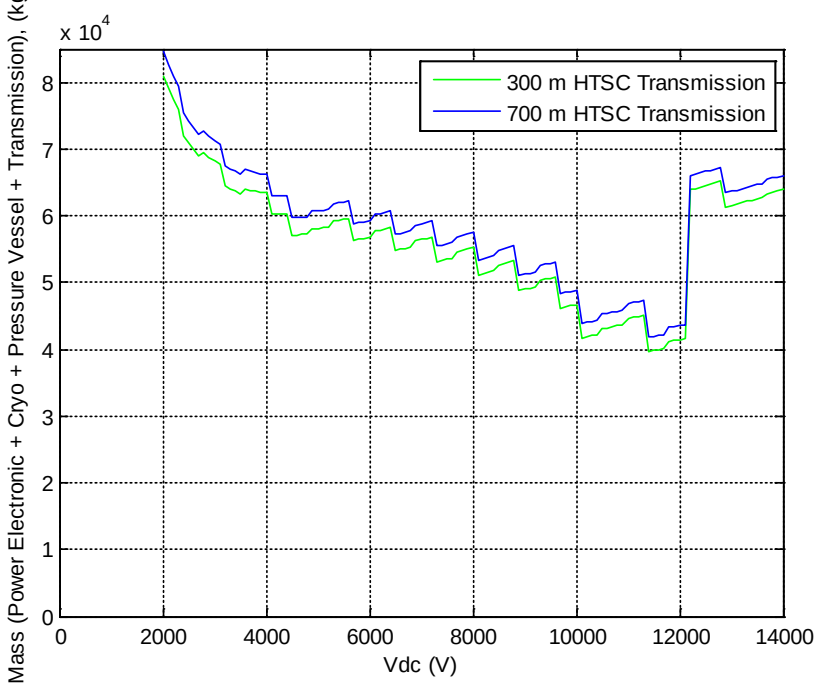


(b) With Power Converter Containment

Figure 43.—Power Conversion and Cryocooling and Transmission Line Mass vs. DC Link Voltage 15 kg/kW (input) Cryocooler scalar, 50 K cryogen, 300 K ambient

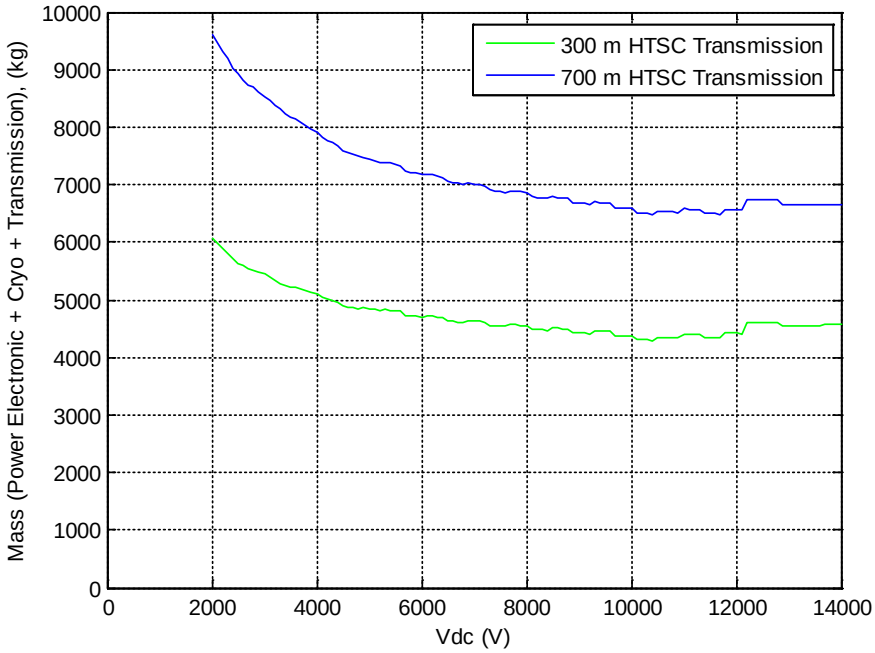


(a) Without Power Converter Containment

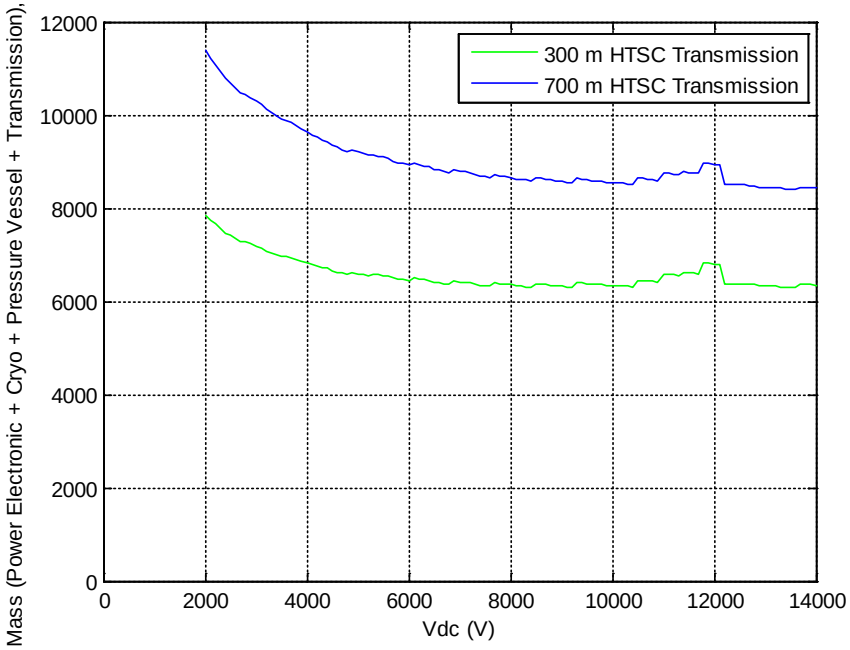


(b) With Power Converter Containment

Figure 44.—Power Conversion and Cryocooling and Transmission Line Mass vs. DC Link Voltage 0.3 kg/kW (input) Cryocooler scalar, 50 K cryogen, 300 K ambient

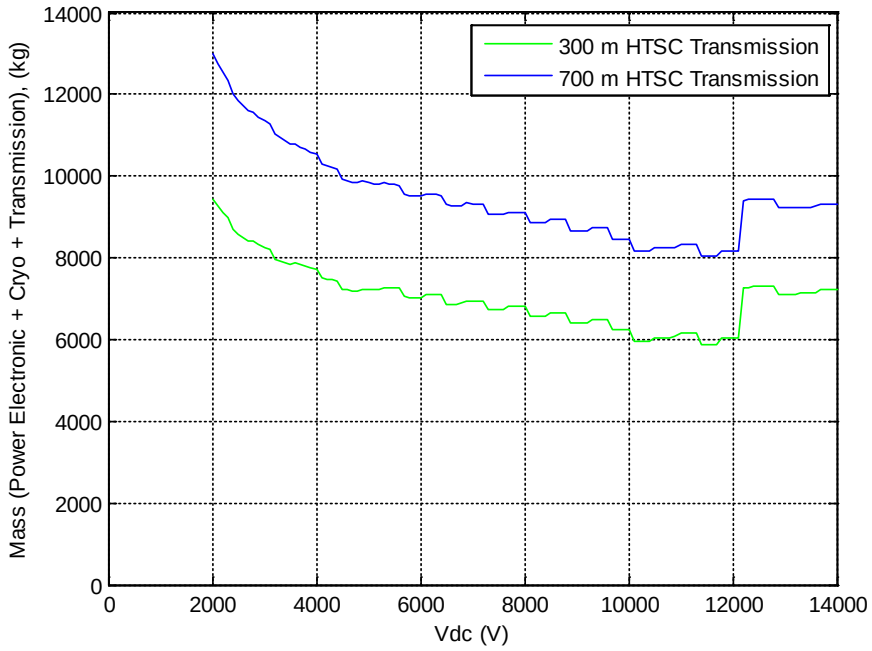


(a) Without Power Converter Containment

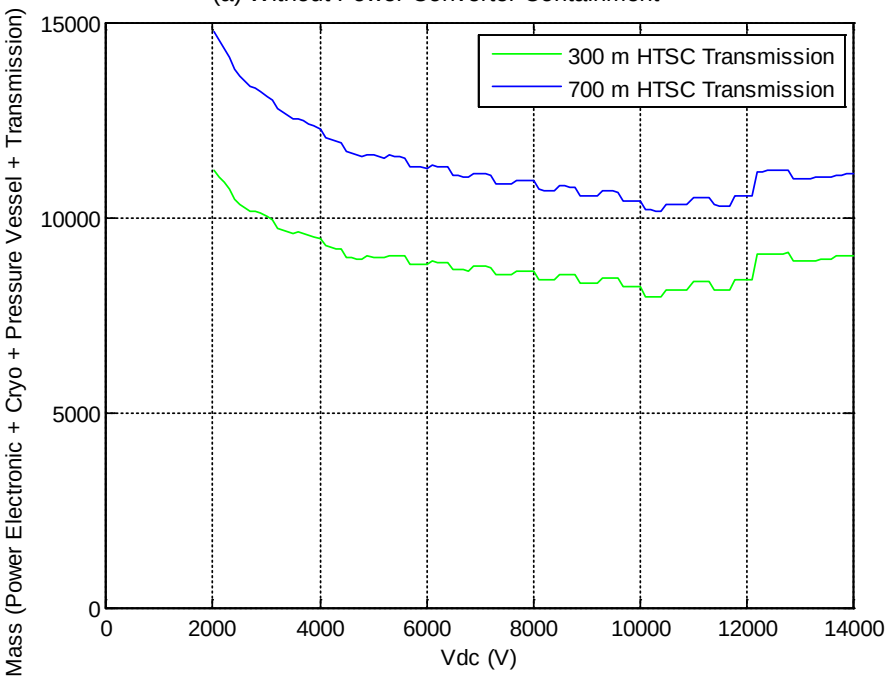


(b) With Power Converter Containment

Figure 45.—Power Conversion and Cryocooling and Transmission Line Mass vs. DC Link Voltage 3 kg/kW (input) Cryocooler scalar, 130 K cryogen, 300 K ambient

The summary plots above represent a broad range of density scalars. Though the absolute value and the existence of a minimum vary, all cases show the greatest decrease in the component mass with increasing voltage occurs by approximately 6 kV. For the architecture selected, and the assumptions made in the last milestone, a minimum occurs at about 8 to 10 kV. For cases where cable mass and cryocooler mass dominate, the minimum mass is achieved at the highest voltage achievable without the need to parallel two devices in a switching unit (12 kV in this study). Though the cases with higher cryocooler power density may indicate a lower system mass with adoption of a 3-level power converter, it should be noted that this system mass is similar to the minima at a lower voltage with a 2-level power converter.

Given the wide range of estimates in length and power densities, a voltage of over 6 kV would capture much of the weight reduction; a minimum may occur between 6 kV and 10 to 12 kV.

# 8.0 Final System Weight Estimate

The final system mass roll-up was completed for an 8 kV system voltage. A high pressure (650 psi) cryogen system is specifically assumed in the component masses of all components, except electric machines, which simply reference mass scalars from earlier studies. The high pressure cryogen assumption adds a pressure vessel mass to those components.

Figure 46 shows the evolution of the system mass estimate from the beginning of the study in the far left column to the final system estimate in the right two columns. Table 14 shows the estimates associated with the plot, and proves explanation for the weight growth. The largest weight growth is the transmission and distribution estimate, which now includes transfer line cryogen mass in the center column. The right-most column includes only the HTSC core in the transmission and distribution estimate; however, the length of HTSC increased greatly partly due to bend radius assumptions. Power conversion mass increased due to a change in motor power rating and due to inclusion of a pressure vessel for the high pressure cryogen. In review of the figures, one can conclude that the design of the superconducting transfer lines and the layout of the architecture will be important to minimize system weight. Future systems may or may not operate at high pressure, but inclusion of some packaging mass suitable for structure or pressure is recommended. As was shown in the previous section, even with large variation in the assumptions included in this weight roll-up, a narrowed system voltage range could be projected.

A summary of the impact of a two cryogen system is provided in the following Table 15 and Table 16. Since the majority of the electrical losses are generated by the power electronics which do not need to operate at temperatures as low as the superconductors, using a higher temperature cryogen may result in less cryocooler power and weight. Numerous system developments and details would be required for transitions between the two-temperature system, but the impact of the difference in required power to lift power conversion losses from lower temperatures could be a significant impact to system efficiency.

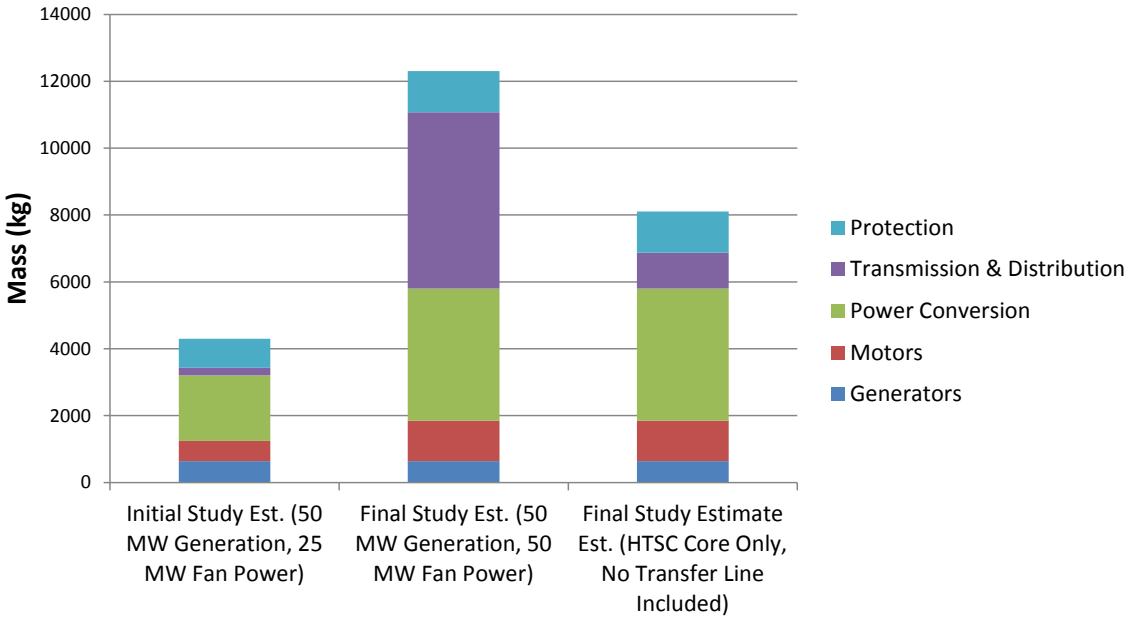


Figure 46.—Development of System Mass Estimates

TABLE 14.—COMPONENT MASS SUMMARY

| Components | T&D subtotals (kg) | Final estimate | | Initial estimate | | Mass delta (kg) | Reason for delta |
|---|---|---|---|---|---|---|---|
| | | Mass (kg) | System % | Mass (kg) | System % | | |
| Generators | | 636.9 | 5% | 636.9 | 15% | 0.0 | |
| Motors | | 1213.2 | 10% | 606.6 | 14% | 606.6 | Due to increase in rating: Fan motor and generating power should be equal |
| Power conversion | | 3950.5 | 32% | 1960 | 46% | 718.6 | Due to inclusion of pressure packaging and increase in rating: Fan motor and generating power should be equal |
| Transmission and distribution | 5269.8 | 5269.8 | 43% | | | | |
| Ne System | | | | | | | |
| HTSC | 1069.8 | | | 226.8 | 5% | 5043.0 | Inclusion of transfer line estimate and increase in length ~330 m to 1100 m |
| Transfer line | 3477.0 | | | | | | |
| Ne cryogen | 209.7 | | | | | | |
| $N_2$ System | | | | | | | |
| Transfer line | 432.4 | | | | | | |
| $N_2$ cryogen | 80.8 | | | | | | |
| Protection | | 1236.8 | 10% | 867 | 20% | 369.8 | Due to fan motor rating increase and refinement of estimate |
| | Total | 12307 | | 4297 | | 8010 | |

TABLE 15.—CRYOCOOLER POWER AND MASS ESTIMATE—TWO SEPARATE CRYO SYSTEMS REJECTING HEAT TO AMBIENT

| | | | Ambient temperature 300 K | | | | | | | |
|---|---|---|---|---|---|---|---|---|---|---|
| | | | Supercritical Ne System | | | | Supercritical N2 System | | | |
| | | | System temperature | 50 K | | | System temperature | 130 K | | |
| | | | Carnot COP | 5.0 | | | Carnot COP | 1.31 | | |
| | | | % of Carnot | 30% | | | % of Carnot | 30% | | |
| | | | Ne cooling scalar | 16.7 | | | N2 cooling scalar | 4.4 | | |
| | | | Cryocooler density | 3 kg/kW (input) | | | Cryocooler density | 3 kg/kW (input) | | |
| | | | Supercritical Ne System | | | | Supercritical N2 System | | | |
| Loss estimate | Electrical losses | | Heat leak and pumping SC Ne | | Cooling system input power | | Heat leak and pumping SC LN2 | | Cooling system input power | |
| | kW | % of System | kW | % of System | kW | % of System | kW | % of System | kW | % of System |
| Generators | 12.55 | 5.7% | - | | 209.19 | | - | | - | |
| Motors | 25.00 | 11.4% | - | | 416.67 | | - | | - | |
| Power conversion | 180.78 | 82.8% | - | | - | | - | | 788.0 | |
| Transmission | 0.00 | 0.0% | 2.76 | | 46.07 | | 6.54 | | 28.5 | |
| Protection | 0.07 | 0.0% | - | | 1.23 | | - | | - | |
| Totals | 218.40 | 100% | | | 673.16 | | | | 816.53 | |
| Total system losses | | 1708 kW | | | 2019.5 kg | | | | 2449.6 kg | |
| Total system efficiency | | 96.584% | | | | | | | | |
| Cryocooler mass | | 4469.1 kg | | | | | | | | |

TABLE 16.—CRYOCOOLER POWER AND MASS ESTIMATE—SINGLE CRYOGEN SYSTEM—TEMPERATURE SET BY SUPERCONDUCTOR

| | | | | | | |
|---|---|---|---|---|---|---|
| | | | Ambient temperature 300 K | | | |
| | | | Cryogen | | | |
| | | | System temperature | 50 K | | |
| | | | Carnot COP | 5.0 | | |
| | | | % of Carnot | 30% | | |
| | | | Ne cooling scalar | 16.7 | | |
| | | | Cryocooler density | 3 kg/kW (input) | | |
| | | | Cryogen | | | |
| Loss estimate | Electrical losses | | Heat leak and pumping | | Cooling system input power | |
| | kW | % of system | kW | % of system | kW | % of system |
| Generators | 12.55 | 5.7% | - | | 209.2 | |
| Motors | 25.00 | 11.4% | - | | 416.7 | |
| Power conversion | 180.78 | 82.8% | - | | 3013.0 | |
| Transmission | 0.00 | 0.0% | 5.00 | | 83.3 | |
| Protection | 0.07 | 0.0% | - | | 1.2 | |
| Ne System losses to $N_2$ System | | | | | - | |
| Totals | 218.40 | 100% | | | 3723.40 | |
| Total system losses | 3942 kW | | | | 11170.2 kg | |
| Total system efficiency | 92.116% | | | | | |
| Cryocooler mass | 11170.2 kg | | | | | |

# 9.0 Dynamic Model and Example Case Runs

The modeling approach selected is based on Reference 45 and has been used for modeling DC power systems on aircraft. Large system models with detailed physics-based component models present the system modeler with the challenge of identifying many component parameters and typically result in small time constant dynamics requiring long model run times. This approach uses simplified, non-physics based, dynamics models. This is useful for the initial phases of system development, allowing the modeler to include component models that represent the dynamic performance of components while minimizing small time constant dynamics. Additionally, such models allow the system-level models to be created utilizing component models that only require top-level performance and can typically be included in some non-proprietary form.

## 9.1 Model Overview

The model assembled for this program is shown in three figures below as a roadmap to the Matlab/Simulink model file deliverable. Figure 47 shows the top level of the model; Figure 48 labels the major components; and Figure 49 labels the right, center, and left buses.

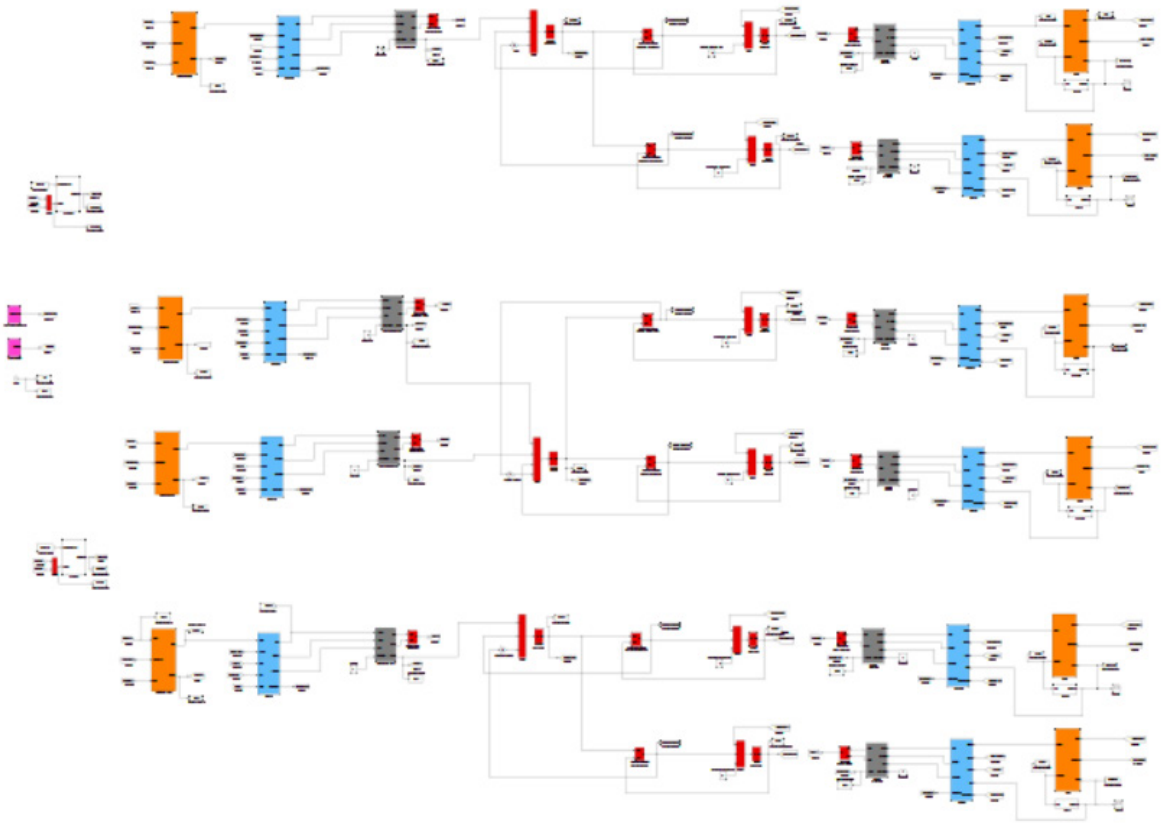

Figure 47.—Baseline System Model in Matlab/Simulink

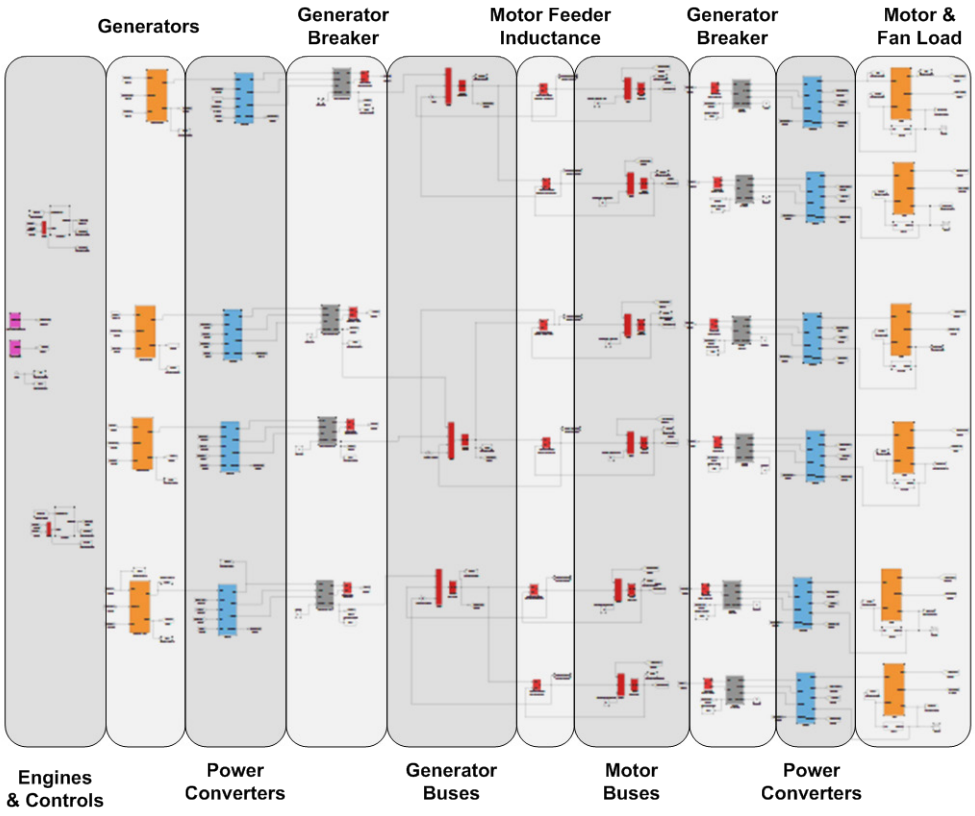


Figure 48.—Baseline System Model with Major Component Labeled

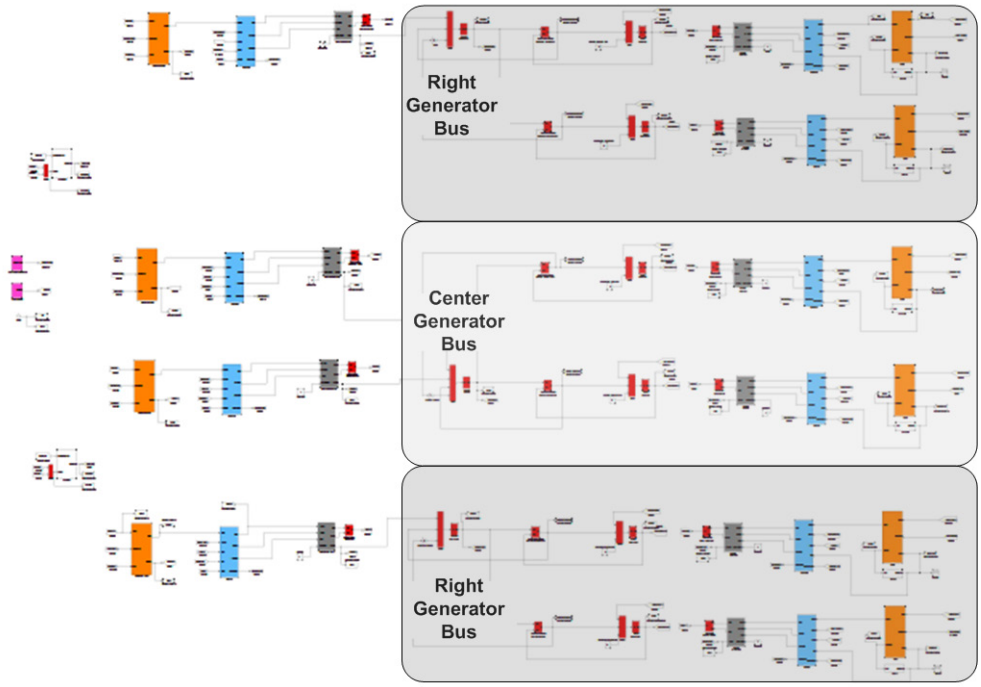


Figure 49.—Baseline System Model with Generator Bus Systems Labeled

The component naming convention follows that shown in Figure 3 of the architecture definition.

The three generator buses are modeled. Connected to each generator bus are two motor feeders. The current from one of these two motor feeders is multiplied by one minus the total number of model feeders connected to the bus. This allows the model to be used for single motor feeder disconnects or faults without duplicating every motor feeder. Modeling every motor feeder with its associated components would result in longer model fun times and would not change the results, as each motor feeder is identical with identical parameters.

The baseline deliverable model allows investigation of nominal controls and bus stability. All breakers are modeled only as ideal switches; none of the energy dissipating circuitry of the hybrid breakers is included. This does not impact the longer time constant dynamics associated with system controls through fault cases; however, for fault cases it results in large voltage spikes due to forcing a near-instant change in current. For cases where fault voltage is the focus of the study, additional models were provided where only the relevant breakers were replaced with breaker models including the function of the energy dissipating circuitry. This can result in significantly longer model run times due to the addition of model states and smaller time constants. As indication of the model's usefulness, its exercise for fault cases indicated an additional component, a resistor for transient damping, be added to the hybrid circuit breaker concept. The need for the component was made obvious when one considers system operation with multiple series hybrid breakers.

## 9.2 Component Models

Component model parameters were selected based on estimates used throughout the study effort. These are summarized below, and are provided with full detail and comments in the model initialization file provided as a deliverable.

### 9.2.1 Generator

The main elements of the DC generator unit model are a controlled current source feeding into a capacitor with proportional integral feedback to control the capacitor voltage as shown in Figure 50. The proportional integral control regulates the generator output voltage to the set point value. The values $G_{pgen}$, $G_{igen}$, and $C_{gen}$ can be determined from the generator and power converters' step response, which is characterized by the size of the step load, the peak of the voltage transient, and the time constants of the step response as described in (Ref. 45).

### 9.2.2 Power Converter

Reference 45 represents elements of the power converter EMI filter inductance and capacitance parameters shown below. For this power system, the estimated EMI filter capacitance sets the capacitance value, but the inductance will be dominated by the series inductance in the generator hybrid DC breaker, which sets the inductance value shown in Figure 51.

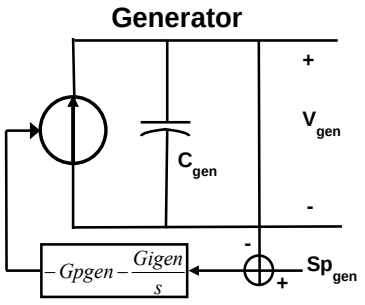


Figure 50.—Generator Model

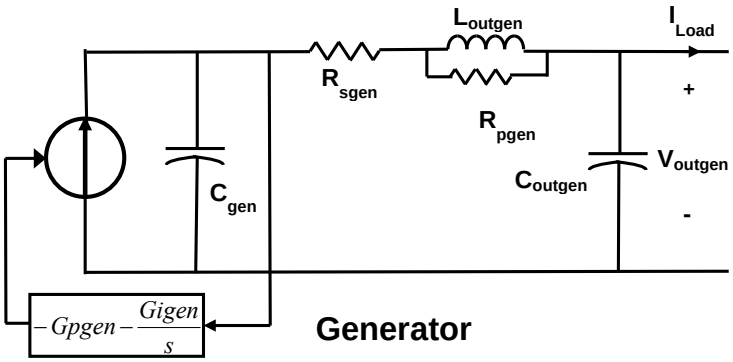


Figure 51.—Generator and Power Converter

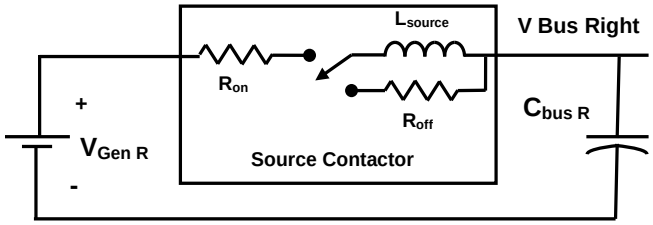


Figure 52.—Ideal Switch Breaker Representation

The modeling approach lumps generator and power converter performance with a DC output. As a result of this approach, on the hybrid DC breakers are modeled; no AC transmission between generator and power converter is modeled.

### 9.2.3 Generator Breaker

When modeling to develop system controls for power sharing, system reconfiguration, and other slower dynamics, the breakers can be modeled as ideal switches as shown in Figure 52. Opening the ideal switch under load will cause voltage spikes and ringing in the system, but generally for a short time.

When investigation voltage and current during fault operation is the objective, the specific breaker that will open can be replaced with the model shown in Figure 53. This models the ZnO or MOV function of the snubber circuit as a voltage (MOV Voltage), which drives current to zero, and then the switch is off.

### 9.2.4 Contactors

For the purposes of this system model, contactors were not modeled. As the system controls are further developed, contactors will need added.

### 9.2.5 Motor

The motor incorporates an inertia parameter. This is a per unit inertia in units of seconds, meaning that if rated power is drawn for the defined time in seconds from an initial rated speed, the speed at the end of that time will be zero.

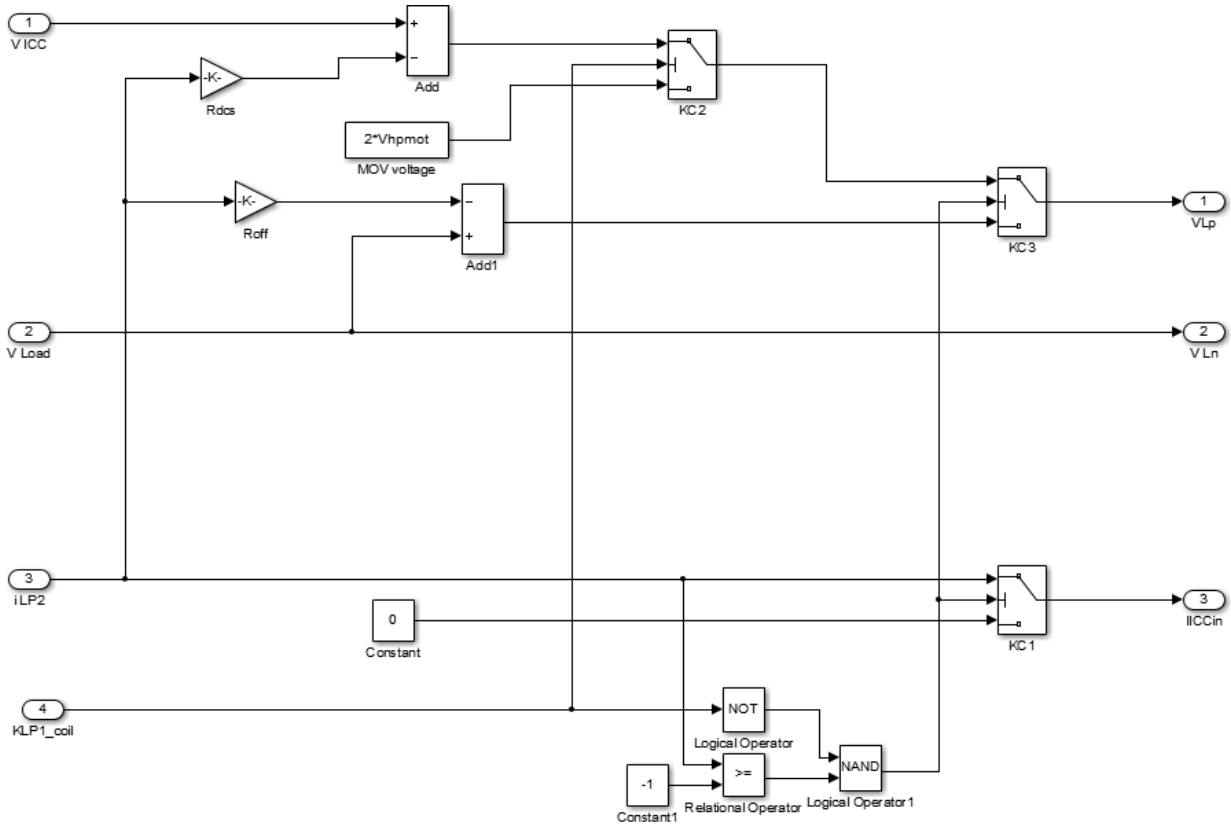


Figure 53.—Hybrid Breaker Snubber Model

### 9.2.6 Fan

The propulsive fans are modeled as simple cubic load as shown below.

$$P_{load} = a * speed^3$$

The constant "a" is selected based on a fan speed and fan load. For the default model, "a" is calculated so that rated power of 3.57 MW is reached at 3500 rpm.

### 9.2.7 Bus Voltage Controls

The power converter controls and modeled generator response establish the bus voltage. The voltage reference is set as the nominal voltage of 8 kV, with a voltage droop offset which is used for power sharing between generators. The voltage droop was selected as 50 V over the full power range. For a system with an 8 kV nominal voltage this is only 0.5 percent droop over the full power range. If it is determined that system disturbances cause significant variation in this range, the percentage droop could be increased so system disturbances have less control impact.

### 9.2.8 Gas Turbine Engine

The turboshaft gas turbine engine is modeled as a second order underdamped response, using the same approach as for the generator model. For the purpose of this simulation, a full rated power step results in a speed droop of 20 percent and recovery to rated speed in 5 sec.

### 9.2.9 System Power Controls

System power is controlled by commanding fan speed. All other system components and controls respond to this control command, which requires increased motor current, which requires increasing current from the generators, and ultimately requires more torque from the engines.

## 9.3 Example Cases

### 9.3.1 Nominal Operation with Thrust Transient

The figures below show an example case of an increase in system power from a low fan speed to near rated conditions. The plots below are from the plotting scripts delivered with the model.

Figure 54 shows the fan load increasing with fan speed. The fan speed command was a ramp to a constant. All modeled fans are plotted in the windows below. The single line indicates that all modeled fans have exactly the same speed and load versus time. All of the following plots also plot the noted parameter for all components, and a single line indicates all perform the same.

Figure 55 shows engine and fan powers. The total of all 14 motor powers are applied to four generators and then to two engines.

Figure 56 shows the increase in engine power output and engine speed droop as the load is applied. Engine speed is shown to droop during the rapid increase in system load and then begin to recover as the increase in fan load slows. Engine response will be a combination of engine capability and controls.

Figure 57 shows the bus voltage decreasing with increasing power as defined by the droop control, which allows power sharing between generators. The excursion at time zero is a model initialization artifact.

Figure 58 shows component efficiencies, and is primarily used as a check that losses are occurring in the system model and they are of the approximate magnitude expected. Efficiencies will change with load and during transients, and could later be used to estimate the cooling capacity needed during faults where losses will be slightly higher. For cases where even small oscillations occur in the system, efficiency may be calculated to be higher than 100 percent for part of an oscillation.

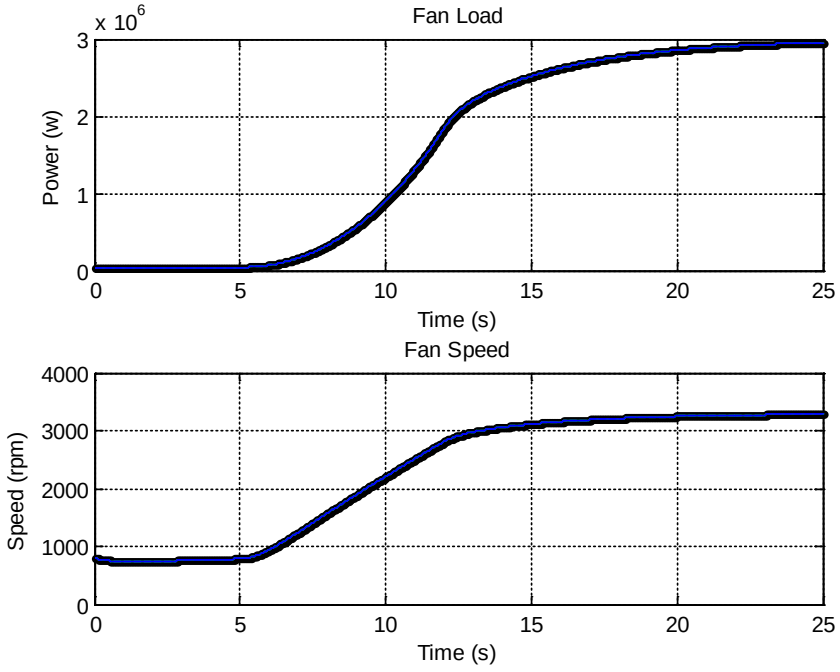


Figure 54.—Fan Load and Fan Speed

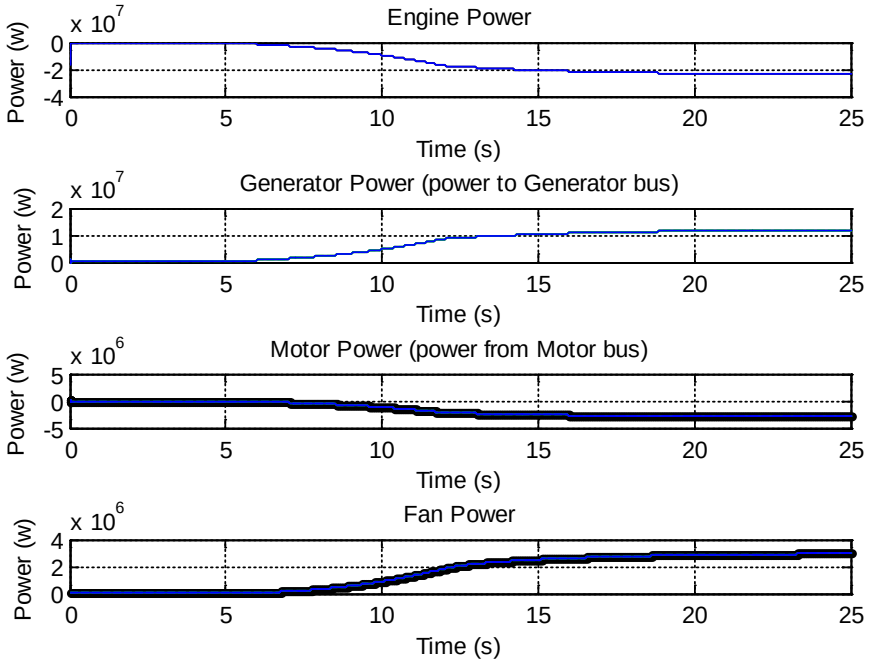


Figure 55.—Component Powers

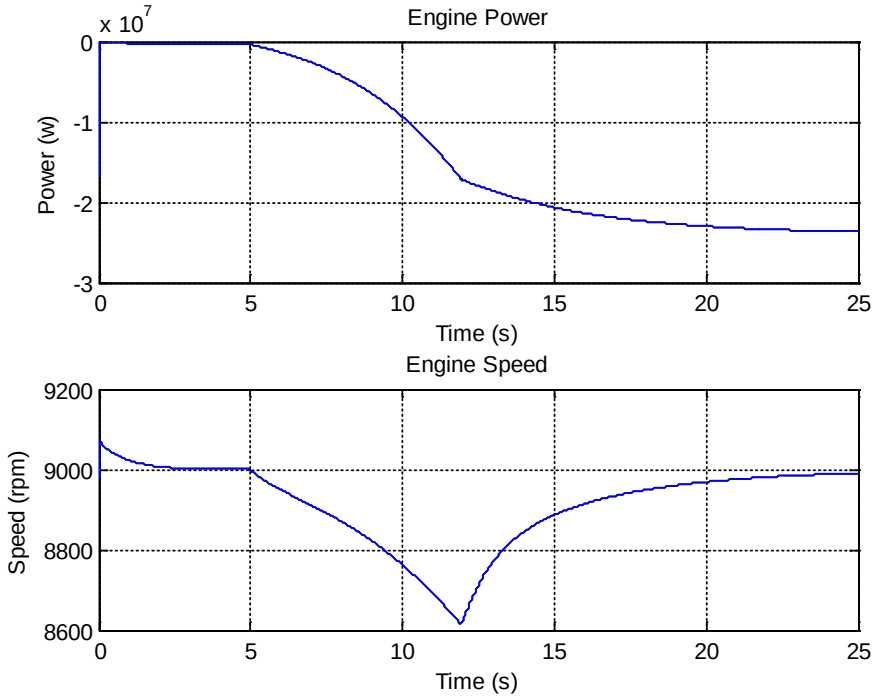


Figure 56.—Engine Power and Turbine Speed

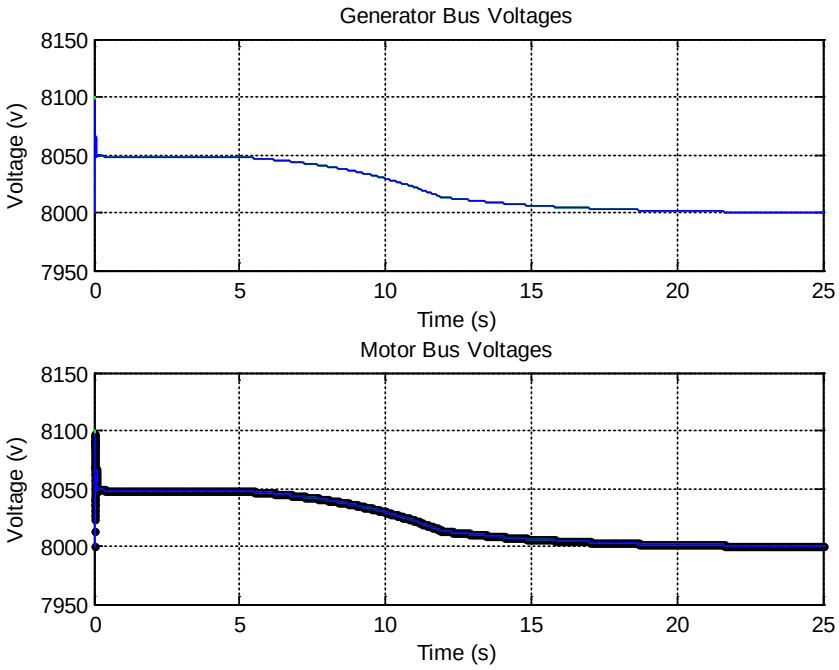


Figure 57.—Generator and Motor Bus Voltages

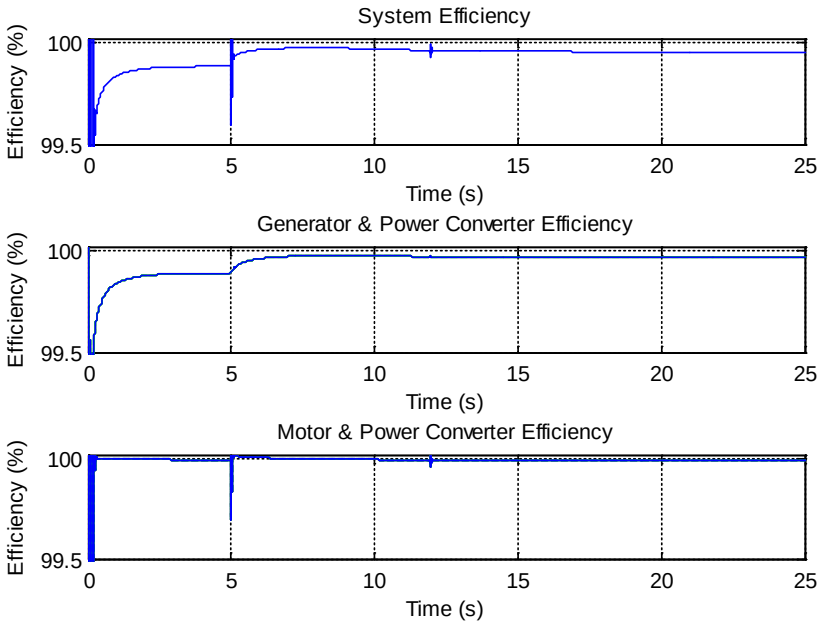


Figure 58.—System Efficiencies

In addition to the system model deliverable, a model of the hybrid breaker was created using Matlab/Simulink SimPower components. This model allowed the confirmation of estimated hybrid breaker performance, but runs more slowly than elements in the larger system model. In keeping with the philosophy of the system model, the performance of the hybrid breaker was modeled.

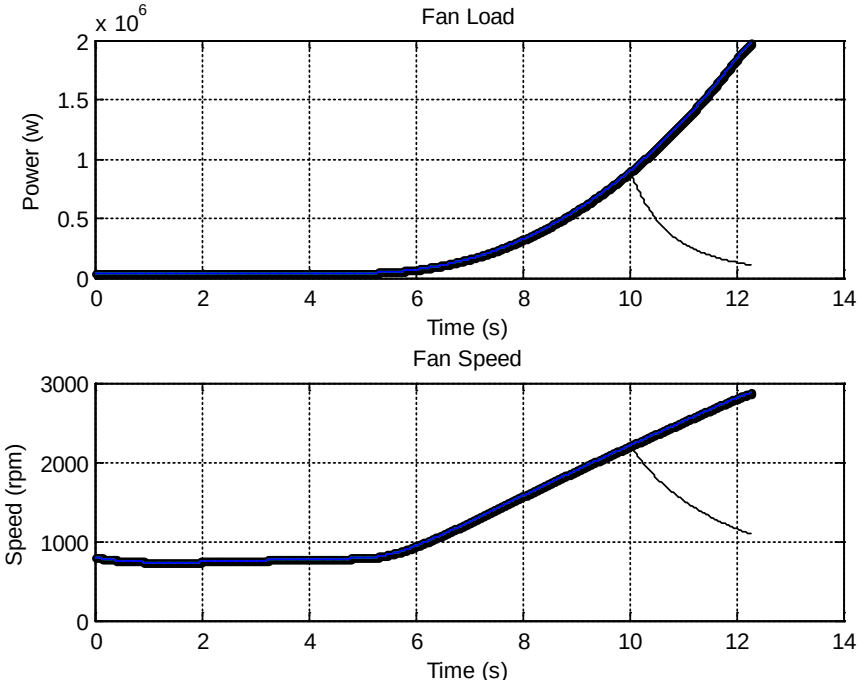


Figure 59.—Fan Load and Speeds for a Breaker Opening on a Single Motor

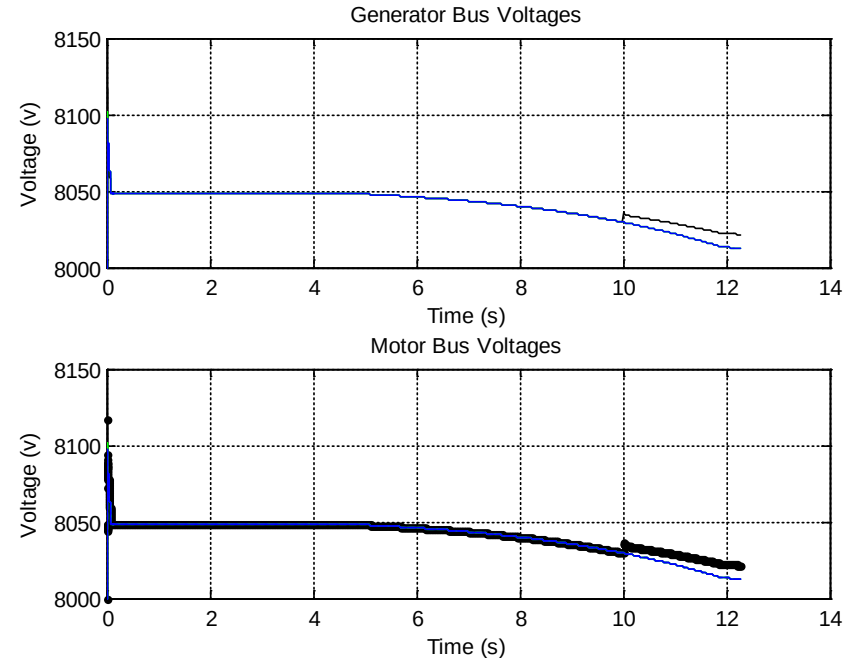


Figure 60.—Motor and Generator Bus Voltages for a Single Motor Open

### 9.3.2 Motor Breaker Open

This case models opening of a motor breaker under load, but not as a result of an electrical fault. Such operation could occur if an impending failure is detected and requires the motor bus be immediately disconnected from the rest of the system. The breaker must interrupt current, but not fault level currents.

Figure 59 shows a commanded ramp increase in fan speed and fan load with all fans moving together until time = 10 s when the motor breaker is opened. At this point, the driving torque to one fan is reduced

to zero and this fan (the thin black line) slows relative to the others (thick blue line). Figure 60 shows the motor and generator bus voltages when the breaker opens at time = 10 s. It can be seen that no large voltage excursions or ringing occurs. As the load drops for one of the generator buses, the droop control adjusts the voltage a higher set point.

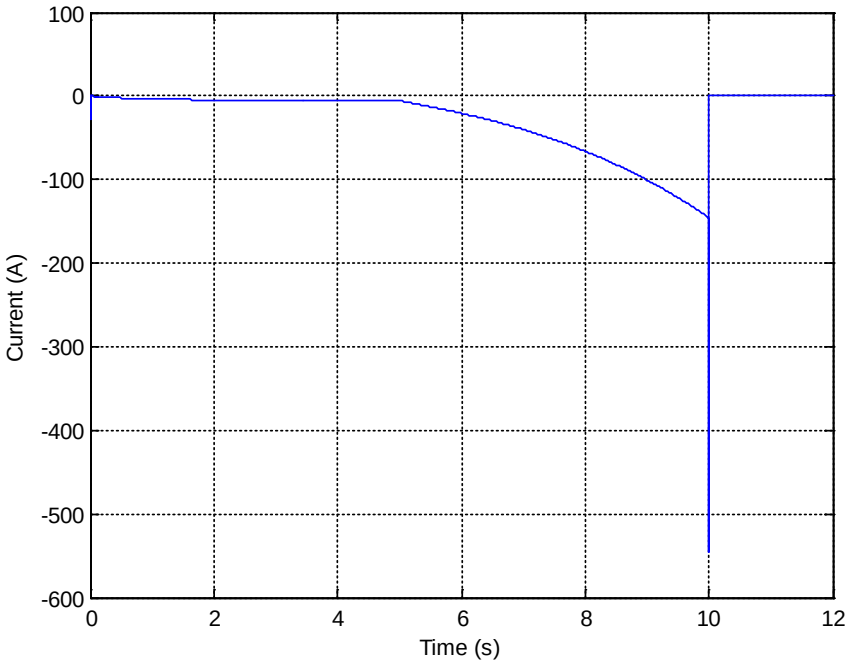


Figure 61.—Motor Bus Current During Fault (t = 10 s) and Breaker Open

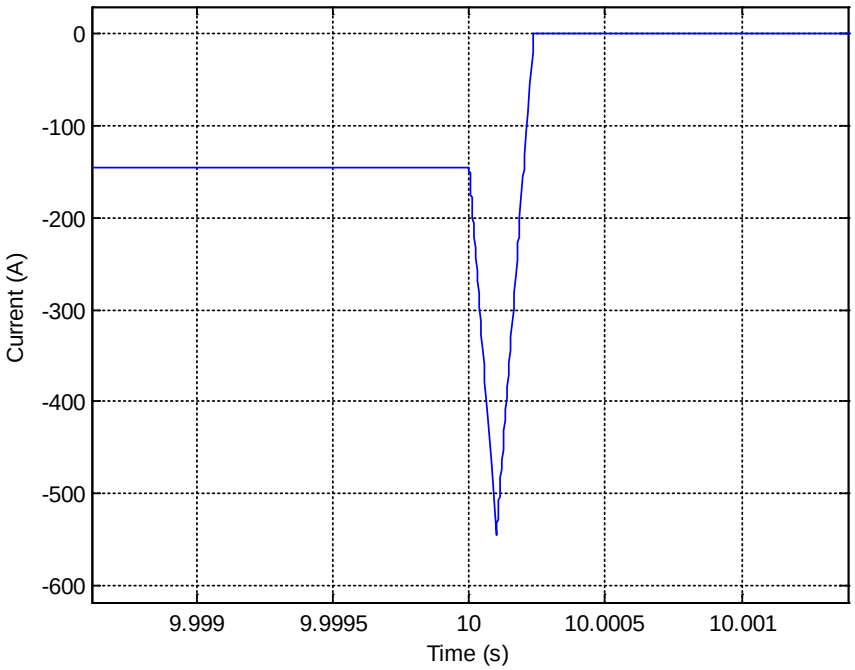


Figure 62.—Hybrid Breaker Operation After Fault at t = 10 s

### 9.3.3 Motor Fault and Breaker Open

Figure 61 shows current at the motor bus, and a current spike can be seen at time = 10 s when the fault occurs. On a smaller time scale, Figure 62 shows the fault current rise and the hybrid breaker driving current to zero.

Finally, Figure 63 shows that all of this occurs with no large voltage disturbances at the generator bus.

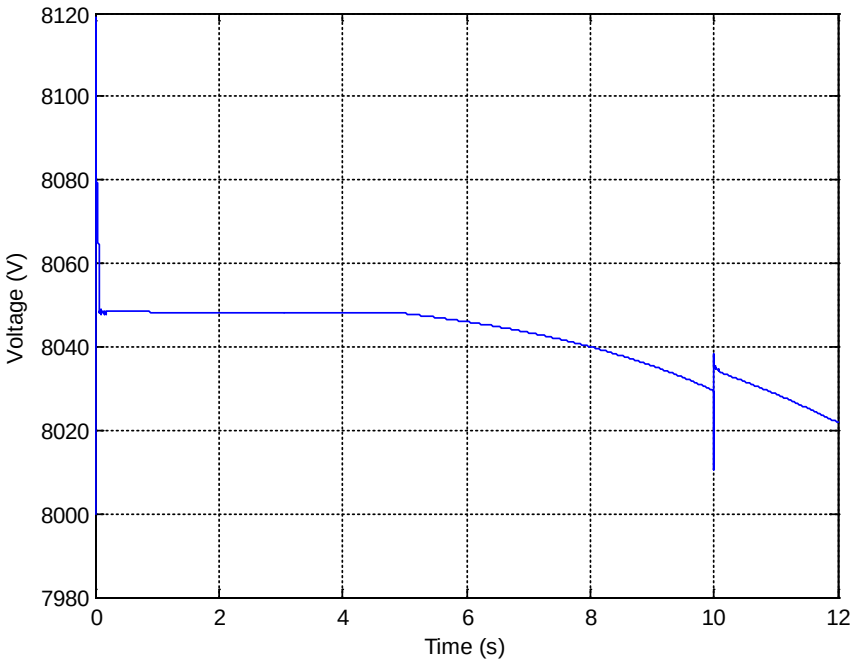


Figure 63.—Generator Bus Voltage During Motor Fault and Breaker Open

# 10.0 Standards Recommendation

A good standard should be simple and of limited size, focus on the requirements formulated based on collective experience and consensus, utilize all relevant existing standards, and leave room for future improvements.

However, medium-voltage DC power systems are still not a mature technology and will require continued research activities. Although there are some IEEE Power Electronics Standards for Ships in which a MVDC power system is discussed, those standards themselves are not finalized and cannot be applied directly to the MVDC system under study, which is targeted for aerospace propulsion application and involves the use of cryogenic electrical high power equipment. Existing standards from the marine space are discussed in References 46 and 47. The marine space provides perhaps the closest analog, though it is clear that the weight sensitivity of flight will drive a different system than the marine space.

Based on the analysis of the aerospace propulsion system performed so far in this program and other previous work on MVDC systems, the following contents are recommended to be included in the future standard for MVDC power systems on aerospace propulsion systems with cryogenic electrical high-power equipment. Note that the sequence does not correspond with importance.

1. *MVDC Power Ratings:* The common ratings of MVDC power systems, including their operating devices and auxiliary equipment, should be selected from the following:
   a. Rated voltage or different voltage class, which is the most important parameter of the system and can determine the selection and the design of the system key components, such as power converters, motors, cables, and generators
   b. Voltage tolerance or the voltage variation range during normal operation
   c. Rated withstand voltage, which includes the maximum voltage during short pulse or lightning
   d. Rated continuous current, which determines the current rating of superconductor cables
   e. Rated withstand current, which includes the maximum system current for short pulse, such as during system grounding fault

2. *Grounding Method:* The system components that are connected to the MVDC network, such as motor, generators, connectors, and power electronics converter, all need to be grounded. If not, the system will not have a voltage reference point and any leakage current could cause DC system voltage unbalance.

   The grounding scheme can significantly impact the system performance, both in normal operating conditions and during faults. In general, solid grounding or low impedance grounding can introduce high leakage current during normal operation and high in-rush current, but can also limit system voltage; while high impedance grounding or a floating system can limit the system current, but can increase the system isolation requirement, especially during grounding faults.

   In the standard, certain basic requirements of the system grounding method should be included. For example, the leakage current through the grounding network should be lower than a certain level.

3. *Galvanic Isolation:* To limit the impact of a single system fault, the whole system should be separated into several sections. Galvanic isolation should be provided between such sections, either in normal operations or at least during faults. However, galvanic isolation will also increase system loss, weight, volume, and cost.

   In the standard, certain performance related to galvanic isolation should be addressed. For example, the minimum power rating of a system component or a system section should be identified, above which a galvanic isolation between the component and the whole system should be provided.

4. *System Stability:* The MVDC system will involve many subsystems, and such subsystems need to be developed and tested separately before being assembled together. To guarantee a reliable system operation, the system stability requirements need to be included in the standard.

   In the standard, a well-accepted method to describe the stability performance should be defined first, followed by the test methods. The minimum requirement of such performance, according to different operating conditions, should also be described clearly.

5. *Efficiency:* The electrical efficiency of the system depends on the mission of the aircraft and service conditions. MVDC power systems are expected to be efficient to meet economic constraints, especially with the use of cryogenic electrical high power equipment. Therefore, it is critical to achieve high efficiency under a range of operating conditions representative of anticipated uses. However, the use of cryogenic component also brings significant challenge into the cooling system, since the cooling efficiency is much lower for a cryogenic system compared with a system running in normal temperature. Thus, the system loss may bring more penalties for a cryogenic system in terms of the increased weight and cost of the cooling system.

   In the standard, the lowest efficiency for each system component, such as the generator, motor, power converter, and cable, should be specified under different conditions, such as different load levels. The impact of the load variation slope should also be considered, since AC components can generate much more heat in a superconductor than DC. The related test methods for the efficiency number should also be included.

6. *Quality of Service:* QoS is a metric of how reliably the power system provides power to the loads. An example of a QoS metric is the Mean-Time-Between-Service-Interruption (MTBSI). QoS does take into account equipment failures and normal system operation transients. Higher QoS is desirable. However, it usually means higher system cost.

   In the standard, the minimum QoS, such as the minimum MTBSI, should be identified for different types of loads, e.g., the critical loads and non-critical loads.

7. *Survivability:* For aircraft application, system survivability is critical. Thus, in the standard the following topics should be addressed:
   a. Fault ride-through capability. The system should be able to continue operating without being impacted by system faults. The system faults should be defined, as well as the severities. Good examples include the single component failure, the system voltage drop or rise due to other system faults and system single-point grounding fault.
   b. System redundancy. To handle the failure of certain critical components, such as the generator, power converter, and motor, the system design may consider involving system redundancy. The system redundancy may mean additional system components, such as one more generator, or over rating the existing system components, or both.
   c. System derated operation. Under certain extreme cases, or to keep the economic benefits, the system should continue operating under a derated condition. The derated power should meet the predefined system minimum requirements.

8. *Power Quality:* In a DC distribution system, the fundamental frequency is zero and the concept of harmonic distortion in an AC system does not apply. However, the impact of the ripple voltage and current still exist. For the DC system, the power quality can be described by the amplitude of the ripple component, e.g., the maximum non-repetitive peak, the maximum repetitive peak, and the maximum repetitive peak-to-peak. Since in the cryogenic system the power loss in the

superconductors could be dominant by the AC or ripple currents, it is very important to cover power quality in the standard.

9. *Operation of a Cryogenic System:* Compared with a normal MVDC system, this system will involve the operation of a cryogenic system to enable the operation of a superconductive motor and generator. This special subsystem needs additional attention. In addition to providing cooling, the cryogenic system, at pressures above ambient, may be responsible for providing electrical insulation of the high voltage system.

   In the standard, the performance and operation of the cryogenic system should be specified, e.g., the controlled temperature variation range, reliability, and the minimum cooling capability.

10. *Power Management:* Power management shall fulfill the following functions: manage power under normal conditions, maintain QoS, and maximize survivability.

    Under normal operating conditions, power management must provide for on average balance of the energy used by loads and the energy produced by generation. In addition, power management also should include dynamic balancing associated with load sharing among generators.

    Under the conditions where the power system cannot serve all loads due to damage or equipment failure, power management is required to implement a survivability response.

11. *Others:* In the standard, some other specific topics could also be addressed or reference other standards, e.g., the system EMI performance, system DC breaker performance, MVDC insulation techniques at altitude.

    In addition to standards, there will be various certification requirements that will need to be developed with the appropriate governing bodies, such as the Federal Aviation Administration (FAA).

# 11.0 Conclusions and Recommendations

## 11.1 Conclusions and Observations

Through investigation of several potential architectures, estimates of component weights as a function of voltage, comparison of electromechanical and solid-state circuit breakers, development of a dynamic system model, and investigation of relevant standards, the high-level conclusions and observations below were reached.

- A voltage source architecture was selected as the best option for reconfiguration, either for scalability or redundancy. Distinction between breakers (which can open under load conditions) and contactors (which are only opened or closed for unloaded cases) were made to reduce the system protection weight as contactors can be significantly lighter than breakers.
- Bus voltage in the 6 to 10 kV range was estimated to provide minimum system weight depending on assumptions for the forward-looking parameters. An optimum for the proposed architecture of approximately 8 to 10 kV was anticipated.
- Hybrid circuit breakers that use mechanical contacts for low loss current carrying, and solid-state components for absorption of interruption energies, were proposed and are estimated to provide an improved power density over mechanical breakers and improved efficiency over solid-state breakers.
- This range of bus voltages assumes all electrical components are in a pressurized environment to prevent breakdown of air at ambient pressures. The study further proposed the possibility of a highly pressurized system (up to ~700 psi) to allow supercritical cryogen. The potential benefit of supercritical cryogen is the absence of boiling of the cryogen and bubbles that concentrate electric fields. Such a system has the obvious drawback of requiring all component enclosures to withstand the cryogen pressure that contributes weight.
- Whether or not a high pressure cryogen is used, the construction of the cryogenic cables should be considered in weight and cooling system estimates. Existing cables with transfer line construction, including a flow path for the cryogen and a vacuum jacket for thermal isolation, add significantly to the mass of a superconductor core-only mass estimate.
- Though cooling system design was beyond the scope of this study, some estimates of cooling system power were needed to evaluate system losses. A simple mass scalar was also used to estimate the impact of cryocooler mass. As semiconductors may not require temperatures as low as components with superconductor material in order to achieve low losses, a two cryogen system may offer an option for a more efficient and lower mass system.
- The dynamic system modeling approach implemented allowed rapid assembly of a system model with only high-level component parameters, and was sufficient for investigating both control and basic fault scenarios.
- For the power and voltage levels considered, evolving standards in the marine space for Medium Voltage Direct Current are the closest analog and can be leveraged. These standards are, however, still being developed and will not likely address superconducting and cryogenic systems, and these standards will not likely address the weight sensitivity of systems for aircraft.

## 11.2 Recommendations

In general, research and development is required in all component areas to meet the mass and efficiency required for full turboelectric flight. System development is required to develop the power system architecture in coordination with the cryogenic system. Cryogenic power electronic testing and system developments will provide data and systems concepts to allow operating temperatures for low system losses when cooling is also included. System modeling for development of controls for stability

and robustness of flight-critical DC power systems will be required and could be applicable first at lower powers and non-cryogenic temperatures as electric flight progresses. These recommendations can be roughly grouped into electrical, cryogenic, and airframe-propulsion studies, and specific recommendations are provided below.

### 11.2.1 Electrical

- The DC grid stability and robustness should be further developed through modeling to investigate and propose local control and power sharing, as well as system management and fault reconfiguration approaches. The approaches would support system requirements development.
- Additionally, bus harmonics from power electronics should be studied to estimate their impact on the DC cables and cooling system versus filtering components.
- The cryogenic semiconductor studies completed under this effort should be furthered to include an improved test set-up, more devices, and a range of temperatures. This work would provide more recent data points than available in literature.

### 11.2.2 Cryogenic

- A Pressure Vessel and Cryostat Concept Trade Study for Motor / Generator / Electronics Weight Reduction is recommended. This trade study would evaluate the weight reduction potential of various cryostat concepts. Examples include (but are not limited to) strength-to-weight ratio enhancements like isogrid construction for metal interior pressure vessels, composite exterior walls with robust vacuum-tight surface treatments, honeycomb composite panel walls for electronics enclosures, compact rotor torque tube geometries (conical, re-entrant) with composite and / or hybrid metallic construction, and multi-lobed gas storage tanks.
- Concept optimization of electrical interconnection between cold neon and warm $N_2$ flow loops is recommended. This trade study would evaluate and compare various material and geometry options for hybrid HTSC-resistive construction types versus the all-resistive aluminum alloy variant originally assumed for the GE baseline study. The use of HTSC (e.g., YBCO) at the cold Ne-anchored end of the interconnection is expected to reduce heat leak significantly due to the lower thermal conductivity and zero heat generation of the HTSC compared to traditional resistive materials used in current leads.
- Lightweight, high pressure cryogen transfer line exploration is recommended. This trade study aims at theoretical optimization and bench-top feasibility demonstration of a promising cryogen transfer line geometry and construction targeting smaller hydraulic diameter and bend radius than today's commercially-available all-corrugated variants.
- AC superconductor cabling loss investigation is recommended to explore how the $MgB_2$ cabling process could affect superconductor AC loss performance and critical current degradation. The key, high-impact, programmatic benefit of such an empirical investigation is that it would establish a necessary, core technical foundation leveraging subsequent machine design studies towards higher fidelity sizing and performance predictions. The investigation need not be machine design-specific, per se, but would be motor / generator-centric in that the cable forms targeted for coupon-level construction and testing would be amenable to machine stator slot and end-turn winding.
- LNG-based architecture studies are recommended as a parallel development path for weight reduction. This could compare a cryogenic system with LNG used as fuel and electrical component coolant to the studied superconducting systems.

### 11.2.3 Airframe-Propulsion

- Studies investigating fan and inlet design across aircraft size classes and mission ranges are recommended to understand the aircraft size and mission which could most benefit from TeDP, and to understand the impact on the rating and size of a TeDP system.

# Appendix A.—Superconducting Contact

It is assumed that a 600 A, 10,000 volt superconducting contactor will be available by 2025, since superconducting contacts are already available in that current range. High temperature superconducting disconnects are presently available with current rating in the 1000s of ampere range, and the literature recently reports resistance in the 1 μΩ range (Ref. 32). The most promising technique at this date is Yttrium Boron Copper Oxide (YBCO) with a thin silver plating. Contact resistance on the order of 1 μΩ has already been reported, with contact force in the range of 10 to 500 N, which is well within range of the electromechanical techniques used in conventional power contactors.
Note that "superconducting" is a misnomer for the expected contactor, since the resistance is not zero. However, it is low enough so that the power losses (0.36 W per contactor at 600 A) are acceptable.

It is expected that the design of the superconducting contactor will resemble that of a conventional contactor, except its actuation coil will be superconducting, and its contacts will have very low resistance. The size and weight of the superconducting contactor will be comparable to that of a conventional contactor.

The actuation coil is expected to have zero steady-state losses. It may or may not have small energy losses during opening and closing, but it is not expected that the contactors will be called upon to operate very often, so that does not really matter.

Another consideration for this application is contact life (number of switching operations). At present there is not much information on how many times superconducting contacts may be operated before requiring replacement. The technology is still in its infancy, so it is quite likely that by 2025 it will advance to achieve contact lifetime comparable to that of conventional contacts. Also, in this application, it is not expected that there will be any contact erosion due to arcing, since the contacts will be opened only when there is no current through them, and will be closed only when the voltage across them is zero.

Opening speed is also of interest in this application. In conventional contactors, the usual design employs a spring to open the contactor, and an electromagnet to close it. It is possible to increase the opening speed by using a spring to close, and an electromagnet to open. In any case, it is expected that opening time of around 1 msec is possible.

If it is required to open much faster than that, it is possible to use a repulsion disc principle. Because the repulsion disc would be superconducting, extremely high forces could be developed, so it would be possible to achieve opening times on the order of 100 μsec.

# Appendix B.—Cryogenic Semiconductor Tests and Results

## B.1 Objective

The objective of the team is to test silicon devices, both IGBT structure and MOSFET structure designed for high voltage operations (up to 4 kV for the IGBT and 4.5 kV for the MOSFET) at cryogenic temperature. The test will highlight, for the first time, the behavior of a device designed for high voltage operated at low temperature, and it will highlight the performances of the IGBT and MOSFET structures for use in high power circuitry. It must be noted that the structures are designed to work at room temperature and above; therefore, the team expects that the performances at cryogenic temperatures can be improved by designing doping profiles optimized to operate at cryogenic temperatures. The team cooled the devices to $LN_2$ temperature (about 77 K) and performed switching measurements. The test is aimed to establish the conduction and switching losses of high voltage rated devices in cryogenic environment.

## B.2 Introduction

Two devices have been considered for the cryogenic tests: the IGBT IXEL40N400 and the MOSFET IXTL2N450, both of them produced by IXYS. These devices have been considered as an example of high voltage silicon parts that could be used in a high power application.

The IGBT is rated for 4 kV and 90 A at 25 °C (it decreases to 40 A if the junction temperature is 110 °C), and the MOSFET is rated for 4.5 kV and 2 A at 25 °C (and a differential resistance of 20 Ω approximately). Both parts have and identical footprint, and both parts use the same amount of silicon: 14.26- by 14.26- by 0.6-mm approximately.

Figure 64 shows the IGBT (on the left) and the MOSFET (on the right) in their commercial package (bottom) and without the plastic envelop (top). Figure 65 shows the active silicon area completely isolated and overlapped on the devices (IGBT on the left and MOSFET on the right), and Figure 66 shows the two active areas next to each other (IGBT on the left and MOSFET on the right), showing that the two devices use the same identical area.

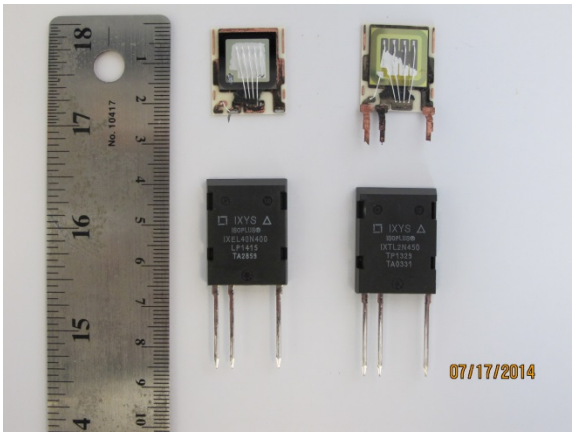


Figure 64.—IGBT (left) and MOSFET (right) Full Package and Stripped Version

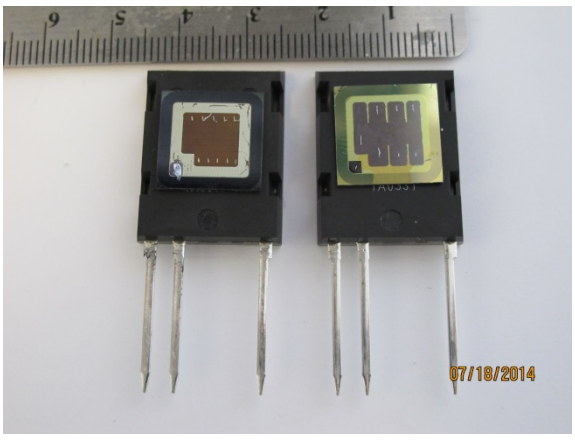


Figure 65.—IGBT (left) and MOSFET (right) Full Package Overlapped With Active Silicon Area

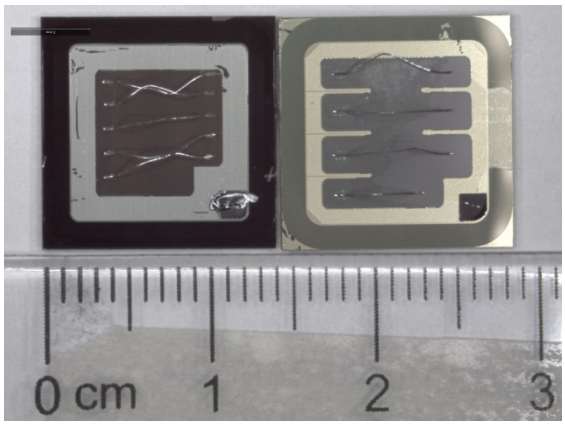


Figure 66.—Active Silicon Area of IGBT (right) and MOSFET (left)

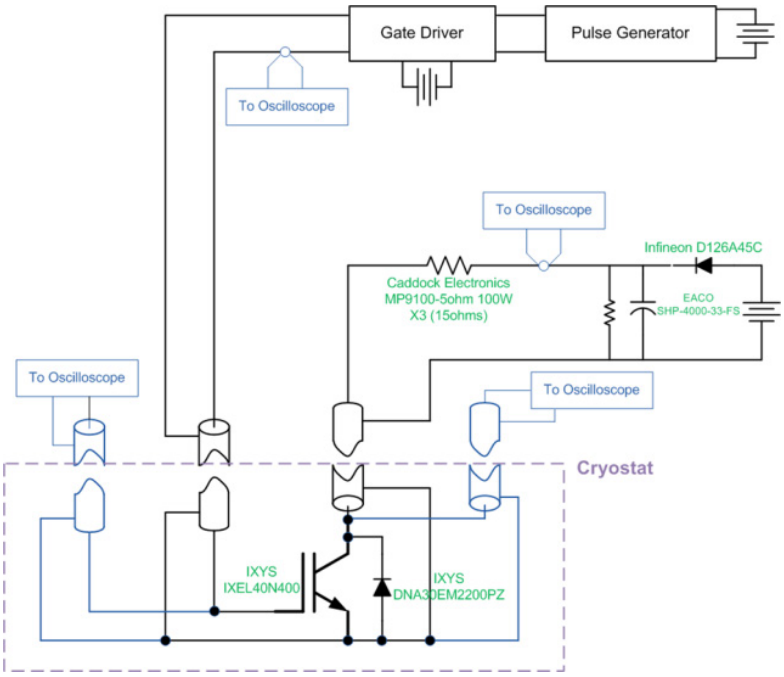


Figure 67.—Resistive Switching Schematic

The authors consider the comparison of the two structures a fair comparison based on the fact that they use the same silicon area.

## B.3 Test Set-Up

The test set-up follows a similar procedure as the one listed in (A. Caiafa 2004). The testing circuit with resistive load is represented in the schematic shown in Figure 67. While the symbol of the device in Figure 67 is relative to the IGBT, the same circuit has been used for both IGBT and MOSFET switching testing.

The test bed was assembled to minimize the parasitic inductance and to minimize the thermal losses such that the temperature of the device can be considered constant throughout the test. In order to minimize parasitic inductance, coaxial cables were used for every connection from inside the cryostat to outside, and to minimize thermal losses, thermal barriers were added to the set-up. The thermal stability of the device was also greatly improved by the use of a large heat sink. Figure 68 shows the set-up before

being inserted into the cryostat: the large heat-sink is visible on the bottom, the device is mounted on the heat-sink and it is connected through four coaxial cables to the top of the insert. In Figure 68, the two thermal barriers are also visible. The team used four coaxial cables to implement the four probe measurement technique for both the conduction (two coaxial cables used for a total of four conductors) path and the gate controls (two coaxial cables used for a total of four conductors).

Figure 69 shows the full set-up that includes: the $LN_2$ tank, the test cryostat, the oscilloscope, and the power supply. Not visible in the figure is the resistive load and the capacitor bank (behind the oscilloscope).

The insert was equipped with thermal probes as well: one next to the device, one below the heat-sink, and one a few centimeters above the device. The last probe was mainly used to make sure that the device is fully covered in $LN_2$ during the test.

Figure 68.—Test Insert


Figure 69.—Test Set-Up

## B.4 Static Tests

The team has tested both IGBT and MOSFET, collecting the V-I curves at cryogenic temperature. After slowly cooling the device, once the device is completely submerged by $LN_2$ and has been submerged for more than one minute, the device has been collected to a high power curve tracer and the V-I characteristic was collected. The test has been repeated two times per device. Only one IGBT and one MOSFET were tested.

Thanks to the high power curve tracer, the team was able to test the IGBT with currents as high as 200 A. Figure 70 shows the V-I characteristic of the IGBT. Focusing first on the characteristic at LNT and room temperature (25 °C), it is possible to observe that the IGBT at LNT has an improvement of about 38 percent.

It must be stated that the thermal resistance of the IGBT packaging decreases by about 5 to 10 times compared to the room temperature thermal resistance. In other words, losses that will increase the temperature of the junction of the IGBT of 10 °C, for example, will cause an increase of junction temperature of 50 to 100 °C in an IGBT kept to 25 °C; therefore, it is more meaningful to compare LNT performances to 125 °C junction performances. Comparing these two characteristics, shown in Figure 70 in solid blue (LNT) and in red (125 °C), it is possible to observe that the losses are about 55 percent less at LNT.

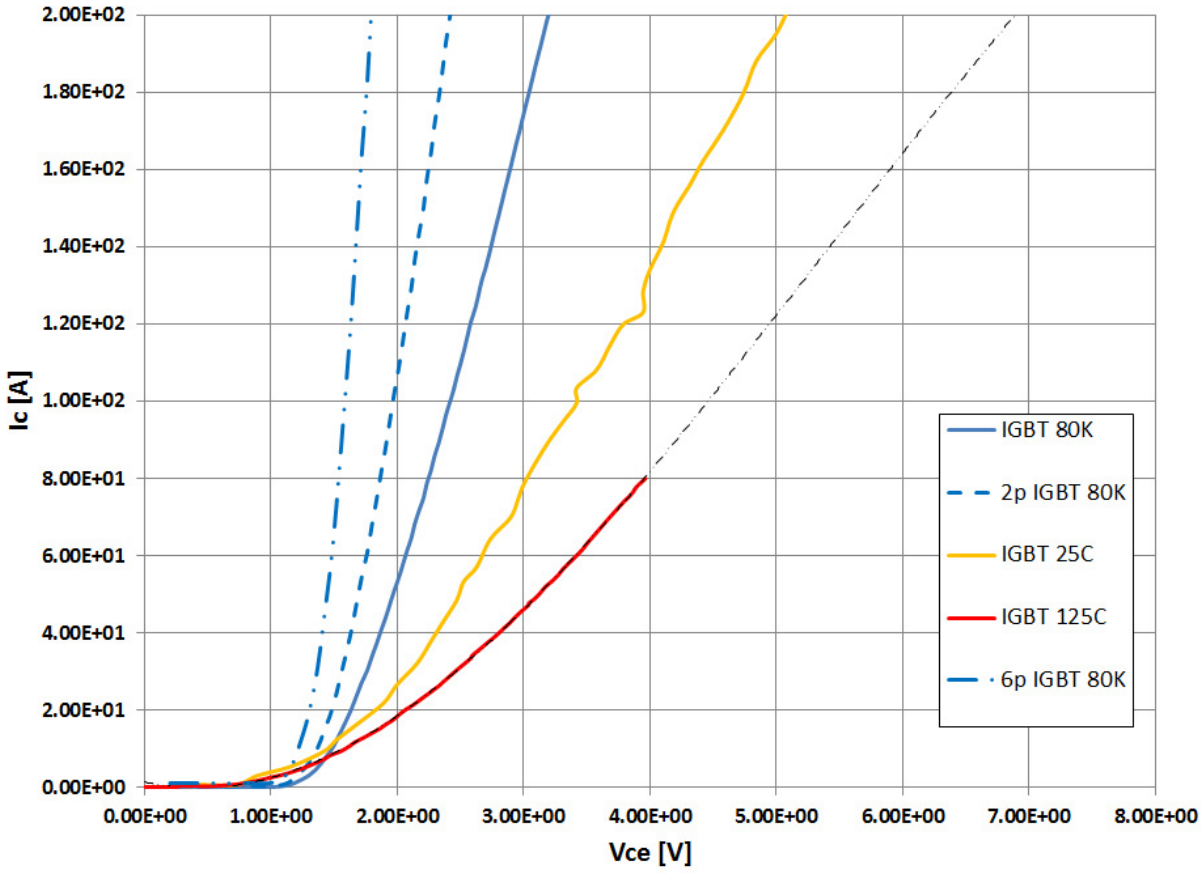


Figure 70.—V-I Characteristic of the IGBT. Measured at LNT (solid blue), two IGBTs in parallel at LNT (marked as 2p IGBT), 6 IGBTs in parallel at LNT (marked as 6p IGBT). Characteristic at room temperature (yellow trace), and at 125 °C (red trace).

If lower conductive voltage drop is needed, more devices can be paralleled. In Figure 70 the curves of two IGBTs paralleled and six IGBTs paralleled are shown. While the overall voltage drop does not decrease in proportion, a much larger current can be conducted for a relatively small junction temperature increase. Paralleling more than six devices becomes quite difficult due to device characteristic pairing and parasitic inductance issues.

Figure 71 shows the V-I characteristic of the MOSFET at LNT, room temperature, and 125 °C.

Figure 71 shows that a cryocooled MOSFET has 80 percent less losses than the same MOSFET operated at room temperature, and about 90 percent less losses than a MOSFET with a junction temperature of about 125 °C (about 10X improvement). As with the IGBT, the thermal resistance drastically decreases at LNT, making it more meaningful to compare the LNT characteristic with the 125 °C characteristic than comparing it to the 25 °C characteristic.

In summary, the cryocooled IGBT exhibits a 2 times improvement, while the cryocooled MOSFET exhibits a 10 times improvement in conduction losses performances.

Despite the fact that the MOSFET has a much larger improvement than the IGBT, the IGBT has a much better power density capability. Figure 72 shows a comparison of the cryocooled IGBT and MOSFET conduction performances. It is clear that, given the same silicon area and same voltage blocking capability, the IGBT can conduct a much larger current. In order to match the performances of the IGBT at 200 A, about 160 MOSFETs are required to be connected in parallel.

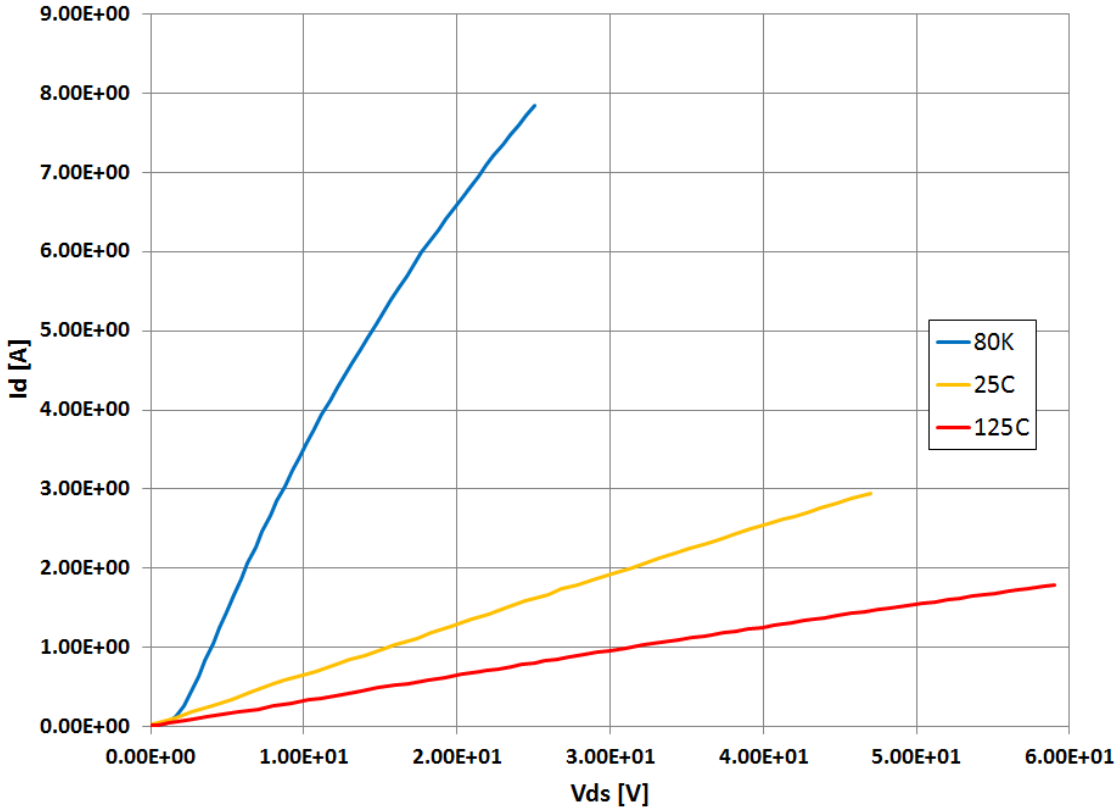


Figure 71.—V-I Characteristic of the MOSFET. At LNT (blue trace), at room temperature (yellow trace), and at 125 °C (red trace)

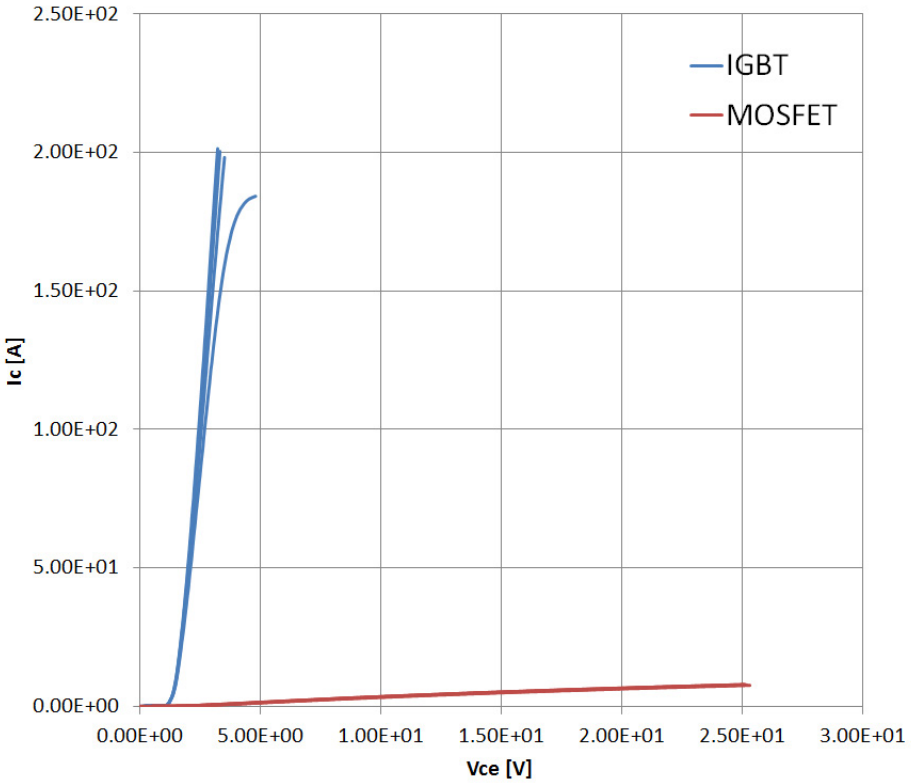


Figure 72.—Comparison of the V-I Characteristics of the IGBT (blue trace) and MOSFET (red trace). Measured at LNT

The breakdown voltage of the IGBT at LNT decreased to 3.6 kV, while the breakdown of the MOSFET decreased to 3.2 kV. It must be noted that only one IGBT and one MOSFET have been tested. To have a more statistically meaningful value, a larger number of devices need to be tested.

In conclusion, a MOSFET structure exhibits a larger improvement, but an IGBT structure still exhibits much less losses for same silicon area and voltage blocking capability.

## B.5 Dynamic Testing

### B.5.1 Resistive Test Results

The resistive test was performed using a low inductance high energy dissipation resistor of approximately 5 Ω. The voltage drop on the device was measured through a voltage divider and a zener diode that clamps the measured voltage when this rises above the zener voltage (in this experiment it was about 15 V).

An example of the data collected during the resistive switching test is shown in Figure 73. In this figure, the green trace corresponds to the current through the Device Under Test (DUT), the red trace corresponds to the voltage drop across the DUT, and the purple trace corresponds to the capacitor voltage. The controller used to control the circuit provides a double pulse command; while this is not necessary for a resistive switching, it will be for the inductive switching. The team used this data to measure the voltage droop at various currents. The challenge in this measurement is the transition time (visible in the red trace) due to the use of the zener and the voltage divider, and the accuracy of the Vce (collector-emitter voltage during conduction) measurement. It is quite difficult to distinguish the voltage droop of the device from the zener transition.


Figure 73.—Oscilloscope Traces for Resistive Test at 40 A

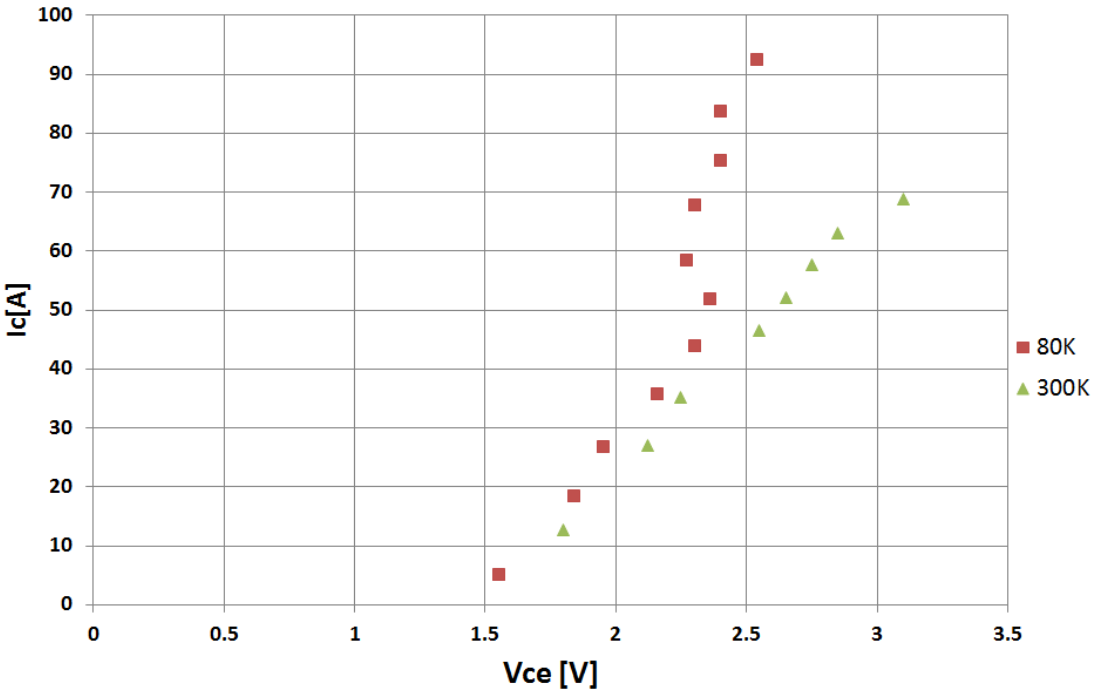


Figure 74.—First Set of Data Captured at $LN_2$ Temperature

Figure 74 shows a set of data collected using the set-up and measurement system described above. While the results of the resistive dynamic measurements at cryogenic temperature are quite comparable with the data collected statically (V-I curves), the team feels that the resistive dynamic measurement set-up needs improvement and is working toward it.

### B.5.2 Inductive Test

The team has prepared the inductive load and the test bed for the inductive switching as shown in Figure 75. The inductor built is 510 µH and the recirculating diode is a Schottky SiC diode rated for 100 A. The selected diode will minimize the reverse current effect during the turn on, allowing the team to perform more accurate losses evaluation.

Figure 76 shows double pulse waveforms collected using a cryocooled IGBT. The purple trace represents the voltage and the green trace represents the current. Figure 77 and Figure 78 show the turn on and turn off, respectively.

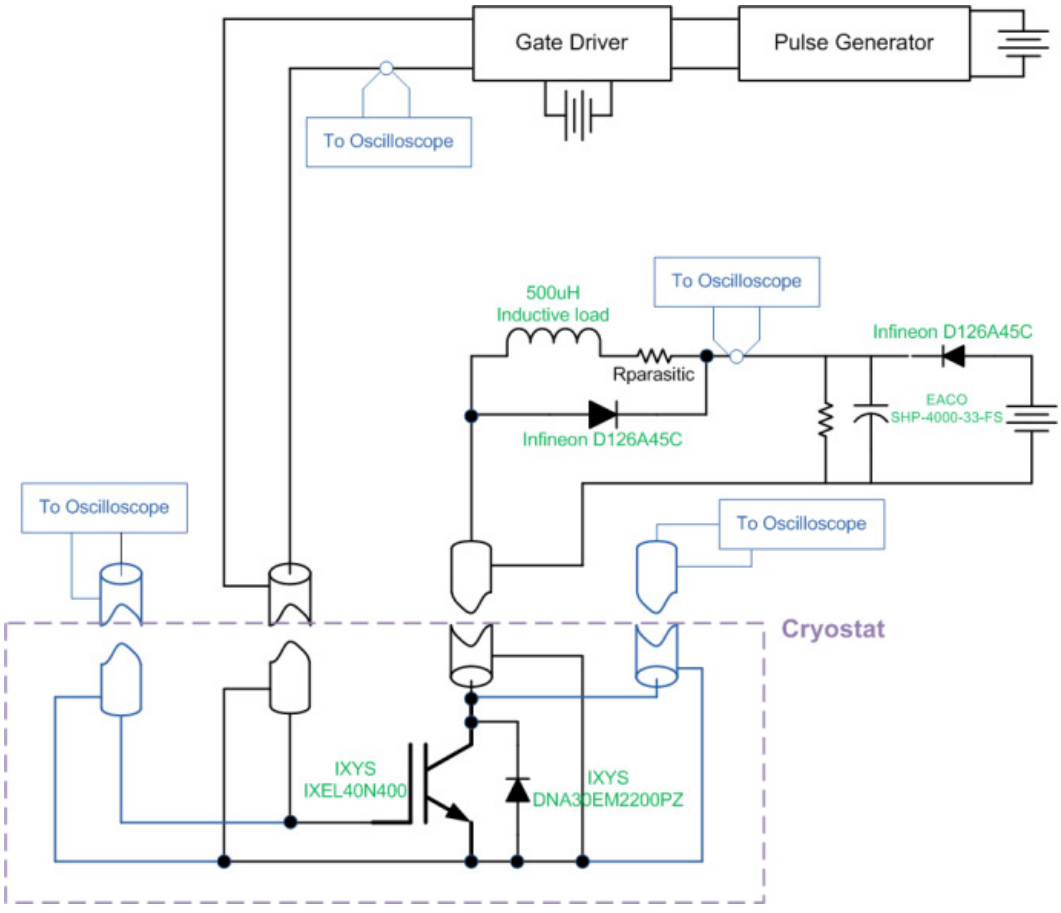


Figure 75.—Inductive Switching Test Set-up

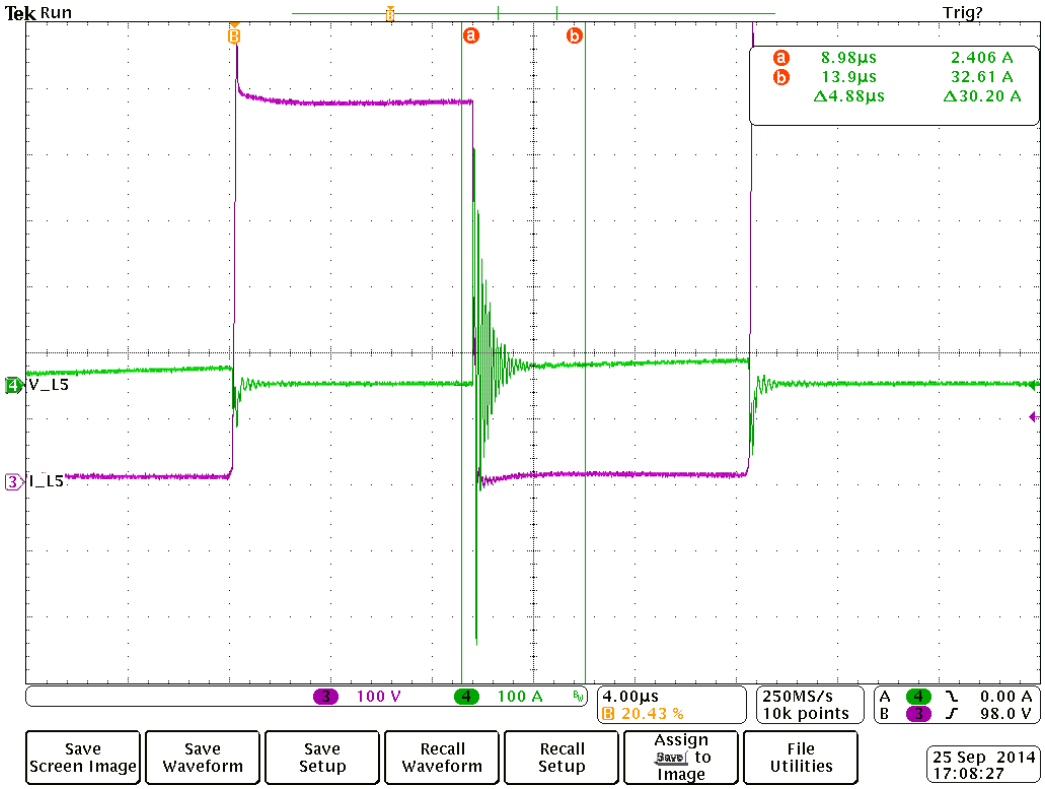


Figure 76.—Detail of the Double Pulse Test of the Inductive Switching at LNT

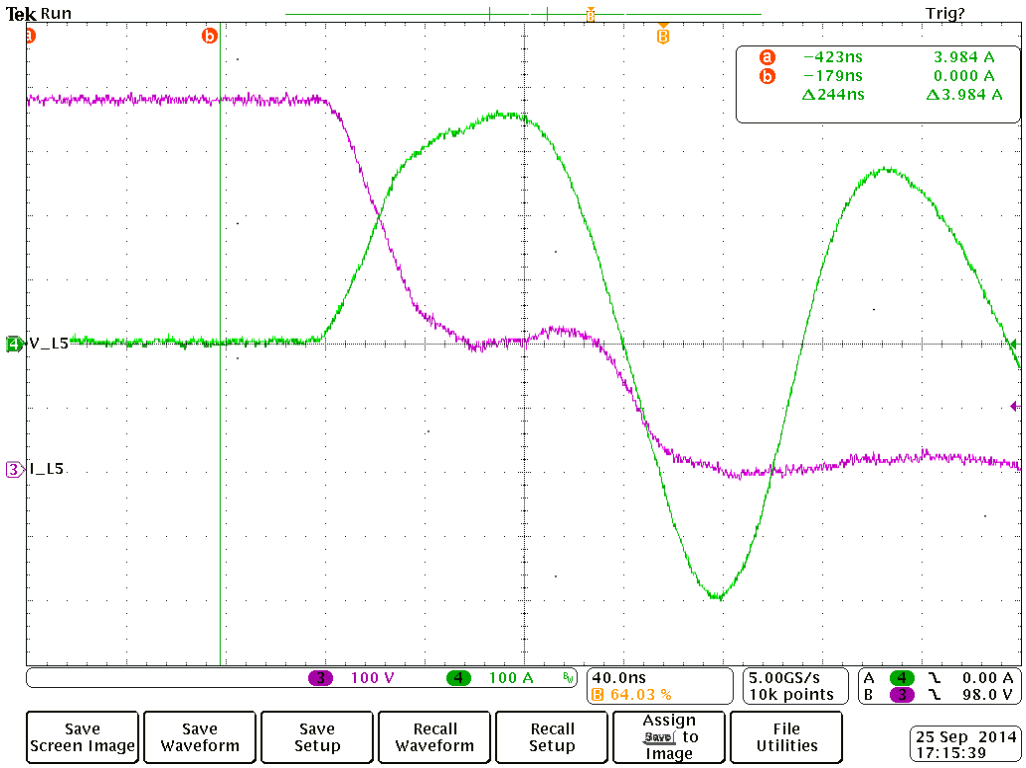


Figure 77.—Inductive Turn-On at LNT

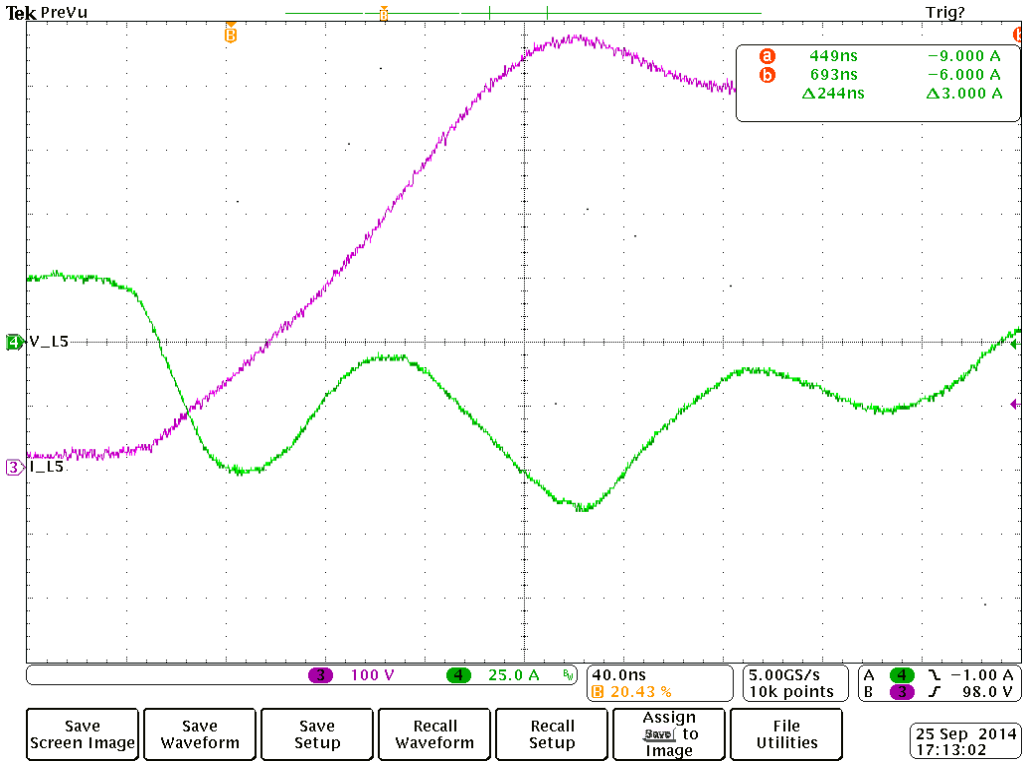


Figure 78.—Inductive Turn-Off at LNT

The set-up was operated to produce 600 V and 30 A. The initial objective was to push the device at higher voltage and higher current, but, because of the excessive current ringing (both overshoot and undershoot), the team had to limit the test to the mentioned value. The large current peaks can damage not only the device under test, but especially the equipment connected around it. The current overshoots are caused by the excessive parasitic inductance, measured to be around 500 Nh, that is introduced by the relatively long coaxial cables and by the very fast turn on and turn off speed of the DUT. The long coaxial cables were needed to lower the DUT into the cryogenic bath in the available cryo-tank. The very fast speed of the device is due to the increase in the carrier mobility at cryo temperature.

By observing the curves shown in Figure 77 and Figure 78, we can argue that the device switches in an extremely short time (the current reaches the maximum peak within 10s of nanoseconds), but, because of the large ringing caused by the parasitic inductance, not much more can be said.

The MOSFET is expected to switch faster than the IGBT, so the issues caused by the parasitic inductance will be magnified. This is the reason why the team decided not to test the MOSFET within this set-up.

## B.6 Conclusions

The team proved that there are benefits in using cryocooled large voltage blocking devices. A more detailed study is needed to completely assess the benefit of high voltage cryocooled devices (new dynamic test bed).

A different cryo-tank has been identified that will require much shorter coaxial cables; therefore, a much lower parasitic inductance, to repeat the dynamic tests and complete the assessment of the two DUT (IGBT and MOSFET).

Given the results obtained, the team feels confident that a system based on the use of superconductors and cryo-power electronics will be beneficial to the overall system efficiency, especially if the system utilizes a “disposable” coolant such as a fuel. A two temperature cryogenic system (operating at two different cryo temperatures) may be the ideal choice.

# Appendix C.—Model Description

The file below provides the parameters used for the Matlab/Simulink system model used for this program.

10/24/14 10:01 AM  D:\Users\a...\InputParameters RTAPSv07.m    1 of 4

```
%%%%%%%%%%%%%%%%%%%%%%%%%%%%%%%%%%%%%%%%%%%%%%%%%%%%%%%%%%%%%%%%%%%%%%%%%%%%%%%%%%%%%%%%%↙
%%%%%%%%%%%%%%%%%%%%%%%%%%%%%%%%%%%%%%%%%%%%%%%%%%%%%%%%%%%%%%%%%%%%%%%
% Prepared for:
% NASA RTAPS Architecture, Voltage and Components for Turboelectric
% Distributed Propulsion (TeDP) Electric Grid
% Contract #NNC10BA06B Order NNC13TA73T
%
% Purpose:
% Simulation Parameters for RTAPS simulink *.slx files
%
%
% Calls: None
%
% runs with RTAPSv6.mdl
%%%%%%%%%%%%%%%%%%%%%%%%%%%%%%%%%%%%%%%%%%%%%%%%%%%%%%%%%%%%%%%%%%%%%%%%%%%%%%%%%%%%%%%%%↙
%%%%%%%%%%%%%%%%%%%%%%%%%%%%%%%%%%%%%%%%%%%%%%%%%%%%%%%%%%%%%%%%%%%%%%

%
clear

%% Simulation Parameters
%
tstep=0.25e-3;                      % Simulation step time (presently set to auto)
tsample=1.1e-3;                     % Sample time for discrete variables (flipflops)
tstart=0;                           % Simulation start time
tend=tstart+60.0;                   %
tsave=2.00e-4;                      % Time between saves to the Matlab environment
tsave2=15e-3;                       % Time between saves to the Matlab environment for↙
slow variables
Ndata=5e6;                          % Maximum number of data points saved

%% System Modes
%
%  Single "mode" used selects generator on
% M3   M2   M1    M0
% 1    0    0    1       Generator on mode
M0G_1ch=1;
M1G_1ch=0;
M2G_1ch=0;
M3G_1ch=1;

%% Engine Model
%
Peng=25e6;                          % Engine power rating
rpm_engine=9000;                    % Engine power turbine rated speed (rpm)
wmeng=rpm_engine*pi/30;             % Engine power turbine rated speed (rad/s)
Tengmax=1.1*Peng/wmeng;             % Maximum Torque
Jeng=0.07;                           % Engine dynamic model Inertia
Gpeng=140;                           % Engine dynamic model proportional gain
Gieng=107;                           % Engine dynamic model integral gain
```

```
tvsofteng=20e-3;                    % Soft start time constant
Gvengdroop=0/Tengmax;               % Droop factor for speed mode droop control
dVengdroop=0;                       % No load speed offset (increase) for droop control

% Engine initilization
Penginit = 1e6;
Tenginit = Penginit/wmeng;

%% Generator Parameters
%
Pgen = 12.5e6;
rpm_hpgen_max=rpm_engine*1.1;        % Generator maximum speed 10% overspeed (Nominal↙
speed = 9000 rpm)
wm_hpgen_max=2*pi*rpm_hpgen_max/60;
rpm_hpgen_min=rpm_engine*.9;         % Generator minimum speed
wm_hpgen_min=2*pi*rpm_hpgen_min/60;
Vhpgen=8000;                         % Generator voltage
Ihpgenmax=2*Pgen/8000;               % Maximum current out of generator (2x rated)
Kvhp=Vhpgen/wm_hpgen_min;            % Speed voltage and torque constant
RCuhp=0;                             % Effective series resistance for losses (0 for SC↙
machine)
Reddyhp=1e6;                         % Effective parallel resistance for (inf for air↙
core machine)
Ihysthp=0;                           % Effective parallel current source for hysteresis↙
losses (0 for air core machine)
Awindagehp=1.19e-7;                  % Windage loss factor (N-m-s^2) Twind=Awindage*wm^2
% Chpgen=8e-3;                         % Generator dynamic model output C
% Gphpgen=16.8;                        % Generator dynamic model proportional gain
% Gihpgen=1.6e3;                       % Generator dynamic model integral gain
Chpgen=1e-4;                        % Generator dynamic model output C
Gphpgen=21;                        % Generator dynamic model proportional gain
Gihpgen=5e5;                       % Generator dynamic model integral gain

tvsofthp=20e-3;                      % Soft start time constant
Gvhpgendroop=100/Ihpgenmax;          % Droop factor for voltage mode droop control
dVhpgendroop=50;                     % No load voltage offset (increase) for droop↙
control
Vhpgeninit = Vhpgen;                 % soft start initilization point

%% Generator Power Converter
%
% Rectifier Characeristics
Vfeffhp=1.2;                          % Effective diode forward voltage drop
Rfeffhp=1e-3;                         % Effective diode resistance
%
% Power Converter  switch characteristics (presently not used for generator power↙
converter)
Rswinveffhp=1e-3;                     % Inverter effective switch resistance
Voinveffhp=2;                         % Switch offset voltage
Fswhp=1200;                           % Switching frequency
Eonnormeffhp=2.57e-7 *2/3;            % Normalized turn on switching energy
```

```
Eoffnormeffhp=9.2e-7 *2/3;            % Normalized turn off switching energy
Edeadnormeffhp=1.0e-10;               % Dead time energy loss in reverse SiC diode offset
(Vf=2.5V, tdead=400ns)

%% Gen Bus breaker inductance model (breaker inductance and Converter EMI inductor)
%
Vsdchp=8000;                          % Source voltage
Ldchp=5.00e-4;                        % Inductance of the bus fault current limiting
breaker
Rdcshp=1e-6;                          % Series resistance (silver breaker contact
resistance)
Rdcp=100;                             % Fault Current Limiting Inductor damping resistor
ILdchp=0;                             % Initial inductor current
Cdchp=5.1e-6;                         % Bus capacitance (uses Power Converter EMI filter
value)
VCdchp=8000;                          % Initial capacitor voltage

%% Motor Feeder Inductance
%
Ldcfeed=1.00e-6;                       % Inductance of the bus fault current limiting
breaker
Rdcsfeed=1e-9;                         % Series resistance (0 for superconductor)
ILdcfeed=0;                            % Initial inductor current


%% Motor Bus breaker inductance model (breaker inductance and Converter EMI inductor)
%
Vsdcmot=8000;                         % Source voltage
Ldcmot=2.00e-3;                       % Inductance of the bus fault current limiting
breaker
Rdcsmot=1e-6;                         % Series resistance (silver breaker contact
resistance)
ILdcmot=0;                            % Initial inductor current
Cdcmot=1.2e-6;                        % Bus capacitance (uses Power Converter EMI filter
value)
VCdcmot=8000;                         % Initial capacitor voltage

%% Fan Model
% Assume cubic load PFan = aFan * WmFan^3,
PFan = 3.575e6;                      % Rated Fan ouput power at Speed (w)
rpmFan = 3500;                       % (rpm)
WmFan = rpmFan*pi/30;                % Rated Fan speed (rad/sec)
aFan = PFan/WmFan^3;                 % Assume fan load is cubic

wFan_ic = 800*pi/30;                 % Initial fan speed (rad/sec)
wFan_sp = 1000;                      % saturation limit (rad/sec)

%% Motor Parameters
%
rpm_hpmot_max=rpmFan*1.2;            % Motor maximum speed 10% overspeed (Nominal speed =
8000 rpm)
```

```
wm_hpmot_max=2*pi*rpm_hpmot_max/60;
rpm_hpmot_min=rpmFan*1.1;            % Motor corner point speed
wm_hpmot_min=2*pi*rpm_hpmot_min/60;
Hmot = 0.8;                          % Motor and fan inertia in per unit (sec)
Jhpmot=2*3.1e6*Hmot/WmFan^2;         % Motor moment of inertia (kg m^2)
Vhpmot=8000;                         % Motor voltage
Ihpmotmax=PFan/8000;                 % Maximum current out of Motor (3.1 MW/8000V)
Kvhpmot=Vhpmot/wm_hpmot_min;         % Speed voltage and torque constant
RCuhpmot=0;                          % Effective series resistance for losses (0 for SC↙
machine)
Reddyhpmot=1e6;                      % Effective parallel resistance for (inf for air↙
core machine)
Ihysthpmot=0;                        % Effective parallel current source for hysteresis↙
losses (0 for air core machine)
Awindagehpmot=1.19e-7;               % Windage loss factor (N-m-s^2) Twind=Awindage*wm^2
Chpmot=8e-4;                         % Motor dynamic model output C
Gphpmot=1.68;                        % Motor dynamic model proportional gain
Gihpmot=160.0;                       % Motor dynamic model integral gain
tvsofthpmot=20e-3;                   % Soft start time constant

GP_fan = 2;                          % Fan speed control proportional gain
GI_fan = 1;                          % Fan speed control integral gain

%% Motor ICC
%
% Power Converter rectifier characeristics
%
Vfeffhpmot=1.2;                      % Effective diode forward voltage drop (2x diode↙
drop)
Rfeffhpmot=1e-3;                     % Effective diode resistance
%
% Power Converter  switch characteristics
Rswinveffhpmot=1e-3;                 % Inverter effective switch resistance
Voinveffhpmot=2;                     % Switch offset voltage
Fswhpmot=1.2e3;                      % Switching frequency
Eonnormeffhpmot=2.57e-7 *2/3;        % Normalized turn on switching energy
Eoffnormeffhpmot=9.2e-7 *2/3;        % Normalized turn off switching energy
Edeadnormeffhpmot=1.0e-10;           % Dead time energy loss in reverse SiC diode↙
offset(Vf=2.5V, tdead=400ns)
```

## References


1. M. Armstrong, C. Ross, D. Phillips and M. Blackwelder, "Stability, Transient Response, Control, and Safety of a High-Power Electric Grid for Turboelectric Propulsion of Aircraft," NASA/CR—2013-217865.
2. R. Marquardt, "Modular Multilevel Converter: An Universal Concept for HVDC-Networks and Extended DC-Bus-Applications," The Proceedings of 2010 International Power Electronics Conference, June 2010, Sapporo, Japan.
3. E. Solas, G. Abad, J. A. Barrena, S. Aurtenetxea, A. Carcar and L. Zajac, "Modular Multilevel Converter with Different Submodule Concepts – Part I: Capacitor Voltage Balancing Method," IEEE Transactions on Industrial Electronics, vol. 60, No. 10, Oct. 2013.
4. D. Soto-Sanchez and T. C. Green, "Control of a Modular Multilevel Converter-based HVDC Transmission System," The Proceedings of the 2011-14th European Conference on Power Electronics and Applications.
5. J. Song-Manguelle, R. Datta, M. Harfman Todorovic, R. Gupta, D. Zhang, S. Chi and R. Lai, "A Modular Stacked DC Transmission and Distribution System for Long Distance Subsea Applications," 2012 IEEE Energy Conversion Congress and Exposition (ECCE), Sep. 2012, Raleigh, NC.
6. R. Datta, C. Sihler, R. Zhang, Collection and transmission system, European Pat. EP20070122541, June 2007.
7. European Pat. EP20070122541, June 2007, R. Zhang, R. Datta, C. Sihler and J. Song-Manguelle, Modular Subsea Power System Architectures, U.S. Patent 2010/0133901, Dec. 2008.
8. R. Datta, C. Sihler, R. Zhang, Direct Current transmission and distribution system, U.S. Patent 7,851,943 Dec. 2010.
9. R. Thome, W. Creedon, M. Reed, E. Bowles and K. Schaubel, "Homopolar Motor Technology Development," in IEEE Conference Publications, Power Engineering Society Summer Meeting, 2002.
10. R. A. Marshall, "3000 Horsepower Superconductive Field Acyclic Motor," IEEE Transactions on Magnetics, Vol. 19, no. 3, pp. 876-879, 1983.
11. Caiafa A., X. Wang, J.L. Hudgins, E. Santi, and P.R. Palmer, "Cryogenic Study and Modeling of IGBTs, 2003 IEEE Power Electronics Specialists Conference (PESC)," Vol. 4, 2003, Acapulco, Mexico.
12. Otward Mueller, Properties of high-power cryo-MOSFETs 1996 IEEE Industry Application Conference (IAS), Vol. 3, 1996, San Diego, CA.
13. R. L. Patterson, A. Hammond and S. S. Gerber, "Evaluation of Capacitors at Cryogenic Temperatures for Space Applications," Conference Record of the 1998 IEEE International Symposium on Electrical Insulation, 1998, pp: 468-471, Vol. 2.
14. S. Gerber, A. Hammond, M. Elbuluk and R. Patterson, "Performance of High-Frequency High-Flux magnetic Cores at Cryogenic Temperatures," 37th Intersociety Energy Conversion Engineering Conference (IECEC), Vol. 1, July 28 – Aug. 2, 2002.
15. M. Elbuluk, and A. Hammond, "Power electronics in harsh environments," Industry Applications Conference, 2005. Conference Record of the 2005 Fortieth IAS Annual Meeting, Vol. 2, pp: 1442-1448.
16. T. Zhang, E. Laskaris, M. Shah, J. Bray and K. Sivasubramaniam, "Electrical Machine with Superconducting Armature Coils and Other Components." United States of America Patent 20110285219 A1, 24 November 2011.
17. James, D. R., and Sauers, I. (2004). "Electrical insulation materials for superconducting col applications," Power Engineering Society General Meeting, 2, pp. 2062-2064, Vol. 2. Denver, CO: IEEE.

18. Gerhold, J. (2002, December). Potential of Cryogenic Liquids for Future Power Equipment insulation in the Medium High Voltage Range. IEEE Transactions on Dielectrics and Electrical Insulation, 9(6), 878-890.
19. Shanbhag, M., and Chow, T. P. (2002). Cryogenic Operation of 4H-SiC Schottky rectifiers. Proceedings of the 14th International Symposium on Power Semiconductor Devices and ICs, (pp. 129-132). Santa Fe.
20. Chen, S., Cai, C., Wang, T., Guo, Q., and Sheng, K. (2013). "Cryogenic and high temperature performance of 4H-SiC power MOSFETs," Applied Power Electronics Conference and Exposition (APEC), 2013 28th Annual IEEE, (pp. 207-210), Fort Worth.
21. Rajashekara, K., and Akin, B. (2013), "A review of cryogenic power electronics - status and applications," IEEE International Electric Machines and Drives Conference, pp. 899-904, Chicago.
22. Leong, K., Bryant, A., and Mawby, P. (2010). Power MOSFET Operation at Cryogenic Temperatures: Comparison between HEXFET, MDMesh, and CoolMOS. 22nd International Symposium on Power Semiconductor Devices and IC's (ISPSD), 2010, (pp. 209-212). San Diego.
23. Schlogl, A., Deboy, G., Lorenzen, H., Linnert, U., Schulze, H.-J., and Stengl, J. (1999), "Properties of CoolMOS between 420 K and 80 K-the ideal device for cryogenic applications," Proceedings of the 11th International Symposium on Power Semiconductor Devices and ICs, 1999, ISPSD '99, pp. 91-94, Toronto.
24. Caiafa, A., Snezhko, A., Hudgins, J., Santi, E., and Prozorov, R. (2004). "IGBT operation at cryogenic temperatures: non-punch-through and punch-through comparison," 4, pp. 2960-2966. Aachen.
25. De La Hidalga, F., Deen, M., and Gutierrez, E. (2000). Theoretical and experimental characterization of self-heating in silicon integrated devices operating at low temperatures. IEEE Transactions on Electron Devices, 1098-1106.
26. Ramalingam, M., Donovan, B., & Beam, J. (1996). Cryogenic refrigeration thermodynamics for a power conditioning electronic component. Proceedings of the 31st Intersociety Energy Conversion Engineering Conference, 1996. IECEC 96, 4, pp. 1390-1395. Washington, DC.
27. Gerapid: High Speed DC Breaker Application Guide, GE Energy Industrial Solutions, 2010.
28. Lightning DC: Incorporating the NDC Circuit Breaker, Hawker Siddeley Switchgear Ltd, www.hss-ltd.com, 2010.
29. Edwards, Huw, "Distributed Electrical Propulsion: Electrical Architecture Assessment," Roll-Royce Technical Report, DNS161385, March 2010.
30. Christoph Meyer, Stefan Schroder, De Doncker, "Solid-State Circuit Breakers and Current Limiters for Medium-Voltage Systems Having Distributed Power Systems," IEEE Transactions on Power Electronics, Vol. 19, No. 5, September 2004.
31. Magnus Callavik, Anders Blomberg, Jurgen Hafner, Bjorn Jacobson: "The Hybrid HVDC Breaker: An innovation breakthrough enabling reliable HVDC grids," ABB report.
32. K. Sawa, S. Masako, T. Masaru, and M. Masato: "A Preliminary Study of Mechanical Switch Using High Temperature Superconducting Material," Proc. 51st IEEE Holm Conference, pp. 272-276, 2005.
33. Lionel M. Levinson and H. R. Philipp, "Low-temperature ac properties of metal-oxide varistors," Journal of Applied Physics, Vol. 49, No. 12, pp6142-6146, December 1978.
34. General Electric Company, "Development of a HVDC Prototype Breaker," Final Report, Reporting Period: November 5, 1975 – October 1, 1978, Prepared for United States Department of Energy, Contract No. EX-76-C-01-2065, October 1978.
35. E. C. Sakshaug, J. S. Kresge and S. A. Miske, Jr., "A New Concept in Station Arrestor Design," IEEE Transactions on Power Apparatus and Systems, Vol. PAS-96, no. 2, March/April 1977.
36. J. W. Lue, J. R. Miller, and J. C. Lottin, Pressure Drop Measurement on Forced Flow Cable Conductors, IEEE Trans. Magnet. Mag-15, 53 (1979).
37. V. Arp, Forced Flow, Single Phase Helium Cooling Systems, Adv. Cryog. Eng. 17, 342 (1972).

38. J. W. Dean, W. Stewart, and J. K. Hoffer, “Temperature Profiles in a Long Gaseous Helium Cooled Tube,” Adv. Cryog. Eng. 23, 250 (1978).
39. T. Kupiszewski, O. R. Christianson, D. Natelson, “Predicted Thermal-Hydraulic Characteristics of Cable-In-Conduit Conductor Windings During Steady-State Operation,” Adv. Cryog. Eng. 41a, 513 (1996).
40. A. Caiafa, A. Snezhko, J.L. Hudgins, E. Santi, R. Prozorov, and P.R. Palmer, “Physics-Based Modeling of NPT and PT IGBTs at Deep Cryogenic Temperatures,” IEEE IAS 2004, pp. 2536-2541.
41. Ranbir Singh and B. J. Baliga, “Cryogenic Operation of P-i-N Power Rectifiers,” ISPSD 1993, pp. 193-198.
42. Munaf Rahimo, Future Trends in High Power MOS Controlled Power Semiconductors, ABB.
43. Rixin Lai, etc., “A Systematic Topology Evaluation Methodology for High-Density Three-Phase PWM AC-AC Converters,” IEEE Transactions on Power Electronics, Vol. 23, no. 6, pp. 2665-2680, Nov. 2008.
44. I. Clelland, R. Price, and W. J. Sarjeant, Advances in Capacitor Technology for Modern Power Electronics, IEEE Power Modulator Symposium, pp. 145-148, Jun. 2000.
45. Radun, A., “Simplified Aircraft DC Power System Model,” SAE Technical Paper 2014-01-2154, 2014.
46. Roa, M., “ABS Rules for Integrated Power Systems (IPS),” IEEE Electric Ship Technologies Symposium, April 2009, Baltimore, MD.
47. Khersonsky, Y, et al., “IEEE Electric Ship Technologies Initiative,” Petroleum and Chemical Industry Conference, 2009, 2009 Record of Conference Papers – Industry Application Society 56th Annual, Sept. 2009, Anaheim, CA.